571451 Research Performance Progress Report (RPPR) – DOE Solar Program

Research Performance Final Report

Project Title:	Loop Thermosyphon Enhanced Solar Collector
Project Period:	10/01/2018 – 03/31/2022
Budget Period:	04/01/2021 – 03/31/2022
Reporting Period:	10/01/2018 – 3/31/2022
Reporting Frequency:	Single
Submission Date:	7/29/2022
Recipient:	Advanced Cooling Technologies, Inc.
Address:	1046 New Holland Ave
	Lancaster, PA 17601
Website (if available)	www.1-act.com
Award Number:	DE-EE0008398
Project Team:	Advanced Cooling Technologies, Inc.
	University of Maryland, College Park
Principal Investigator:	Nathan Van Velson
	Phone: 717-205-0662
	Email: nathan.vanvelson@1-act.com
Business Contact:	Frank Morales, Jr.
	Phone: 717-205-0637
	Email: frank.molares.@1-act.com
HQ Tech Manager:	Andru Prescod
HQ Project Officer:	Christine Bing
GO Grant Specialist:	Meisha Baylor
GO Contracting Officer:	Patricia Clark

7/29/2022

Signature **Date**

Acknowledgment: This material is based upon work supported by the U.S. Department of Energy's Office of Energy Efficiency and Renewable Energy (EERE) under the Solar Energy Technology Office Award Number DE-EE0008398.

Table of Contents

Information from Statement of Project Objectives (SOPO)

Project Objective:

Task 1.1: Loop Thermosyphon System Modeling (M1-M18)

To begin this task, a cost and performance matrix of the loop thermosyphon system will be developed. A rigorous system model will then be developed based on the matrix to determine the cost and performance of the proposed loop thermosyphon. This model will be used to evaluate the working fluid temperature distribution, pressure head requirement, overall system cost and performance based on the design parameters such as tube size, materials properties, nanofluid concentration and flow rate, system power load, etc. The solar concentrating and tracking system will also be included in this model to provide a comprehensive system performance and cost aspects, including overall solar-to-thermal efficiency, capital cost, operation, and maintenance over the 25-year operation. The model will be continuously updated based on the test results in other tasks. By the completion of this task, a ready-to-use model with a preliminary design of a low-cost (<\$30/m^2, estimated based on the material cost and labor overhead for manufacturing and installation) loop thermosyphon system that supplies solar thermal energy at <\$0.01/kWh_{th} LCOH will be developed, and sensitivity analysis of LCOH will be applied based on the cost estimation model. The model, including all assumptions, methodologies, and conclusions, will be evaluated by a third-party company or organization proposed to and approved by DOE. The performance requirement of solar-absorbing nanofluid evacuated glass, and loop thermosyphon is updated according to the system model.

Task 1.2: Surfactant-Free Nanofluid Material Identification (M1-M3)

This task will identify a nanofluid solution based on graphene oxide to demonstrate the nanofluid's high optical to thermal efficiency and capability against segregation. A literature review will be completed to down-select the candidate pairs of pretreated nanoparticles and solvents that can potentially meet the light-absorbing

requirements, dispersion, two-phase stability during the partial boiling-condensation cycles, and the cost. Completion of this task will down-select 1-3 nanofluid options with the potential to present and maintain good stability and high solar-to-thermal efficiency over long-term operation. The nanofluid options will be presented to DOE for review and approval.

Task 1.3: Synthesis and Thermophysical Characterization of Nanofluids (M4-M15)

The nanofluids with selected candidate pairs in Task 1.1 at various concentrations will be synthesized for further analysis. Properties of the synthesized nanofluids, including but not limited to mass density, thermal conductivity, specific heat, viscosity, light absorbance, and particle size distribution before and after boiling-condensation cycles will be measured. By the completion of this task, at least one series of nanofluids (at variable concentration) that can potentially satisfy the project requirements for viscosity (will be determined based on the model in Task 1.1), long-term two-phase stability (minimum property change over time), high optical-to-thermal conversion rate inside the nanofluid (>99% of standard solar spectrum light converted to thermal energy within the nanofluid, to be updated based on the model developed in Task 1.1), etc. will be successfully synthesized with standard laboratory processing.

Task 1.4: Preliminary Nanofluid Reliability Test (M7-M18)

This task will develop and run the accelerated test methods for nanofluid properties of dispersion stability. The reliability test criteria will be refined from the initial targets of less than 5% degradation in absorbance and viscosity, reported to DOE for review and approval, and the durability (cyclic stability) of the nanofluids during the boiling-condensation cycles will be tested in an accelerated manner to simulate 5-year operation. This durability test will be extended to BP2 in Task 2.1 for a full length of service test (25 years). The physical properties of the fluid will be measured during tests to verify nanofluid stability. By the end of this task, at least one qualified nanofluid candidate that survives the accelerated durability test (i.e., particle segregation is less than 5% to avoid significant performance drop) will be selected and continued to Task 2.1. The LCOH estimation of the system, including material cost and maintenance, will be updated in Task 1.1 and Task 2.6 accordingly based on the test results.

Task 1.5: Evacuated Glass Solar Receiver Development (M4-M18)

This task will focus on developing a transparent evacuated glass solar receiver based on state-of-the-art back-surface absorbing tube technologies. The design criteria of the transparent evacuated tube will be identified, reported to DOE, and approved, and the anti-reflection coatings will be investigated to apply to the outer glass tube wall to decrease solar reflection, and low IR-emittance coatings will be investigated to apply to the inner glass tube material to suppress thermal emission. By applying coating technologies on glass surfaces, a technology for low-cost, double-wall evacuated glass tube with sufficient optical efficiency (>85% of standard solar spectrum light incident on the tube delivered to the nanofluid at

operational temperature, to be updated based on the modeling results in Task 1.1) will be developed by the end of this task.

Task 1.6: Loop Thermosyphon Performance Evaluation with Inclined Evaporator (M4-M15)

In this task, a series of thermal performance measurements will be performed on loop thermosyphons with their evaporating tubes inclined at different angles between 0º (horizontal) and 60º. The preliminary cost and performance requirement for the inclined collector will be generated by the model developed in Task 1, and the test data will be collected for the next stage prototype design and selection of solar concentrating accessories. By the end of the task, a range of evaporator inclining angles that provides cost and operation parameters (such as pressure head) that fit the design model developed in Task 1.1 will be nominated for next stage development.

Task 1.7: Stakeholder Engagement and Preliminary Market Research (M1-M18)

In this task, preliminary market research will be performed to understand the solar thermal desalination market, the key players, and potential partners for technology integration and commercialization. Types of stakeholders that may have different aspects of influence on this project will be identified, and various methods will be applied for early-stage stakeholder engagement, including publication, presentation, invention disclosure, press release, etc. At least six (6) potential partners among the stakeholders from at least two (2) different segments will be reached out to build a business relationship, and questions and comments to the technology developed in this project will be collected in the form of a survey or technology briefs from at least 2 of the stakeholders from 2 or more different segments. The opinions from stakeholders will be reported to DOE and used to guide the revision of the design in the future.

Task 2.1: Accelerated Durability Tests of the Nanofluid (M19-M30)

This task will continue the accelerated test of the long-term cyclic dispersion stability of the nanofluid candidates. The candidates selected from Task 1.4 during the boiling-condensation cycles will be tested based on the criteria identified and the facility fabricated in Task 1.4. The physical properties of the nanofluids will be measured during tests to verify material stability. This task will select at least one qualified nanofluid candidate passing the accelerated durability test in an accelerated manner to simulate a 25-year operational life. The LCOH estimation of the system, including material cost and maintenance, will be updated in Task 2.6 accordingly based on the test results.

Task 2.2: Accelerated Corrosion Tests of Nanofluids on Tube Materials (M19-M30)

The compatibility of the nanofluids with selected thermosyphon materials (glass, metal tube) during the boiling-condensation cycles will be tested in an accelerated manner to simulate a 25-year operating lifetime. The physical properties of the nanofluids and thermosyphon materials will be measured during the tests to record the material stability. Criteria to evaluate the material compatibility will be identified based on the model developed in Task 1.1, and a test plan will be generated and

submitted to DOE for review and approval. By the completion of this task and Task 2.1, at least one (1) qualified nanofluid candidate paired with feasible thermosyphon material will survive both the accelerated durability test and the corrosion test.

Task 2.3: Sub-Scale Prototype System (M19-M30)

A sub-scale loop thermosyphon prototype will be designed based on the system model developed in Task 1.1 and fabricated with the previously developed materials and off-the-shelf variable solar simulator and concentrator. A simulated solar light source and a heat sink will be used to demonstrate the thermal performance of the loop thermosyphon. Non-condensable gas mitigation strategies and low-cost manufacturing techniques for the glass-to-metal joint will be developed to maintain the high performance and hermiticity of the loop thermosyphon. The effect of working fluid charging volume and height difference between evaporator and condenser on the performance of the loop thermosyphon will also be evaluated experimentally. By the end of this task, a successful sub-scale prototype will demonstrate thermal performance consistent with the thermal performance of the modeling results.

Task 2.4: Thermal Cycling Testing for Loop Thermosyphon Materials (M22-M30)

This task will determine the life of the glass tube loop thermosyphon through thermal cycling. A custom thermal cycling system will be fabricated to test the glass tube material at representative thermal stress according to the coefficient of thermal expansion of both materials across the operating temperature range. The success of the test will be proven by maintaining the loop thermosyphon thermal performance after 9,200 cycles (25 years) within the allowance of performance decline determined by the model developed in Task 1.1. During this task, thermal cycling of the loop thermosyphon materials will be experimentally demonstrated for more than 3,700 cycles (>10 years) by the end of the Budget Period (BP) 2. This task will be continued in Task 3.2, BP 3, to demonstrate the performance through 9,200 cycles.

Task 2.5: Loop Thermosyphon System Model Revision (M28-M30)

In this task, the loop thermosyphon solar collecting system model developed in Task 1.1 will be reviewed and revised according to the test results in Budget Period 2, and an LCOH sensitivity analysis will be applied based on the cost estimation model. The loop thermosyphon system design to supply solar thermal energy at <\$0.01/kWh_{th} LCOH based on the updated model will be re-evaluated by a third-party company or organization approved by DOE.

Task 2.6: Stakeholder Engagement and Market Identification (M19-M30)

In this task, stakeholder engagement activities will be continued following Task 1.7. In addition to establishing partnerships with key industrial players, the recipient will conduct market research and verify by third-party stakeholders. Based on this market research, the potential market of the technology developed in this project will be identified. The market research report and the potential market identified will be submitted to DOE for review and approval by the completion of this task.

Task 3.1: Summary of Nanofluid Development (M31-M33)

In this task, the development and reliability tests of the solar-absorbing nanofluids will be finalized, summarized, and documented. By the end of the accelerated durability and corrosion tests, at least one qualified nanofluid candidate will be nominated based on the design parameters and test results for application in this loop thermosyphon solar collecting system.

Task 3.2: Summary of Loop Thermosyphon Life Tests (M31-M36)

In this task, the life tests of the loop thermosyphon system in Task 2.4 will be continued to determine the life of the glass tube loop thermosyphon through thermal cycling. Thermal cycling of the loop thermosyphon materials will be completed to demonstrate over 9,200 cycles (25 years) by the completion of this task.

Task 3.3: Mid-Scale Prototype Testing in Solar Simulator (M31-M33)

The testing of the prototype system from Task 2.3 will be completed. A simulated solar light source and a flat plate heat exchanger heat sink will be used to demonstrate the thermal performance of the loop thermosyphon. Before testing of the loop thermosyphon, a single-phase pumped water loop and coated steel receiver tube will be tested to calibrate the solar thermal input from the solar simulator based on calorimetry. Testing of the prototype system will be performed at different simulated solar inputs and working fluid charge volumes. The effectiveness of the working fluid volumetric absorption will be evaluated and the performance compared to the developed system model.

Task 3.4: Full-Scale Prototype Design, Fabrication, and Testing (M31-M39)

The overall system design will be completed based on the updated model developed in Task 2.7, and a full-scale prototype will be designed and fabricated accordingly. Either a Fresnel lens or a parabolic trough will be used as a solar concentrator, depending on the loop thermosyphon test results from BP2. A variable indoor simulated solar light source and a heat sink will be used to test the loop thermosyphon's performance. The testing procedure is determined, including the working cycle duration, testing parameters, operation procedure, system maintenance, and data management, and the test run of the system finishes the working cycle. With the full-scale prototype fabricated, the power load carried by the loop thermosyphon will be measured with the simulated solar input and heat dissipation. The complete prototype system is tested for at least 30 working cycles with at least three (3) selected solar input conditions each to draw a system performance distribution and efficiency matrix. The experimental results will be used to validate the system modeling, and the performance metrics for high thermal performance are realized.

Task 3.5: Market Strategy Development (M31-M42)

This task will continue the stakeholder engagement activities and start early-stage commercialization following the market strategy following Task 2.7. A market

strategy with a targeted market, funding and resource requirement, commercialization activity, and estimated commercialization performance will be developed with the support of industrial partners, targeting the market identified in Task 2.7.

Narrative Report and Final Update

Program Overview and Objectives

Advanced Cooling Technologies, Inc. (ACT) and the University of Maryland at College Park (UMD) proposed to develop an innovative solar thermal collection system for efficient, low-cost solar thermal desalination.

The proposed concept featured graphene oxide-based surfactant-free aqueous nanofluids and a high-power two-phase (boiling and condensing) loop thermosyphon to cost-effectively and passively acquire and transfer heat at high thermal efficiencies. The graphene oxide-based aqueous nanofluid would be engineered to be efficient directly absorb solar energy over a broad wavelength range. The two-phase nanofluid would naturally circulate in the loop thermosyphon, allowing for thermal energy transfer at rates much greater than conventional heat transfer systems. The solar receiving portion of the loop thermosyphon will feature a thin film-coated vacuum glass tube with a high solar-to-thermal absorption efficiency, low thermal infrared emissivity, and vacuum insulation. During the daytime, solar radiation would be concentrated by a Fresnel lens onto the glass tube solar receiver and absorbed by graphene oxide nanoparticles in the working fluid, which boils the saturated working fluid. The two-phase nanofluid flow transports heat through the latent heat of vaporization to a condensing heat exchanger located in a steam-generating boiler, where the heat is used to generate steam from brackish water. The proposed solar collection system was designed to reliably supply solar energy to supply various thermal desalination systems with no moving parts (pump) and at a high thermal efficiency. Benefited by the high solar-to-thermal conversion rate of the direct absorption solar receiver and the lowered material and operation cost of the loop thermosyphon, a levelized cost of heat (LCOH) of less than $0.01/kWh was proposed for system. Figure 1 presents the initial concept design proposed at the beginning of the 3-year project.

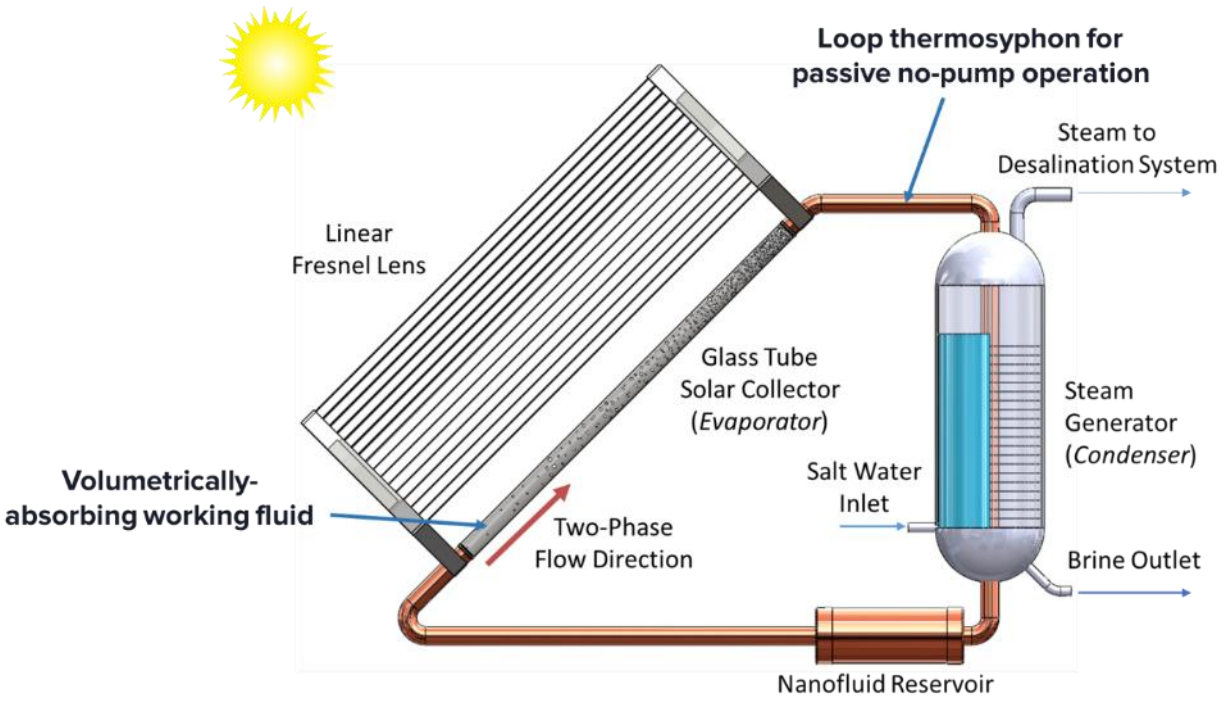

Figure 1: Solar-Driven Desalination System with Volumetrically-Absorptive Two-Phase Working Fluid Operating in a Loop Thermosyphon Configuration

The 3-year project was divided into four parallel technology development pathways completed alongside business development and reporting tasks. The four technology development pathways are as follows:

1. Development, characterization, and testing of the volumetrically absorbing two-phase working fluid.
2. Design and fabrication of the glass receiver and associated corrosion and thermal cycle testing.
3. Modeling, design, fabrication, and testing of the two-phase loop thermosyphon used to circulate the working fluid and thermal energy from the receiver to the steam generator.
4. Fabrication and demonstration of integrated systems (working fluid, receiver, and loop thermosyphon) at different scales.

During the business development task, ACT evaluated the potential market for this technology and reached out to market stakeholders to develop a tech-to-market strategy for the commercialization of the technology during the project.

This report is structured around the four technical pathways and shows how the specific project tasks fit into these pathways and how the team overcame challenges to complete the overall program objectives.

Project Results and Discussion – Working Fluid Development

Tasks 1.2, 1.3, 1.4, 2.1, and 3.1 contain the working fluid development completed throughout the three-year program. The following section summarizes the work and key findings of these Tasks.

***Task 1.2**: Identify a nanofluid solution based on graphene oxide to demonstrate the nanofluid's high optical to thermal efficiency and capability against segregation by literature review.*

As presented in the design of the loop thermosyphon solar collection system, incident solar radiation passes through the glass receiver tube and is converted to thermal energy when absorbed by the dark nanofluid. When exposed to solar irradiation, the nanofluid in the evaporator boils, becoming a two-phase flow passively circulating around the loop thermosyphon. An absorbing efficiency, η_{abs}, approaching 100% was expected for a nanofluid having a sufficient solar-absorbing nanoparticle concentration. The in-situ boiling of the working fluid on the surface of the nanoparticles features minimized thermal resistance in the solar-to-steam process and maximized heat transfer area, thus allowing highly-concentrated solar heating of the working fluid without significant thermal gradients and exergy loss. As a result, the solar-thermal conversion and solar thermal energy collection can be more efficient.

In addition to serving as the volumetric solar absorption media, the nanofluid is also the working fluid of the loop thermosyphon. The thermal performance of a two-phase working fluid is primarily determined by its thermal conductivity, viscosity, latent heat of vaporization, critical heat flux (CHF), and stability.

The requirements identified for a successful nanofluid in the present application include the following:

- Good solar absorbance over the entire solar spectra;
- A significant density difference between the vapor and liquid phases.
- Insensitive to concentration change and flow circulation, i.e., surfactant-free;
- Excellent stability and reliability for long-term (10s of years) use;
- Compatible with tube wall materials (glass and metal;)
- Low viscosity, high thermal conductivity, high latent heat of vaporization, high CHF, etc.

In Task 1.2, these requirements were used to identify an optimal nanofluid. First, a literature review was completed to identify nanofluids with the desired light absorptivity, stability, viscosity, and thermal conductivity. After comparing physical properties between different nanofluids, graphene, graphene oxide, and reduced graphene oxide were all selected due to their performance in the reported tests.

For the volumetric absorption of solar light through the glass tube in the loop thermosyphon solar collection system, the nanofluid should achieve a high absorption rate in the sunlight wavelength range without the requirement of high absorbance at all wavelengths. Luo et. al. reviewed and compared the transmittance between different light-absorbing nanofluid. Nanofluids of carbon-based materials, including both carbon

nanotube (CNT) and graphene (C) nanofluids, are suggested to be the most suitable light-absorbing materials due to their low transmittance. Luo et al. evaluated graphene nanofluids vs. concentration as shown in Figure 2. A low transmittance (i.e., high absorbance) is suggested to be achievable with graphene concentrations greater than 0.01%.

Graphene-based nanofluids have been shown to have good stability both with and without surfactants. Ye et al. studied the long-term stability of three graphene-based nanofluids under various water chemistry conditions [2]. In the absence of additives, graphene oxide (GO) nanofluid remains stable over 21 days, while graphene nanoplatelet (GNPs) and reduced graphene oxide (RGO) nanofluids are less stable compared to GO nanofluids.

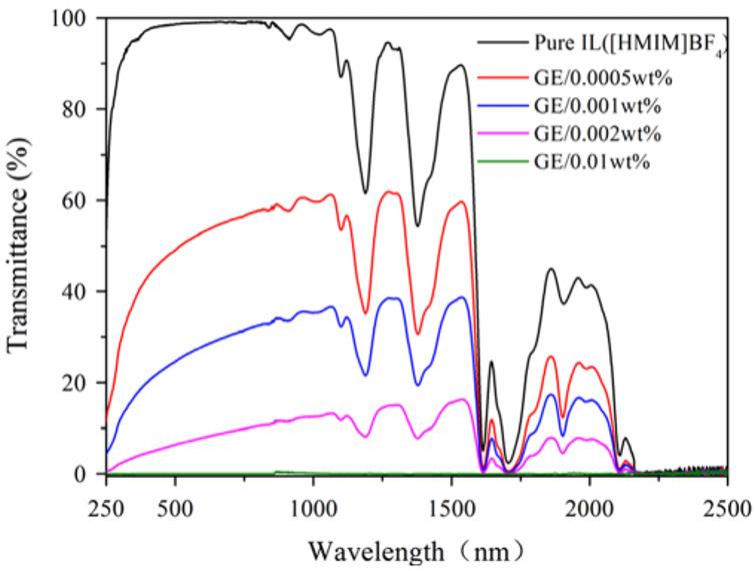

Figure 2. The transmittance data of graphene/[HMIM]BF_4 nanofluids, by Liu et al. [**1**]

As presented in the literature, the surfactant-free graphene/GO-based nanofluids feature good solar absorbance over the entire solar spectra, with good stability, and are suitable for the loop thermosyphon solar collection application. Because of this, it was initially decided to analyze a GO nanofluid for use in the solar-driven loop thermosyphon.

***Task 1.3**: Synthesis and Thermophysical Characterization of the Nanofluids.*

Graphene Oxide-Based Working Fluids

Graphene oxide (GO) in water at various concentrations was prepared for analysis. Properties including atomic ratio, viscosity, and particle size were measured along with spectral light transmittance. Long-term two-phase stability was investigated at room temperature. GO nanofluids were purchased from different manufacturers with initial concentrations as listed in table 1. Each nanofluid was first sonicated using an ultrasound bath (Branson B300, 50W, 34 kHz) for 2 hours, then further diluted with purified water to prepare samples of differing concentrations. Each sample completed a second 15-min bath sonication before testing. Three (3) different types of GO nanofluids were tested. Table 1 presents the basic information about the three GO samples examined.

Table 1: Basic Information About GO Test Samples Tested

Manufacturer	Name	Label	Solvent	Surfactant	Initial Conc.
Graphene supermarket	Single Layer GO	Sample 1	H_2O	/	0.05wt%
Graphene supermarket	Highly concentrated GO	Sample 2	H_2O	/	0.5wt%
Graphenea	GO dispersion	Sample 3	H_2O	/	0.4wt%

The light absorbing ability of the three samples was compared by measuring transmittance at the same concentration with an ultraviolet–visible spectrophotometer. Figure 3 presents spectral transmittance for the three GO nanofluids. When all three (3) samples are compared under the same concentration (0.05wt %), sample 2 showed the lowest transmittance.

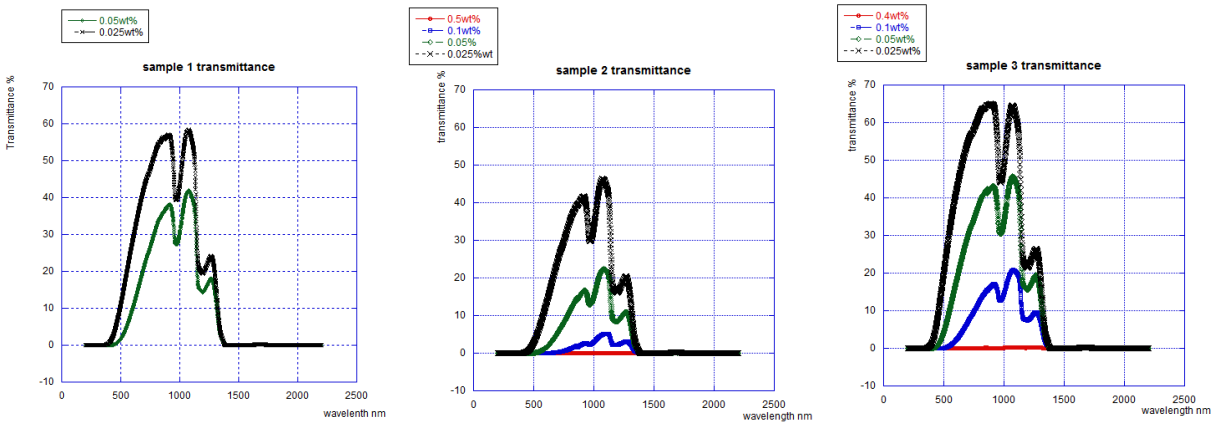

Figure 3. Transmittance Spectra of Sample Series 1, 2 and 3 for Different Nanoparticle Concentrations.

Transmittance data for different samples was combined with the solar irradiance spectra to calculate the light absorbing ability. Across the solar spectrum between 200nm to 1700nm, 94.4% of irradiance can be absorbed by Sample 2 at 0.05wt%. When the concentration decreases to 0.025wt%, only 66.7% of solar power is absorbed by sample 3, which has the lowest atomic ratio of C to O.

Due to the atomic ratio difference between Sample 2 and Sample 3, these two samples were further investigated for long-term stability. Stability was examined at room temperature by monitoring the transmittance change over 30 days with the ultraviolet-visible spectrophotometer. Figure 4 shows that Sample 2 transmittance at 600nm increased from 1.4% to 5.9% after 30 days. Sample 3 only dropped a little from 13.8% to 12.9% across the same time. The smaller change in transmittance for Sample 3 indicates relatively higher stability. Despite this difference, according to The Beer-Lambert Law, a maximum 55% transmittance is allowed for the test conditions (10mm cuvette) to meet the requirements of the solar concentrator. All three samples meet this requirement.

As shall shown in the discussion of Task 1.4, the GO nanofluid was found to experience significant transmittance increases after only a few days of boiling/condensation testing. This is in contrast to static elevated temperature (120°C) testing, where the transmittance remained relatively constant with increasing test time.

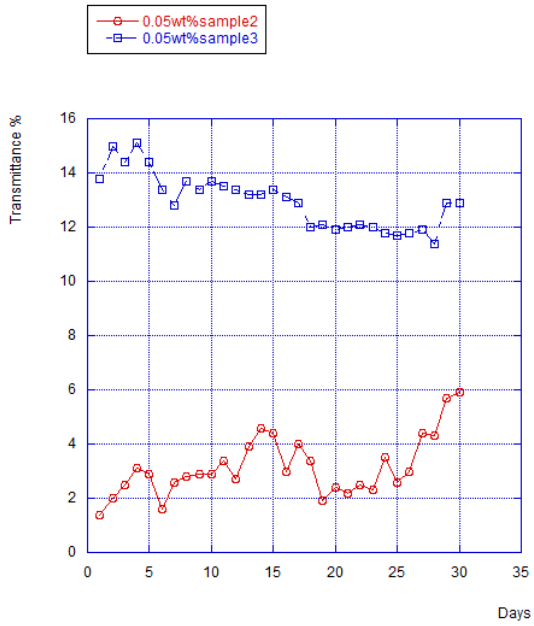

Figure 4. The Transmittance of GO Nanofluid at 600nm as a Function of Time.

A series of mitigation strategies have been explored in this study to address the observed thermal reduction of GO nanofluids under the boiling-condensation condition, which include a pH control method, GO particle functionalization with surfactant, and mixing of the GO nanofluid with nanocellulose. It was found that the introduction of nanocellulose is a promising method to stabilize GO under boiling-condensation conditions. In addition to the nanofluids with GO nanoparticles, a solution of organic dyes has been investigated. The dye solutions are thermodynamically-stable, molecular-level solutions. Initial experimental results suggest that the dye solution has excellent stability when undergoing boiling-condensation cycling. Details for each method are given below.

pH Control Stabilization Method

To help mitigate GO agglomeration and increases in transmittance, a pH control method was investigated. As mentioned in many nanofluid experiments, the stability of an electrostatically stabilized dispersion is strongly dependent on pH. Li et al. found zeta potential to decrease as pH increased, resulting in a more electrostatically stable nanofluid [3]. A pH-tuned GO nanofluid was prepared with buffer solution (NaH_2PO_4/ Na_2HPO_4) and was subjected to boiling-condensing cycling. Each cycle consisted of 24-hours of boiling and 12-hours of cooling. As seen on the left side of Figure 5, the sample only remained stable for the first daily cycle without severe agglomeration after tuning the pH from 4.8 to 8.1. After cycle 2, the stability broke down.

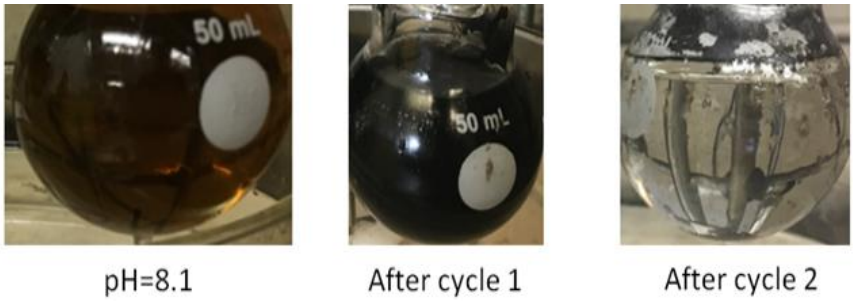

Figure 5: Boiling-Cooling Cycle Test Results for pH Tuned GO Sample

Functionalization with Surfactant

Another method explored to minimize agglomeration was functionalization of the GO particles with a surfactant. A more stable nanofluid was expected by isolating the GO particle with surfactant molecules. Since water was used as a continuous phase in the experiment, a surfactant with relative higher HLB (hydrophile-lipophile balance) value, for example CO630, was selected for testing. Transmittance results for this testing are presented in Figure 6. Compared to the GO nanofluid without surfactant, the deterioration in stability slowed. However, a significant deterioration in stability was observed after only 5 cycles.

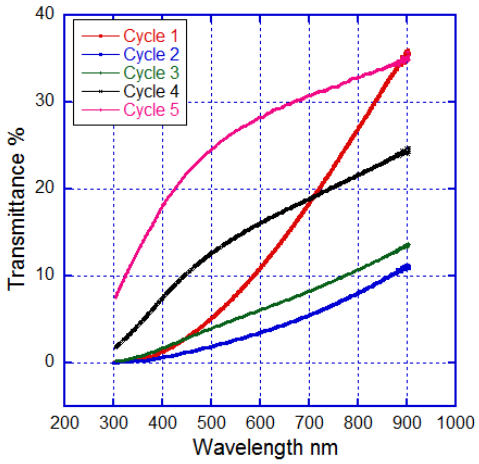

Figure 6: Transmittance Data of CO-630-Functionalized GO Sample

Functionalization with Nanocellulose

Because of the instabilities found during boiling-condensation of GO nanofluids mixed with water, nanocellulose was introduced into the GO nanofluids. The GO nanofluids were mixed by sonication and had a concentration of 0.01 wt%. Nanocellulose nanofluid with a 0.1 wt% concentration was prepared using a pulsed 1-hour ultra-sonication before being mixed with the nanofluid. The transmittance of the nanofluid was measured after each cycle with results shown in Figure 7. The transmittance of the prepared GO/nanocellulose nanofluids changed little during the first 10-cycle boiling test. However, transmittance began to slowly increase as the experiment progressed. After more than 14 cycles, agglomeration and separation are severe enough to lead to a gradual transmittance increase, making the nanocellulose-modified nanofluid unsuitable as a working fluid for the solar-driven LTS.

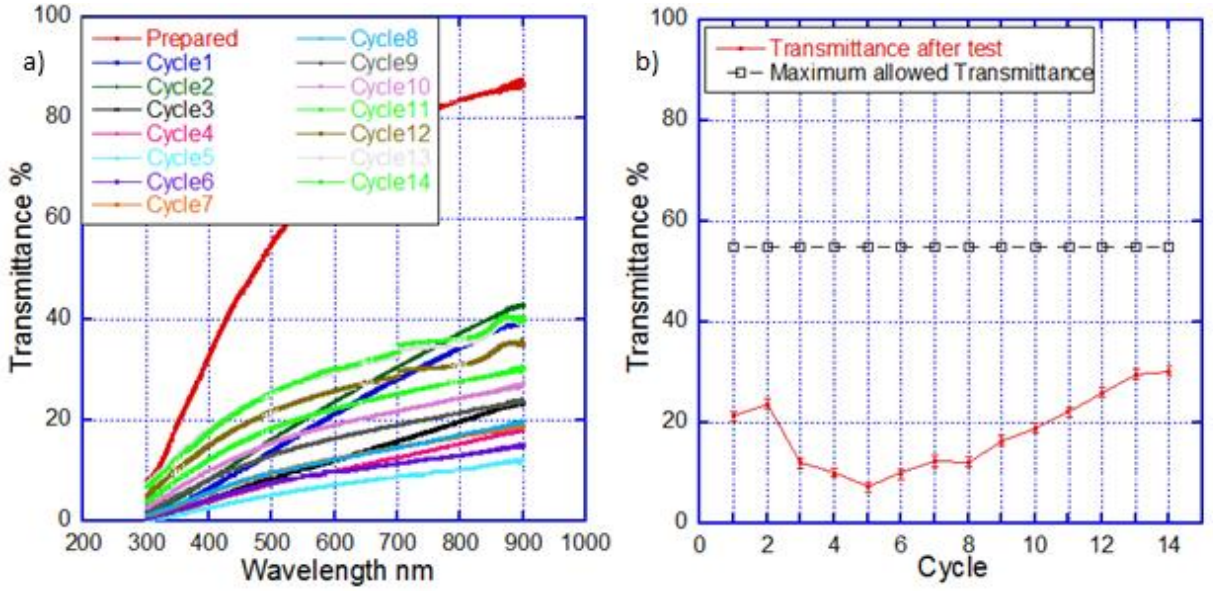

Figure 7: (a) Transmittance as a Function of Wavelength and (b) Transmittance at 600nm as a Function of Time (or Cycles) in the GO/Nanocellulose Nanofluid.

Thermal conductivity of the prepared graphene oxide (GO) nanofluid was measured using the 3Ω-wire method for GO nanofluids with various concentrations and at temperatures of 20°C, 70°C, and 90°C. As seen in the left-hand side of Figure 8, the measured thermal conductivity of the GO nanofluid increases with increasing GO concentration. The viscosity of the samples was measured at different temperatures using a viscometer. Figure 8 (right) shows that the viscosity of the GO nanofluid samples follows a similar trend to that of water, decreasing with temperature.

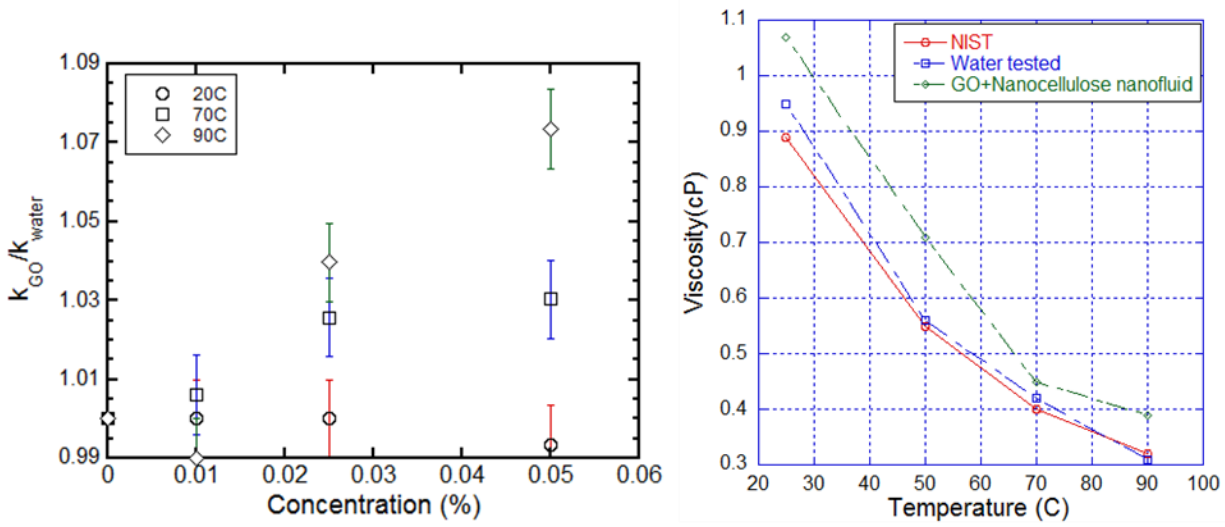

Figure 8: (left) Measured Thermal Conductivity of GO Nanofluid; (right) Measured Viscosity of GO/Nanocellulose Nanofluid after 11 Boiling Cycles

Thermodynamically Stable Solution of Organic Dye in Water

Because of the poor performance of the GO nanofluid, organic dye solutions were considered as substitute working fluids. To identify a dye mixture with good spectral absorptivity, an initial transmisivity study was completed. Initially, a 1:1 ratio of Basic yellow 9 and Basic blue 3 was tested, which yielded results with ambiguous degradation specifications. The aforementioned new dye mixtures that are less susceptible to photodegradation were purchased and prepared at 0.002 g/mL. These samples were then tested in a photospectrometer to determine the transmissivity as a function of wavelength with results shown in Figure 9. Acid Black 52 most closely matched the transmittance data of the original dye mixture (Basic yellow + Basic blue 3) and an additional quantity was synthesized for further testing. Subsequent stability testing suggested that Acid Black 52 be used as the dye of choice.

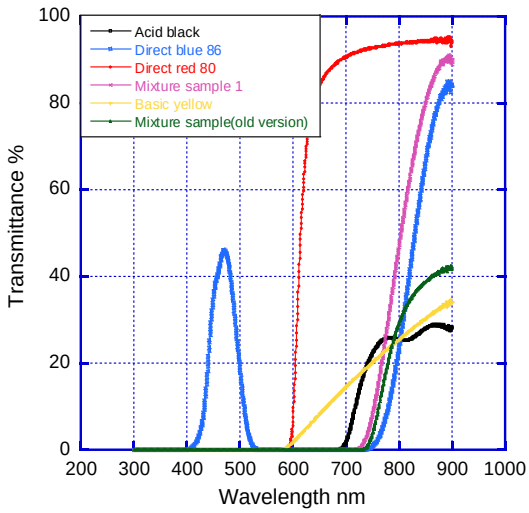

Figure 9: Transmittance vs. Wavelength Data for Several New Dye Options Compared to the Previous Dye Mixture (Basic Yellow 9 + Basic Blue 3).

Task 1.4: *Develop and run the preliminary accelerated test methods for nanofluid properties of dispersion stability*

Experimental Setup

The experimental setup for the cyclic boiling-condensation tests is presented in Figure 10. Test samples were boiled by immersion into a 120°C oil bath, with vapor condensed by a chilled water loop. A complete cycle takes 24 hours, consisting of a 12-hour boiling-condensation phase and 12-hour resting phase (without heating).

As shown in Figures 6 and 7, preliminary boiling-condensation testing of graphene oxide (GO) nanofluids revealed that thermal reduction of the nanofluids was occurring at a much lower temperature than expected; around 110°C. When the thermal reduction of GO nanofluids reaches a certain threshold, agglomeration of GO nanoparticles occurs and the fluid becomes unstable. Nanocellulose was found to stabilize GO nanofluids for a longer period of cycling, but eventually, this partially-stabilized nanofluid also began to agglomerate. Apart from GO nanofluids, other types of thermodynamically stable

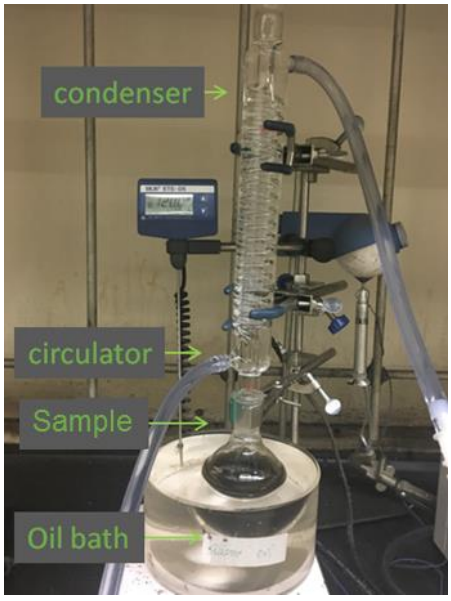

Figure 10: Experimental Setup for Boiling-Condensation Tests

solutions, such as rhodamine B-based dyes, have been identified and tested. Both a dye mixture and existing dye formulation with better stability and optical efficiency than GO nanofluid were identified. In particular, the Acid Black 52 organic dye was identified as having excellent absorptivity properties across the solar irradiance spectrum.

Using the boiling and condensing test unit presented in Figure 5, the team completed boiling/condensing cycles for both Acid Black 52 dye. 25 complete daily boiling/condensing cycles were completed with spectal transmittance measured by UMD after each cycle. Figure 11 (left) presents measured transmittance of the Acid Black 52 vs wavelength and cycle number. Figure 11 (right) presents the transmittance at 800nm vs cycles.

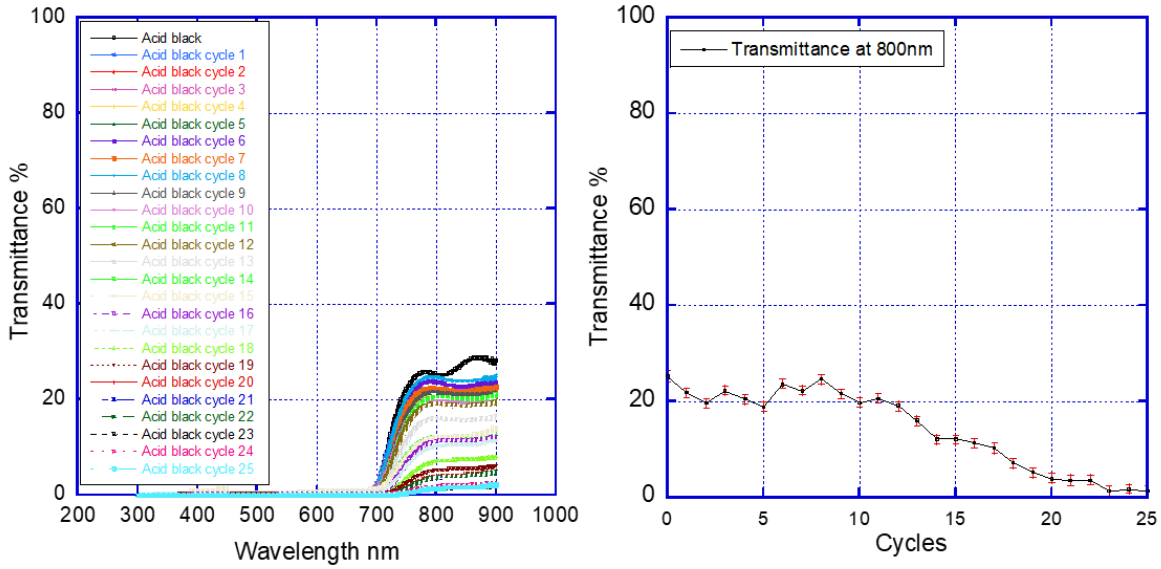

Figure 11. (left) Transmittance Data for Acid Black 52 in the Boiling/Condensing Setup at UMD, and (right) Transmittance vs. Cycle Number at a Wavelength of 800nm.

When tested under boiling-condensing conditions, the optical transmittance of the Acid Black 52 dye was found to decrease with increasing cycle number – through 25 cycles. Overall, the dye showed both better optical efficiency and better stability than the GO nanofluids.

Dye Thickness

Thickness of the dye layer is a critical parameter in calculating the total volumetric absorption of the working fluid. For most of the 300-900nm spectral transmission tests, a 10mm thick rectangular test vial was used. If this vial were thinner, measured transmittance through the thinner dye layer would increase, while the opposite effect would occur for a thicker dye layer. Variations in absorption between wavelengths of 300 and 3000nm were calculated for dye thicknesses between 2 and 30mm (Figure 12). For dye thicknesses less than 8mm, absorption between 300 and ~2000nm is seen to be greatly reduced. In contrast, if the dye thickness is greater than ~20mm, absorption is consistently close to 1, except for a slight decrease in the region of 1000nm.

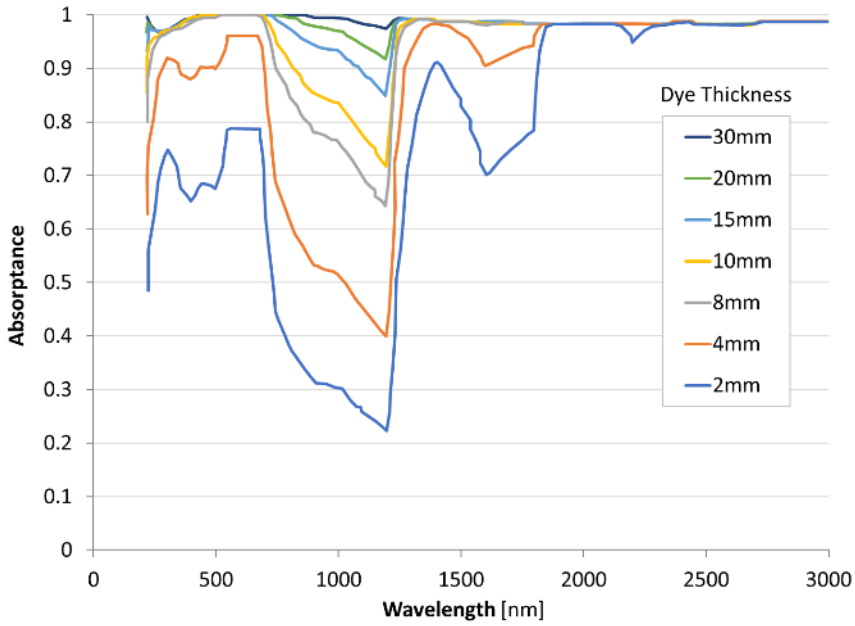

Figure 12: Spectral Absorptance for Different Dye Mixture Thicknesses

By integrating the spectral absorption results of Figure 12 with respect to the solar intensity spectrum, total spectral absorption can be obtained for the different dye thicknesses. Solar intensity (*I*) was estimated using Planck's blackbody radiation function at a temperature of 5,785K:

$$I(\lambda,T) = \frac{C_1}{\lambda^5\left(exp^{\frac{C_2}{\lambda T}} - 1\right)} \quad (1)$$

Where λ is the wavelength, $C_1 = 11{,}910\,\frac{W\mu m^4}{cm^2}$, and $C_2 = 14{,}400\,K\mu m$. Integrated results of spectral absorption with respect to solar intensity are presented in Figure 13 vs. dye thickness. At dye thicknesses less than 10 mm, total spectral absorptance decreases sharply with decreasing thickness, while at thicknesses greater than 20 mm, total spectral absorptance approaches 1. This critical thickness is important when considering the minimum viable system size and maximum void fraction within the receiver. If the tube diameter is too small, volumetric absorption will suffer. Likewise, if a very large percentage of the flow cross-section is vapor vs. liquid, the thickness of absorptive liquid may be too thin to fully absorb the incident irradiance.

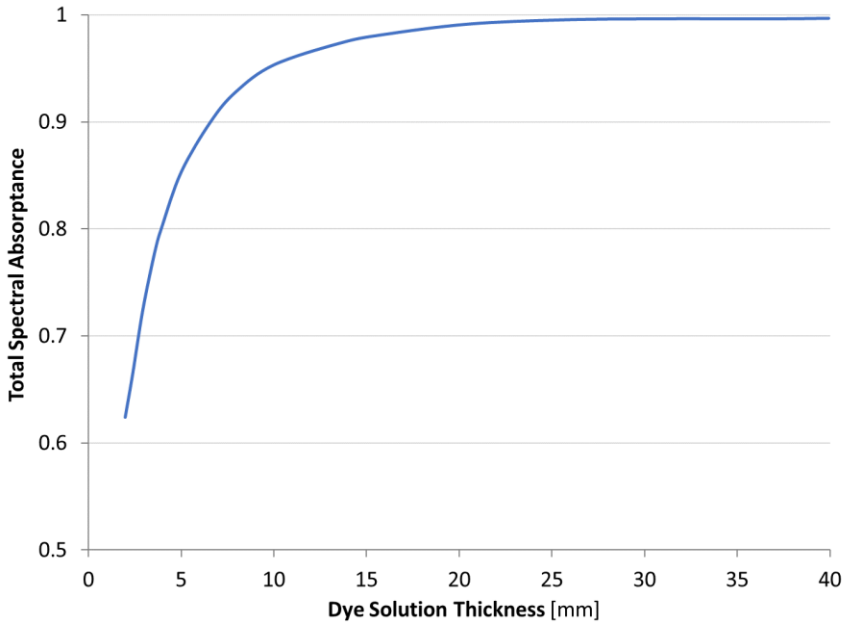

Figure 13: Total Solar Collector Absorptance vs. Dye Mixture Thickness

Task 2.1: *Accelerated Durability Testing of the Nanofluid to Ensure Long-Term Performance*

Task 3.1: *Summary of Nanofluid Development*

Dye Stability During Operation in the Loop Thermosyphon

The thermal stability of the Acid Black 52 was further tested by continuous boiling/condensing in a glass loop thermosyphon fabricated at ACT (Figure 14). The evaporator of this LTS is heated by a Nichrome wire wrapped around the horizontal evaporator. The two-phase dye mixtures rises to the condenser, where it is condensed by cold water supplied by a chiller. The LTS was initially charged with ~120 mL of dye, with ~10 mL samples removed at periodic intervals for transmittance testing by UMD. The system was maintained at a dye saturation temperature of 95°C throughout the test. The purpose of this test was to verify the long-term thermal stability of the Acid Black 52 dye when subject to conditions representative of those in an LTS.

Dye samples were removed from the LTS for transmittance testing after 8, 16, 32, 64, 136, and 199 days. All transmittance measurements were completed by UMD using the same methods employed for their samples taken from the boiling/condensation test apparatus (Figure 10).

The spectral transmittance of the thermally tested dye samples through 199 days is presented in Figure 15. These results are promising as they indicate no clear increase in transmittance with increasing test time. After 8 days, transmittance did increase at wavelengths greater than ~700 nm. However, after 199 days, further significant increases were not observed. The only discernable change over time is a slight relaxation of the curve, where it does not rise to the maximum transmittance value as quickly at wavelengths greater than ~700 nm. While this may indicate a physical change within the

structure of the dye, transmittance values remain low suggesting there is a minimal impact on the absorptivity of the working fluid.

Figure 14: Glass Loop Thermosyphon During Continuous Acid Black Thermal Testing

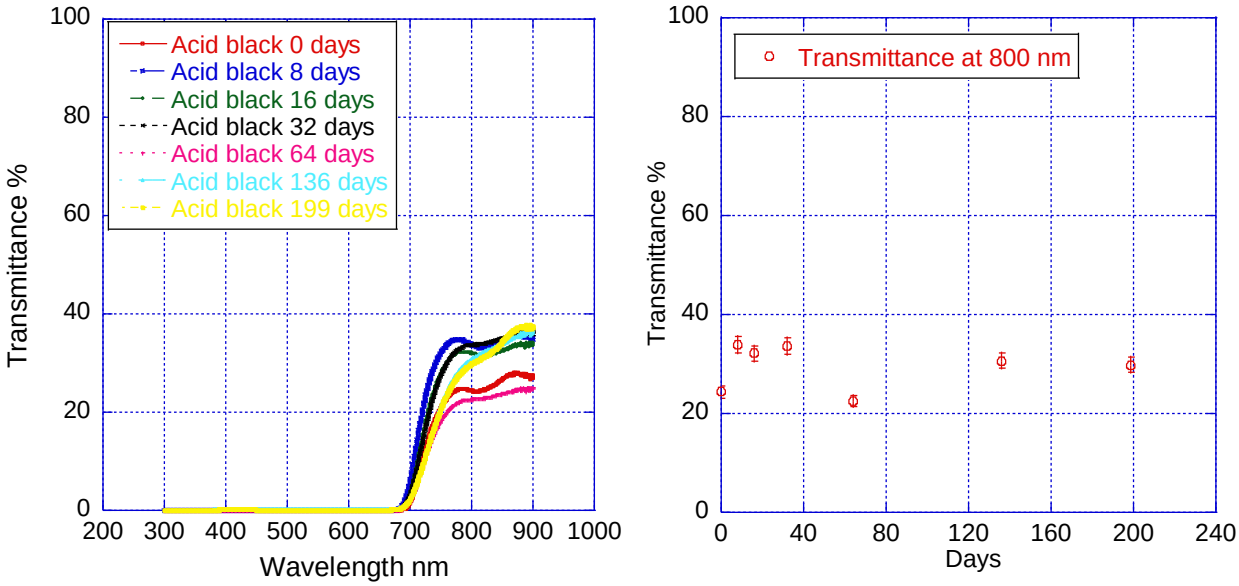

Figure 15: Transmittance of Acid Black Dye Through 199 Days of Continuous Operation in the Glass Loop Thermosyphon (left) vs. Wavelength and (right) vs. Operation Time at 800nm

Degradation of the dye was also examined by the infrared attenuated total reflection (ATR-IR) method. This method allows the molecular bonds of the dye sample to be examined. The ATR-IR results for the LTS thermal samples are presented in Figure 16.

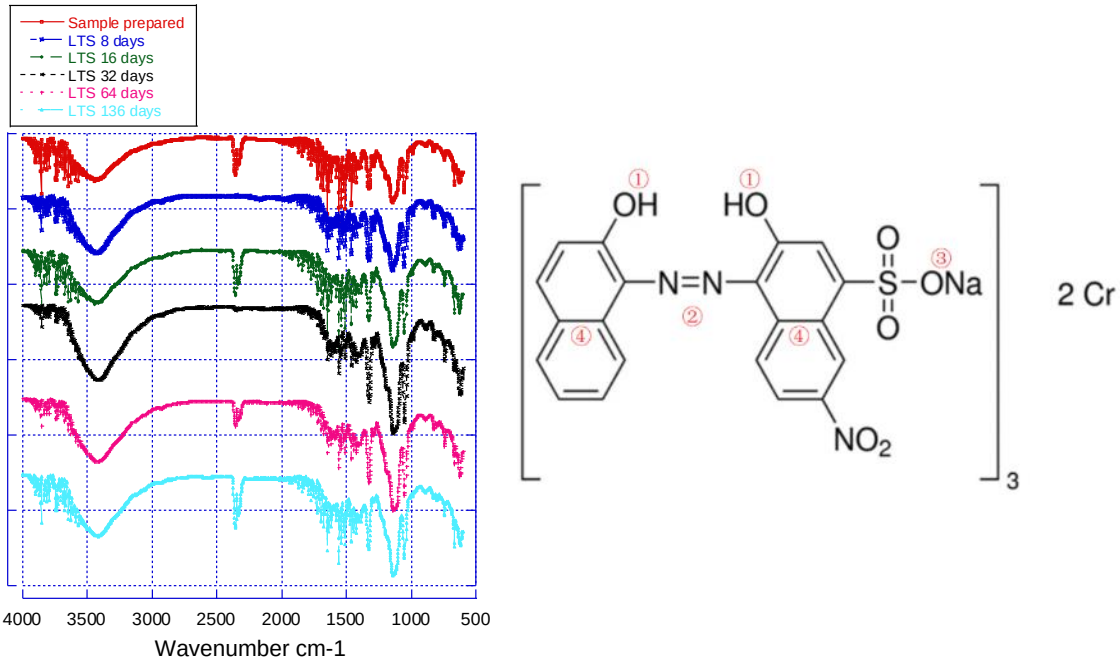

Figure 16: (left) ATR-IR Results for LTS Thermal Test Samples and (right) Acid Black 52 Dye Molecular Diagram

The peaks in the ATR-IR curves correspond to specific molecular bonds (labeled 1 through 4) presented in Table 2. As seen in Figure 16, the ATR-IR intensity curves are very consistent through 136 days of testing with the primary difference being in the CO_2 peak at a wavenumber of 2,400 cm^{-1}. This is environmental CO_2 contaminating the sample and can thus be ignored in this analysis. Given the similarity in ATR-IR intensity curves across the samples, the conclusion can be made that thermal testing in the glass LTS does not significantly change the structure or composition of the acid black 52 dye molecules.

Table 2: Molecular Bonds and Wavenumbers for ATR-IR Analysis

Bond #	Bond	Wavenumber(s) [cm^{-1}]
1	-OH	3,366, 3,471
2	N=N	1,550
3	R-SO2-ONa	1,420 – 1,330 1,200 – 1,145
4	Naphthalene	3,200
Other	CO_2	2,400

UV Degradation Testing

A UV degradation test setup was constructed to test the long-term dye stability during exposure to concentrated UV light. The designed UV test setup is presented in Figure 17. A 100W, 365 nm, UV LED array is mounted above a cylindrical dye chamber, with an optics used to direct a cone of light onto the dye. The 100 W_e, 365 nm UV LED array provided a nominal flux of 394 W/m^2 on the surface of the 5" diameter dye reservoir. While this is well below the typical total solar flux of ~1000 W/m^2, it is approximately 5 times the flux of the UV portion of the solar spectrum. Light passes through the transparent dye chamber cover and is directly incident on the dye. A fill/drain port located on the side of the dye chamber is used for filling and draining of the dye, with dye removed for testing at a specified interval. The LED array is cooled via a heat sink and integrated fan, with the dye chamber cooled by a similar heatsink/fan system. Two identical UV test systems were fabricated to allow for repeatable measurements between independent samples.

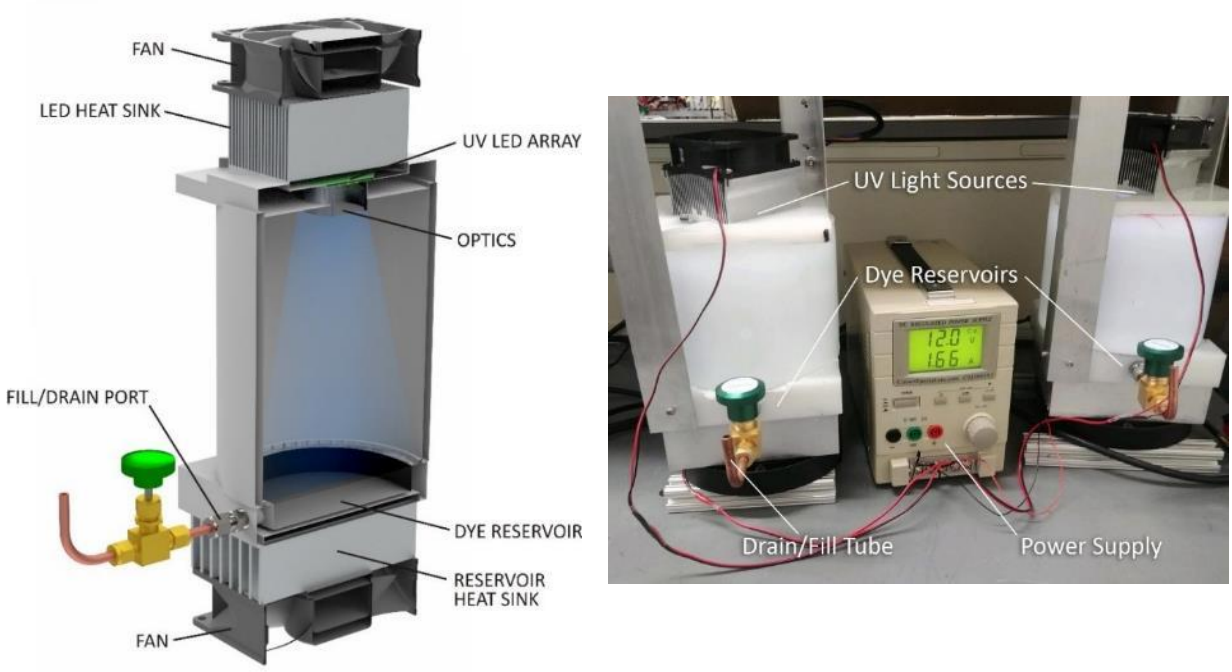

Figure 17: (left) UV Test Setup Design and (right) Dual UV Test Systems during Testing

Transmittance Results for UV Testing

Dye UV testing was continued for 257 days, with samples removed periodically for transmittance testing by UMD. Sample spectral transmittance results through 257 days are presented in Figure 18. Through day 23, the samples from both test setups (UV-1 and UV-2) show very similar transmittance trends with no significant change in transmittance noted during the test period. After 23 days, the samples from UV-1 exhibit a slight increase in transmittance, while those drawn from UV-2 show no significant change in transmittance through day 96. These differences are slight and between 96 and 128 days the samples once again appeared to stabilize. At 191 days, both UV-1 and UV-2 show an increase in transmittance at wavelengths greater than 750 nm. This trend continues for UV-1 through 257 days, while UV-2 shows a marked decrease in

transmittance at 257 days. It is believed that this drop is not an accurate indication of the actual dye performance, and it is likely due to either sampling or measurement errors.

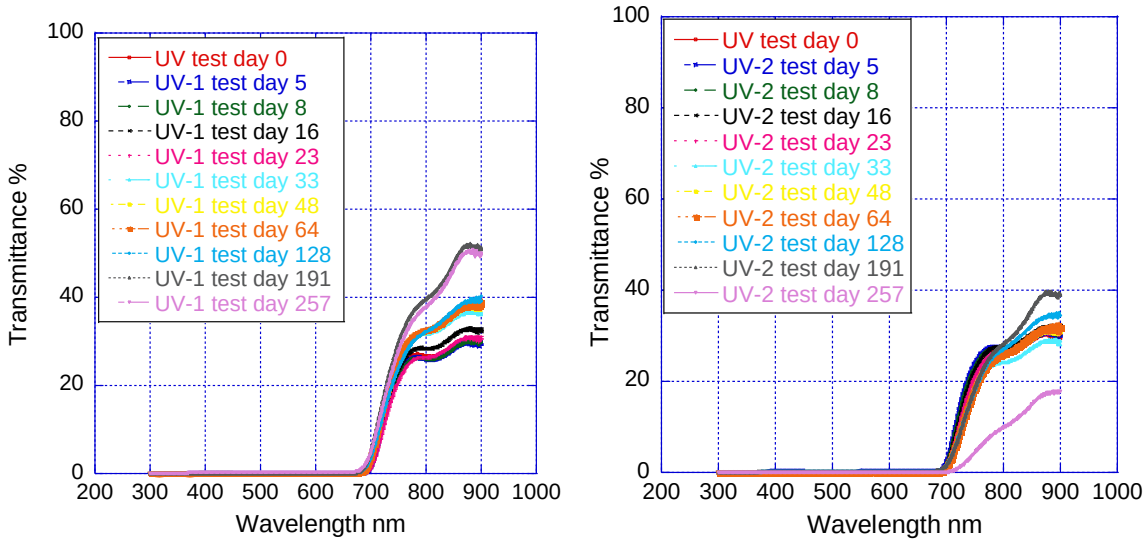

Figure 18: Transmittance of the Dye Samples Through 257 Days of Concentrated UV Exposure

An ATR-IR analysis was also conducted on the UV test samples through 191 days of testing. The results of this testing for the UV-1 samples are presented in Figure 19. Like the ATR-IR analysis of the thermal test samples, the UV test samples show good long-term structural stability with little difference in the intensity peaks across the test period.

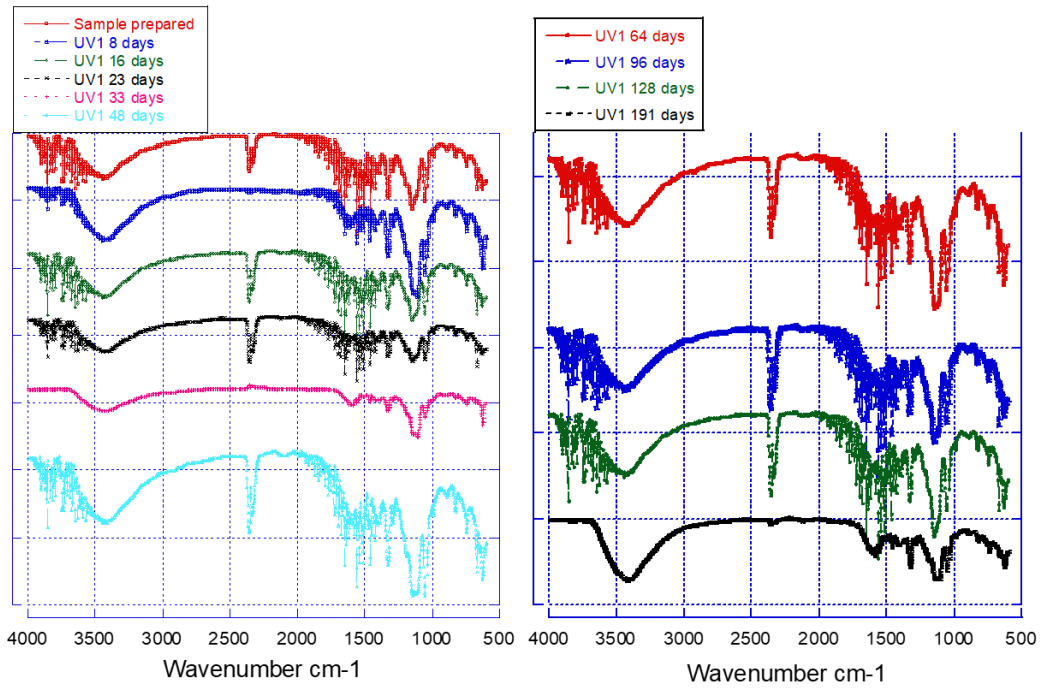

Figure 19: ATR-IR Analysis Results for the UV1 Test Sample Through 191 Day

Conclusion

The promising long-term thermal and UV stability of the acid black 52 dye leads to the conclusion that it will continue to provide a high level of irradiance absorptance across a 25-year system lifetime. For this reason, Acid Black 52 was selected as the working fluid for the full-scale prototype system fabricated during Task 3.3.

Project Results and Discussion – Glass Receiver Development

Tasks 1.5, 2.2, 2.4, and 3.2 contain the glass receiver development completed throughout the three-year program. The following section summarizes the work and key findings of these Tasks.

Task 1.5: *Develop a double-wall evacuated glass tube with sufficient optical-to-thermal efficiency*

The goal of this task was to develop a double-wall evacuated glass tube with an optical efficiency of 85% or above. Borosilicate glass was selected due to its high solar transmittance, high chemical resistance, and good thermal shock resistance. We characterized the transmittance of Borosilicate glass over the solar thermal spectral range, for both a single and double glass layer. This optical characterization demonstrated that the double-wall borosilicate glass solar receiver could satisfy our design requirements, if the heat transfer fluid could absorb virtually all of the incident solar irradiation (e.g., solar absorptance = 0.995).

Glass-Metal Joint Challenge and Fabrication

One significant challenge is the glass-metal seal fabrication. Metals have a greater coefficient of thermal expansion (CTE) than borosilicate glass. For example, a copper tube has a CTE of 17×10^{-6}/K, five times of borosilicate glass. The mechanical stress generated by this large CTE mismatch will break the metal-glass joint during thermal cycling.

There are a few approaches to manufacturing glass to metal joints, including the Houskeeper method, and commercial vacuum fittings. For direct glass/metal joints, metals or alloys with a CTE similar to that of glass are needed. Kovar (Ni-Co-Fe alloy) is a popular alloy for metal/glass joints and is used in applicaitaons, such light bulbs. It was decided to use Kovar to make the glass-metal joint. Figure 20 presents a photo of a Borosilicate glass-Kovar joint fabricated using the graded seal method.

Figure 20: Borosilicate Glass-Kovar Joint Fabricated Using the Graded Seal Method.

Glass/Kovar Stress Analysis & Pressure Testing

A theoretical stress analysis of the glass-to-metal joint based on thin shell and thermal stress theory was completed. While glass can endure compressive stress, it handles tensile stress poorly. The axial stresses component (σ_{xg}) is tensile on the outer surface of glass tube but compressive on the inner surface. σ_{xg}^{total} is typically the largest stress component on the glass tube. Therefore, the axial stress at outer surface is used to investigate the effects of different parameters on the maximum stress on the glass tube.

The maximum axial stress occurs at a point only a few millimeters from the sealing joint between the glass and metal. Figure 21 presents the stress on the glass/Kovar joint as a function of distance from the joint (x). The axial stress on the glass tube is sensitive to the thickness of the Kovar ring and the glass. When the glass-metal seal is operating at elevated temperature, a smaller diameter glass tube helps to reduce the maximum stress. Operating at higher pressure (or temperature) inside the glass tube increases the maximum stress level in the tube, as expected. The results indicate that the most effective way to reduce stress in the glass tube is by using a thin metal ring and thicker glass tube.

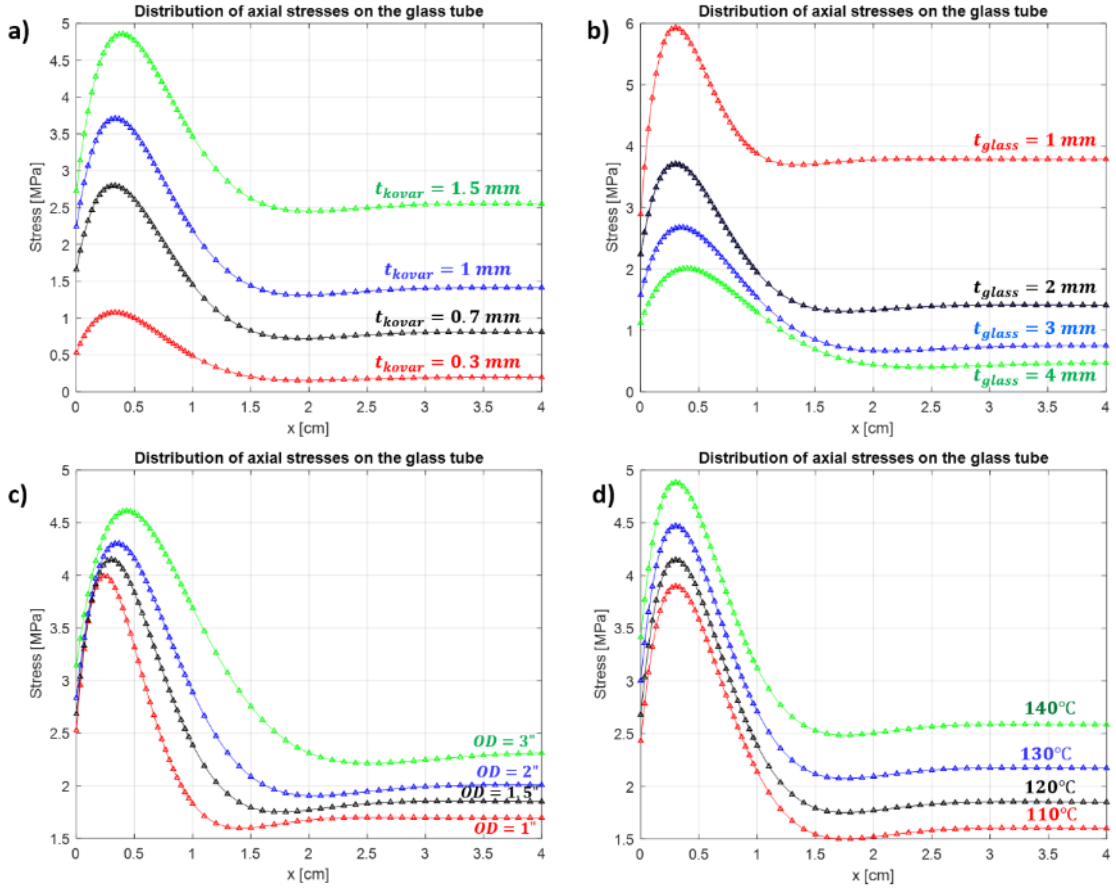

Figure 21: Effects of (a) metal ring (Kovar) thickness (OD=1.5", t_{glass} = 2.5 mm); (b) glass tube thickness (OD=1.5", t_{kovar} = 0.8 mm); (c) outer diameter of the glass tube (t_{glass} = 2 mm, t_{kovar} = 0.8 mm, T=120°C); (d) Operating pressure at sat. temp. (OD=1.5", t_{glass} = 2 mm, t_{kovar} = 0.8 mm).

Positive pressure tests of the Kovar-glass graded seal joint were completed. To test the burst pressure of the joint, a glass tube section with graded seal joints at both ends was first completely filled with water. The pressure of the water fill was gradually increased using a manual hydraulic pump. Both test tube sections were remained intact at pressures up to 133 psia and 151 psia respectively, which is about 4 to 5 times of the operating pressure of the LTS design. Figure 22 shows one of the measured pressure curves.

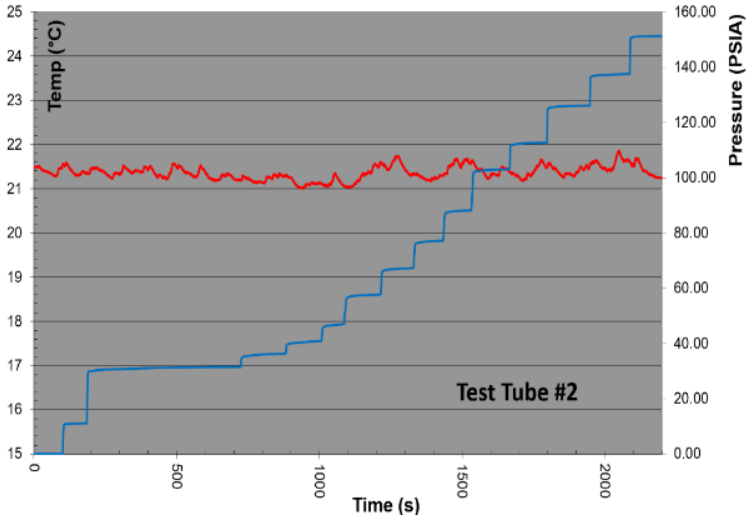

Figure 22: Positive Pressure Test (Blue Curve) for One of the Kovar-Borosilicate Tubes

To observe the burst pressure, the pressure was further increased using a hydraulic pump. Since a manually driven pump was used, it was difficult to ramp the pressure at a constant, gradual rate. One of the tubes failed at about 520~530 psia, and the other failed at about 530~540 psia. These results gave the team confidence to proceed with the graded seal Kovar-Borosilicate joints.

Overall Optical-to-Thermal Efficiency of Solar Receiver System

To examine the net positive impact of the glass receiver with volumetrically-absorbing working fluid, a state-of-the-art (SOTA) receiver was compared against it. A SOTA solar receiver consists of a steel absorber tube through which a liquid heat transfer fluid (HTF) flows. A selective coating is applied to the outer surface of this tube, reducing radiative heat losses, and maximizing absorbed solar energy. An outer glass envelope encapsulates the absorptive tube and allows for a vacuum insulation layer surrounding the receiver. To improve transmittance through the glass envelope, anti-reflective coatings (ARC) are applied to the surfaces of the envelope tube. For the volumetric absorption receiver, the inner steel tube is replaced by a glass tube. Incident solar energy passes through both the inner and outer tubes and is absorbed by the black HTF (dye solution).

Solar receiver performance was modeled using an energy balance based on physical heat transfer models and existing heat transfer correlations. Two receiver tube coatings were considered. The Luz black chrome coating has a solar absorptance of 94%, and emissivity of 0.110 at 100°C and 0.27 at 400°C. The second coating, Luz cermet, has a lower absorptance of 92%, but emissivity is reduced to 0.06 at 100°C and 0.15 at 400°C. While the black chrome coating has higher solar absorptance, the cermet coating has lower radiative losses, which reduces the difference in net solar absorptance between the two. The cermet coating was assumed for the results presented here.

Results of the SOTA solar collector modeling are presented in Figure 23. The percentage of direct normal irradiance (DNI) incident on the trough aperture to the thermal energy leaving in the HTF (Q_{HTF}) is calculated using the following equation:

$$\eta_{th} = \frac{Q_{HTF}}{DNI} = \eta_o \cdot \tau \cdot \alpha_{coating} \cdot R_{sa} \tag{2}$$

Where η_o is the optical efficiency of the trough, τ is the envelope or outer glass transmittance, α is the absorptance, and R_{sa} is the radiation loss efficiency. Based on the aperture of the trough A_{apert} and energy balance equation, we can explicitly express the radiation loss efficiency and rewrite the above equation as:

$$\eta_{th} = \frac{\eta_0 \tau \alpha_{coating} A_{apert} DNI - Q_{loss}}{A_{apert} DNI} = \eta_0 \tau \alpha_{coating} - \frac{\sigma(T_{HS}^4 - T_{env}^4)}{A_{apert} DNI \left[\frac{1}{\varepsilon_{coating}} + \frac{1-\varepsilon_{gt}}{\varepsilon_{gt}}\left(\frac{A_{rec}}{A_i^{env}}\right)\right]} \tag{3}$$

Where T_{HS} is the average surface temperature of the steel tube, T_{env} is the envelop (outer) glass tube temperature, $\varepsilon_{coating}$ is the emissivity of the surface selective coating, ε_{gt} is the emissivity of the glass tube, which is equal to 0.86, A_{rec} is the outer surface area of steel tube (receiver tube), and A_i^{env} is the inner surface area of the envelope tube. The radiative heat loss is the net radiative heat transfer between the outer surface of steel tube and inner surface of the envelope tube (IR opaque). Under steady state conditions, the radiative heat loss is equal to the summation of convective heat transfer (h_{out}) between the ambient air (T_{amb}) and the outer surface of envelope tube (A_o^{env}) and the radiative heat transfer between the outer surface of envelope tube and the sky (T_{sky}). This relation can help us determine the envelop glass tube temperature T_{env}, i.e.,

$$Q_{loss} = \frac{\sigma A_{rec}(T_{HS}^4 - T_{env}^4)}{\frac{1}{\varepsilon_{coating}} + \frac{1-\varepsilon_{gt}}{\varepsilon_{gt}}\left(\frac{A_{rec}}{A_i^{env}}\right)} = A_o^{env} h_{out}(T_{env} - T_{amb}) + A_o^{env}\sigma\varepsilon_{gt}(T_{env}^4 - T_{sky}^4) \tag{4}$$

Where the sky temperature is $T_{sky} = 0.0553 T_{amb}^{1.5}$, and the natural convection heat transfer correlation between a horizontal tube (diameter D) and the air under no wind condition is:

$$\overline{Nu}_D = \frac{h_{out} D}{k(\bar{T})} = \left\{ 0.60 + 0.387 \left[\frac{Ra_D(\bar{T})}{\left[1 + \left(\frac{0.559}{Pr(\bar{T})}\right)^{\frac{9}{16}}\right]^{\frac{16}{9}}} \right]^{\frac{1}{6}} \right\}^2 \tag{5}$$

Where $\bar{T}$ is the average temperature of ambient air and envelope glass tube, $\bar{T} = \frac{T_{env} + T_{amb}}{2}$, which needs to be determined iteratively, Pr is the Prandtl number of the air, and the Rayleigh number is defined as $Ra_D(\bar{T}) = \frac{g\beta\Delta T D^3}{\nu(\bar{T})\alpha(\bar{T})}$, both of which should be calculated using the average temperature. Losses throughout the trough and receiver assembly are presented in Figure 23.

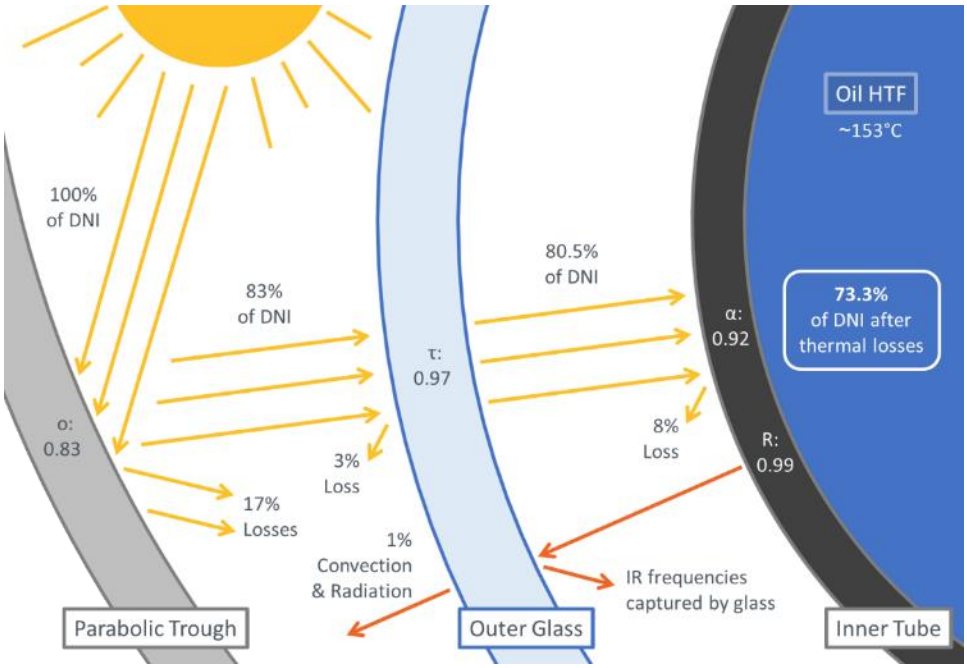

Figure 23: Illustration of Thermal Losses and Absorptance of SOTA Solar Collector

Net solar absorptance for ACT's volumetric absorption solar collector was also modeled, with results presented in Figure 24. For this configuration, the inner steel tube is replaced by a second glass tube, and solar energy is directly absorbed by the dark HTF (a dye solution). The equation for the DNI thermal percentage leaving in the HTF is similar to that of the SOTA collector, with the primary difference being that the light must pass through two glass tubes, doubling the transmittance losses. In addition, the radiation loss efficiency R_{va} (va = volumetric absorbing) will have a slightly different form:

$$\eta_{th} = \frac{Q_{HTF}}{DNI} = \eta_o \cdot \tau^2 \cdot \alpha_{soln} \cdot R_{va} \tag{6}$$

Absorptance, α_{soln}, is greater for the volumetric absorption case, with ~99.5% of incident light absorbed directly by the dye solution. Thermal losses are increased for this case, as the low emissivity coating used on the SOTA receiver cannot be used on the transparent glass tube of the volumetrically absorbing receiver. The emissivity of the glass tube is assumed to be 0.86. Again, we can explicitly express the radiation loss efficiency and rewrite the above equation as (slightly different from the surface absorbing case):

$$\eta_{th} = \eta_o \tau^2 \alpha_{soln} - \frac{\sigma(T_H^4 - T_{env}^4)}{A_{apert} DNI \left[\frac{1}{\varepsilon_{gt}} + \frac{1-\varepsilon_{gt}}{\varepsilon_{gt}}\left(\frac{A_{rec}}{A_i^{env}}\right)\right]} \tag{7}$$

The envelope glass tube temperature can be determined using the method described before. Figure 23 and Figure 24 show that the volumetric absorption solar receiver has a overall DNI to Q_{HTF} efficiency of 75.2% vs. 73.3% for the SOTA receiver; a 1.9% increase.

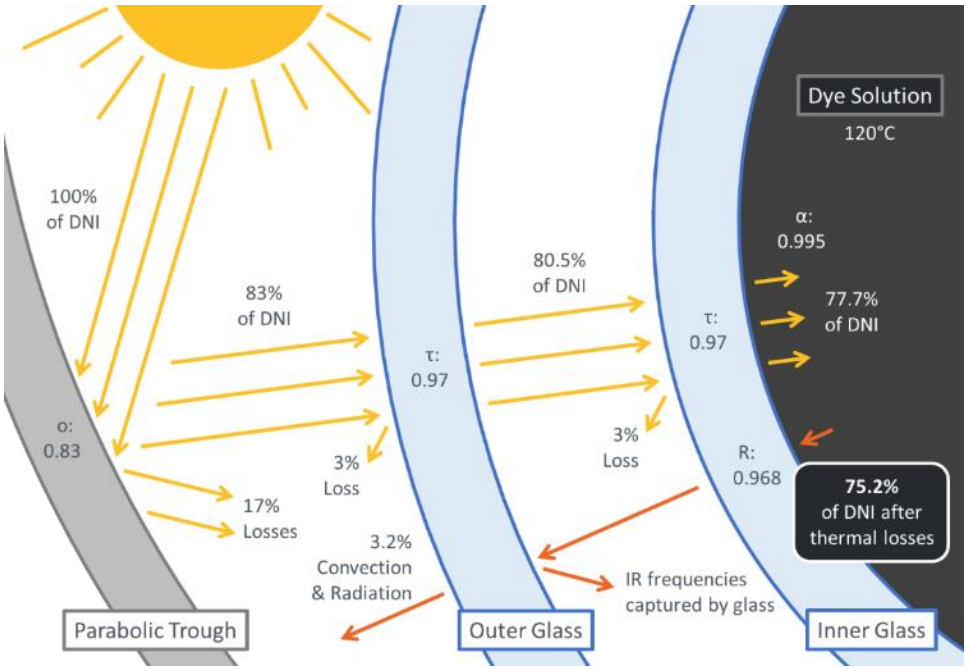

Figure 24: Illustration of Thermal Losses and Absorptance of Volumetric Absorption Collector

Task 2.2: *Accelerated Corrosion Tests of Nanofluids on Tube Materials*

This purpose of Task 2.2 is to investigage the compatibility (or corrosion rate) of the loop thermosyphon materials when in contact with the working fluid. A successful corrosion rate is one that allows the system to operate nominally for 25 years.

Corrosion (Compatibility) Tests in Water and Dye Solution

The loop thermosyphon is primarily made of borosilicate glass and copper tubing. Copper, when used as a heat pipe or thermosyphon envelope material, is known to be compatible with water. However, due to the CTE mismatch between copper and borosilicate glass, a Kovar-glass joint is needed as described previously.

This problem can be solved by forming the Kovar-borosilicate glass joint first, then forming a Kovar-copper joint. Kovar is Fe-Ni-Co alloy with trace amount of C, Si and Mn. Nickel alloy is well-known to have outstanding corrosion resistance. Therefore, one may think a Kovar-copper joint is compatible with water-based solutions. We designed a high-temperature corrosion test setup to investigate the compatibility of Kovar-copper with water (Figure 25).

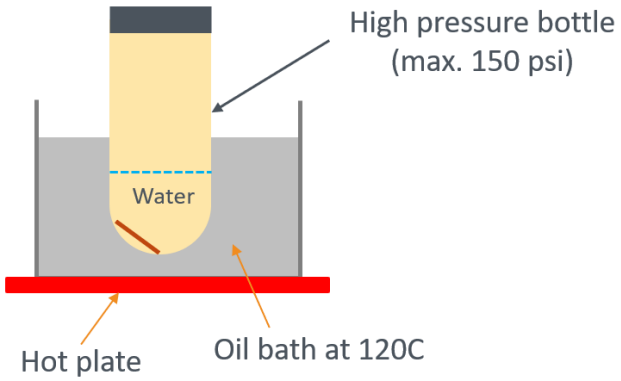

Figure 25: High Temperature Corrosion Test Setup.

During the test the sample temperature is controlled by the oil bath which is heated by a hot plate. The sample immersed in the hot water was a thin Kovar plate 38.6 mm long and 19.5 mm wide. Half of the sample surface was electroplated with a thin copper layer with a thickness between 50 and 75 μm. The sample was maintained at 120°C for 8 hours a day for 34 days. The test results were worse than our initial expectation. The surface showed obvious corrosion, as indicated by Figure 26. This was determined to be due to electrochemical redox reactions between the iron component in the Kovar, the copper, the water and dissolved oxygen in the water.

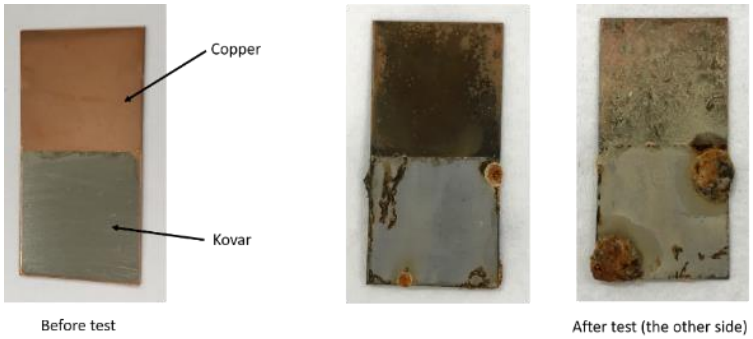

Figure 26: Kovar-Copper Samples Before and After Corrosion Testing. Obvious Corrosion on the Surface was Observed.

To avoid the simultaneous contact of iron and copper with water, another batch of Kovar samples were fabricated, where their entire surface was electroplated with copper. The thickness of the copper layer was between 50 and 75 μm. The same test method was followed, and the samples were heated to different temperatures (120°C and 130°C, completed; 150°C, undergoing). Each sample was heated for 8 hours a day for about one month. The surface of the corroded samples became complete black, due to oxidation of the copper into copper oxide (CuO). The copper oxide layer serves as a protective layer preventing the electrochemical reaction of iron and copper with water. This result indicated that complete, electroplated copper layer prevents the corrosion of Kovar in high temperature water. These Kovar samples before and after testing are presented in Figure 27.

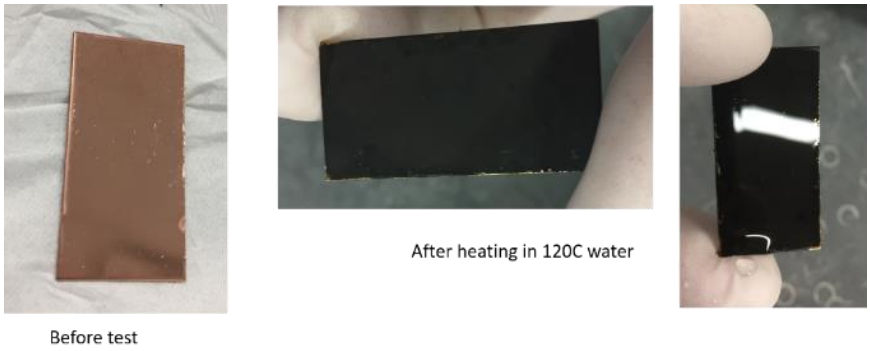

Figure 27: Kovar Sample (Entire Surface Electroplated with Copper) Appearance Before and After Corrosion Test.

The copper oxide layer thickness after each corrosion test was quantified by measuring the sample size and weight before and after the immersion corrosion test and using the density of copper oxide. In all cases, the change of sample weight is very small, from about 0.45 mg for a test at 120°C to 0.8 mg for a test at 150°C. The CuO layer thickness increases from about 230 nm to about 440 nm (see Figure 28). For an electroplated copper layer with a thickness of 75 µm, under conservative consideration, the loop thermosyphon could be operated at 120°C for at least 26 years, satisfying the 25-year lifespan target.

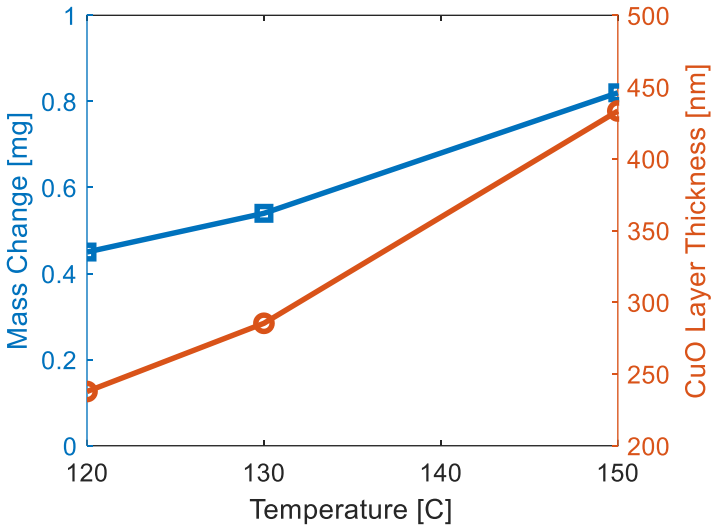

Figure 28: The Change of Sample Weight and CuO Layer Thickness as a Function of Corrosion Test Temperature.

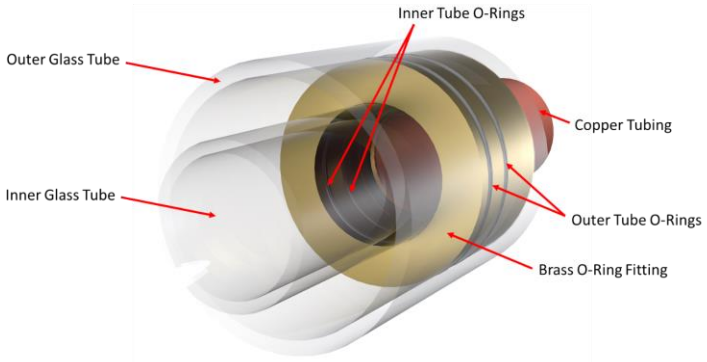

Figure 29: Illustration of the Double-Wall O-Ring Glass-Metal Joint

Task 2.4: *Thermal Cycling Testing for Loop Thermosyphon Materials*

Task 3.2: *Summary of Loop Thermosyphon Life Tests*

The key metric of these tasks is the reliability of the glass-metal joint under thermal cycling. We have demonstrated that the Kovar-glass joint can achieve excellent mechanical strength by choosing suitable glass thickness, metal thickness, and tube diameter, but it was unclear whether the joint could survive thousands of temperature & pressure cycles. These task were completed to ensure that the metal-glass joints could survive after 9,200 thermal cyclings (25 years of day/night heating and cooling cycles).

Design of the Glass/Metal Joint

Two methods for joining the glass receiver tubes to the metal tubing of the LTS were evaluated; the Kovar-glass graded-seal joint previously shown and a static O-ring joint. The O-ring sealing method was developed by ACT on a parallel program and utilized in this program as an alternative to the graded-seal joint. The O-ring joint consists of dual O-rings placed around the glass tube and which fit grooves in a brass fitting surrounding the tube. Although brass and borosilicate glass are not CTE-matched, the O-rings allow the materials to expand and contract independently without breakage or loss of seal.

Unlike a graded seal joint, the O-ring design does not require an expansion/contraction bellows at the end/s of the glass tube. Figure 29 presents the O-ring glass-metal joint.

An evacuated annulus insulates an ideal glass receiver. The O-ring seal design facilitates an evacuated annulus between the inner tube and an outer glass tube, sealed with O-rings fitted into the outer surface of the brass fittings. Figure 29 presents the configuration of these concentric O-ring-sealed glass tubes.

Thermal Cycling of the Glass/Metal Joints

Two thermosyphons were constructed to test the long-term fatigue performance of the Kovar-glass and O-ring joints. Figure 30 presents the two life test thermosyphons. The left thermosyphon is for testing the double-wall O-ring glass joint, with the right thermosyphon fitted with the graded seal Kovar-glass tube section. Dissimilar metal corrosion and off-gassing were prevented by fabricating the O-ring joint thermosyphon from copper with brass O-ring fittings and the Kovar-glass joint thermosyphon from stainless steel.

Each thermosyphon is heated below the glass test section and is cooled above the glass section. Four (4) 300W band heaters heat the O-ring joint thermosyphon, while a single 1,000W cartridge heater heats the Kovar-glass joint thermosyphon. Chilled aluminum blocks clamped around the top of the thermosyphons condense the water working fluid, which falls back to the evaporator regions at the bottom of the systems. 500W chillers supply chilled water to cool the aluminum condenser blocks. A pressure transducer verifies the saturation pressure of each thermosyphon, and thermocouples are placed below, within, and above the glass test sections. A programable logic controller (PLC) handles data collection and controls the thermal cycling of the thermosyphons. Figure 31 presents close-up detail of the two glass tube sections.

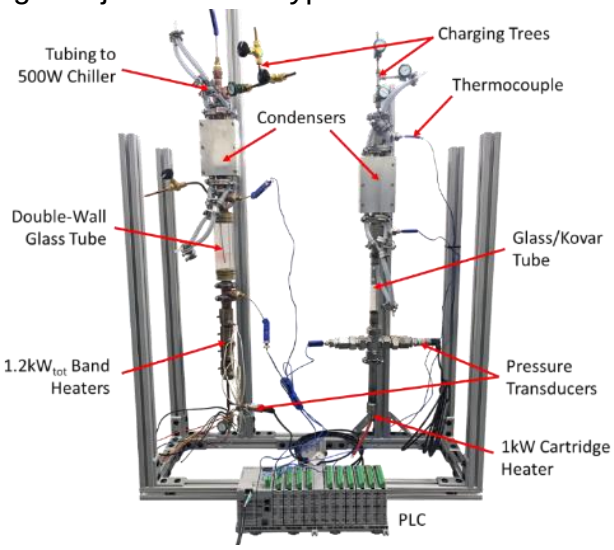

Figure 30: Glass/Metal Joint Thermosyphon Systems for Thermal Cycling Testing.

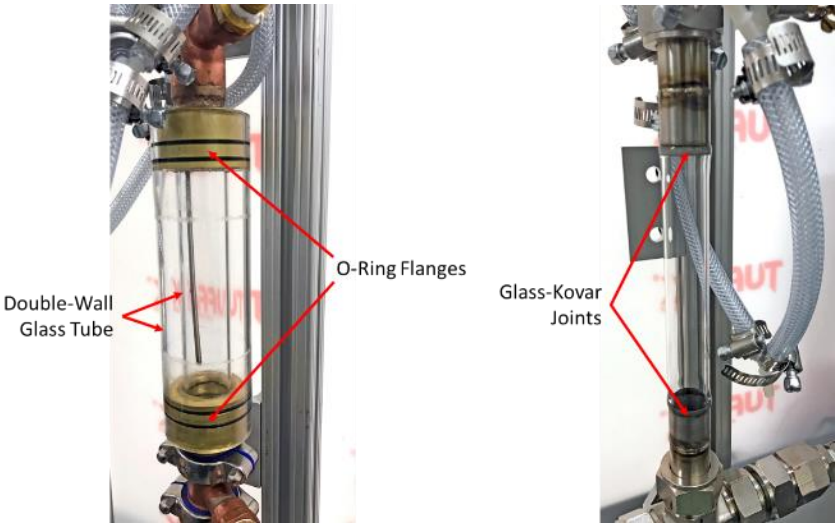

Figure 31: Glass/Metal Joints Being Thermal Cycled (left) the Double-Wall O-Ring Glass Joint and (right) the Kovar-Glass Graded Seal Glass Joint

Thermal Cycling Test Results

The team continuously cycled the two glass-metal joint test thermosyphons between September 2021 and March 2022. A programmable logic controller (PLC) automatically controlled the thermosyphons' heating and cooling systems to cycle saturation temperature between ~70 and 120°C. This saturation temperature swing corresponds to an internal pressure variation between ~5 and 27 psia for the water working fluid. The full-scale loop thermosyphon solar collector operates at comparable saturation temperatures and pressures.

Figure 32 presents the operating temperatures and pressures for the O-ring joint test thermosyphon during an hour of testing. All three thermosyphon temperatures rise and fall together as expected due to the highly isothermal nature of small-scale thermosyphons. The condenser coolant flow rate is reduced during heating while evaporator power is maximized. The opposite scenario occurs during cooling, with the coolant flow rate maximized and heating reduced. Minimal heat input is required during cooling to sustain the operation of the thermosyphon, allowing it to transfer thermal energy up the thermosyphon to the coolant. Approximately 5 heating and cooling cycles occur per hour, allowing the system to complete the targeted 9,200 cycles over 77 days of continuous operation.

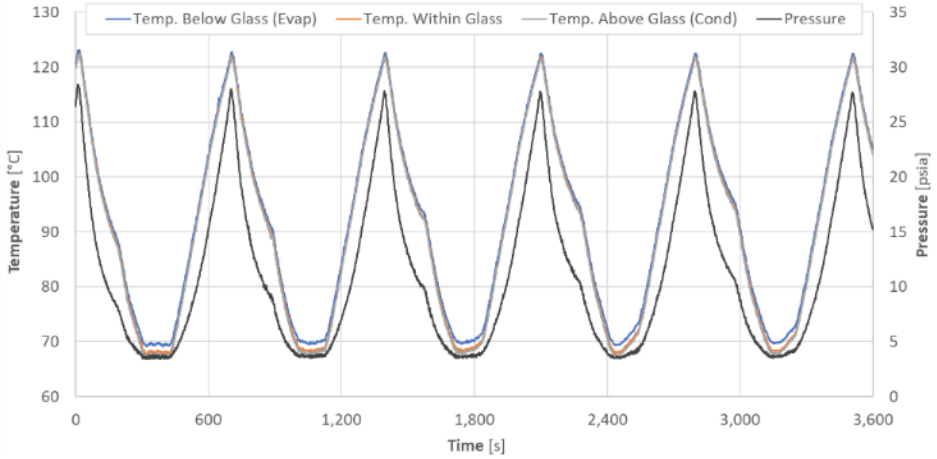

Figure 32: Temperature and Pressure Measurements Within the O-ring Glass-Metal Joint Test Thermosyphon During an Hour of Cycling. Approximately 5 heating and cooling cycles were completed per hour between saturation temperatures of ~70 and 120°C. Internal pressure varies between ~4 and 27 psia.

The Kovar-glass graded seal joint failed at the joint after approximately 5,000 cycles or 13.7 simulated years. Figure 33 presents the broken glass/Kovar joint, which failed at the lower Kovar-glass joint. The O-ring glass-metal joint successfully completed the 9,200-cycle, 25-year life test and is recommended as a manufacturing method for fully-glass solar receivers. Despite this success, the fully-glass receiver proved problematic when scaled and tested at even moderate lengths (~40"), as discussed below.

Figure 33: Broken Kovar-Glass Joint After ~5,000 Thermal/Pressure Cycles

Conclusions

Glass-to-metal joints for high-temperature solar receivers are challenging due to CTE mismatches between commonly used metals and glasses. A CTE-matched borosilicate Kovar-glass joint was thermal cycle tested alongside an O-ring sealed glass-metal joint. The Kovar-glass graded seal joint failed after approximately 5,000 heating/cooling cycles, while the O-ring sealed joint completed the entire 9,200 cycle test program. The increased durability of the O-ring joint is likely due to the joint's mechanical flexibility. The O-ring allows the glass and metal to move and slide independently of one another as they expand and contract. For this reason, an O-ring-style glass/metal joint is recommended for fully-glass concentrated solar evaporator designs.

Project Results and Discussion – LTS Modeling & Development

Tasks 1.1, 1.6, 2.3, and 2.5, comprise the loop thermosyphon modeling, design, fabrication, and testing work completed throughout the three-year program. The following section summarizes the work and key findings of these Tasks.

Task 1.1: *Develop a rigorous system model to determine the cost and performance of the proposed loop thermosyphon system.*

During Task 1.1, an Excel-based 1D numerical loop thermosyphon model was developed to predict LTS operational performance at different system configurations and provide information for the experimental systems, such as fluid charge. The numerical LTS model is based on the pressure and energy balance around the loop.

One feature of an LTS is that it is possible for a two-phase working fluid to flow against gravity from evaporator to condenser. In other words, liquid can be carried along with the vapor leaving the evaporator. This feature is particularly important in the present application as a significant portion of the flow must be liquid at the exit of the evaporator to ensure complete volumetric solar absorption. The motive force required to lift liquid to the condenser is provided by the gravitational head of the liquid condensate beneath the condenser ($\Delta P_{g\,liq}$). Resisting this positive head is the gravitational head of the two-phase flow ($\Delta P_{g\,2\phi}$) and frictional pressure drops in the liquid ($\Delta P_{f\,liq}$) and two-phase lines ($\Delta P_{f\,2\phi}$). In addition, the sum of acceleration ($\Sigma\Delta P_a$) and minor pressure losses ($\Sigma\Delta P_m$) also resist the fluid flow and must be accounted for. During steady-state loop thermosyphon operation, these six pressure components must be in equilibrium:

$$\Delta P_{g\,liq} + \Delta P_{g\,2\phi} + \Delta P_{f\,liq} + \Delta P_{f\,2\phi} + \Sigma\Delta P_a + \Sigma\Delta P_m = 0 \quad (8)$$

Equation (8) forms the basis for modeling of LTS performance and can be applied a wide range of LTS geometries, working fluids, and input powers. By predicting gravitational, frictional and acceleration pressure drops around an LTS, the model can predict changes in the saturation temperature, which directly influence the working fluid thermal resistance between the evaporator and condenser.

Beginning from the pressure balance principle of Equation (8), a numeric mass and energy balance model of the solar-driven LTS was created. Within the code, the LTS is initially divided into discrete sections for sequential analysis. The following five types of sections were defined within the model: evaporator sections, condenser sections, tube sections, elbows and T's. An example of this loop thermosyphon discretization is illustrated in alongside critical dimensions and fluid operating parameters defined and calculated by the model.

Model execution begins by specifying a saturation temperature, operating temperature (if superheated or subcooled), and fluid quality, which define the enthalpy and pressure at the inlet or outlet of the starting section. Beginning from this point of the loop, a heat and mass balance is serially performed alongside a pressure drop analysis for each section of the loop. The fluid flow is fully defined by only two "base" parameters; enthalpy and pressure. The model iterates on these two parameters with temperature, density,

viscosity, and surface tension derived from the pressure and enthalpy values in each section.

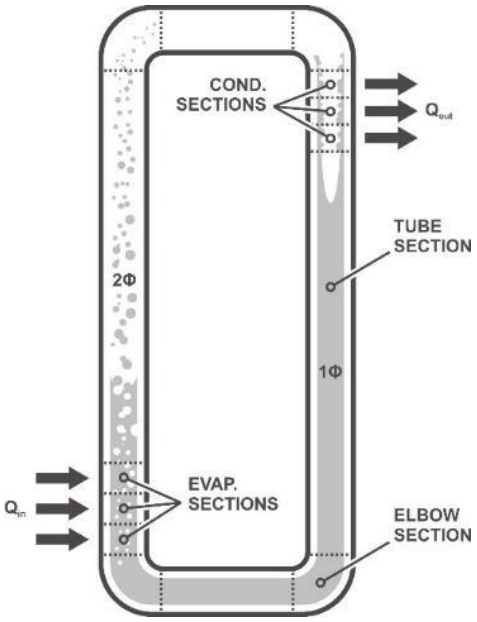

DIMENSIONS
- ID: Inner Diameter
- OD: Outer Diameter
- L: Length
- A: Cross-sectional Area
- θ: Tube Inclination (relative to positive x-axis)
- r: Elbow Radius

BASE FLUID PARAMETERS
- h: Enthalpy
- P: Pressure

DERIVATIVE FLUID PARAMETERS
- T: Temperature
- ρ: Density
- μ: Viscosity
- σ: Surface Tension

CALCULATED FLUID PARAMETERS
- ΔP_f: Frictional Pressure Drop
- ΔP_g: Gravitational Head
- ΔP_a: Acceleration Pressure Drop
- ΔP_m: Minor Pressure Losses
- α: Void Fraction
- h_c Convective Heat Transfer Coefficient

Figure 34: Illustration of LTS Model Discretization and Important Calculation Dimensions and Parameters

Frictional Pressure Drop Calculations

As suggested by Equation (8), accurate calculation of the loop pressure drops is essential in predicting the performance of the LTS. In sections with single-phase liquid or vapor (i.e. in the downcomer), frictional pressure drop is calculated using the standard Darcy frictional factor equation for tubular flow. However, in the evaporator, two-phase riser, and condenser, empirically derived, two-phase pressure drop correlations are most applicable.

Lockhart and Martinelli (L-M) [5] proposed that the two-phase frictional pressure drop per unit length $(dP_f/dz)^{2\phi}$ be estimated by multiplying the single-phase frictional pressure drop for the liquid phase $(dP_f/dz)_{liq}$ by a two-phase frictional pressure drop multiplier ($\phi_{liq}^{2\phi}$):

$$\left(\frac{dP_f}{dz}\right)^{2\phi} = \phi_{liq}^{2\phi}\left(\frac{dP_f}{dz}\right)_{liq} \tag{9}$$

The two-phase frictional pressure drop multiplier is a function of the Lockhart and Martinelli parameter (*XLM*) and a *C* value (Table 3):

$$\phi_{liq}^{2\phi} = 1 + \frac{C}{XLM} + \frac{1}{XLM^2} \tag{10}$$

Table 3: C Values for the L-M Correlation [6]

		Vapor	
		Lam.	Turb.
Liquid	Lam.	5	10
	Turb.	12	20

The XLM parameter is defined as the ratio of the pressure drops if the liquid and vapor flow rates are individually filling the entire flow cross section:

$$XLM = \sqrt{\frac{\left(\frac{dP_f}{dz}\right)_{liq}}{\left(\frac{dP_f}{dz}\right)_{vap}}} \tag{11}$$

The single-phase pressure drops are calculated using the single-phase Darcy pressure drop equation for liquid or vapor flow:

$$\left(\frac{dP_f}{dz}\right)_{liq} = \frac{2f_{liq}G^2(1-x)^2}{d_h\rho_{liq}} \qquad \left(\frac{dP_f}{dz}\right)_{liq} = \frac{2f_{vap}G^2x^2}{d_h\rho_{vap}} \tag{12) \& (13}$$

Where, G is the mass velocity ($\dot{m}/A$) of the entire flow, x is the quality, and d_h is the hydraulic diameter. A transition Reynolds number of 2,300 was assumed in calculating the laminar and turbulent friction factors:

$$f_{lam} = \frac{64}{Re_{liq/vap}} \qquad f_{turb} = \frac{0.316}{Re_{liq/vap}^{0.25}} \tag{14) \& (15}$$

Finally, Reynolds numbers for the liquid and vapor portion of the flow are calculated using the mass velocity and quality:

$$Re_{liq} = \frac{\rho_{liq}G(1-x)d_h}{\mu_{liq}} \qquad Re_{vap} = \frac{\rho_{vap}Gxd_h}{\mu_{vap}} \tag{16) \& (17}$$

Equations (9) through (17) are used by the model to predict the two-phase frictional pressure drop. The C values presented by Chisholm in Table 1 only apply to horizontal, tubular two-phase flow. Yadav expanded on this work, by studying fully turbulent, vertical upward and downward two-phase flows, with appropriate C values for both cases proposed [7]. A linear curve fit between Chisholm's horizontal C values (0°) and Yadav's values for ±90° was used to create an equation for the turbulent liquid-turbulent vapor (*tl-tv*) C value at any tube inclination (θ):

$$For\ \theta\ between\ 0\ and\ 90°: C_{tl-tv} = 0.2\bar{2}\theta + 20 \tag{18}$$

$$For\ \theta\ between\ 270\ and\ 360°: C_{tl-tv} = 0.1\bar{1}\theta + 20 \tag{19}$$

Where, θ is in degrees. In addition to the L-M correlation, the Friedel two-phase frictional pressure drop correlation was also implemented in the model. The correlation used is user-selectable in the model user interface. Complete details of the Friedel correlation are outlined by Filip et al. [8].

An accurate prediction of void fraction (α) throughout the two-phase flow is critical to accurate estimations of fluid charge. Several user-selectable methods for estimating void fraction in the two-phase region were implemented in the model. These include Lockhart and Martinelli's method based on the previously defined XLM parameter:

$$\alpha = (1 + XLM^{0.8})^{-0.378} \tag{20}$$

Heat Transfer Calculations

To estimate thermal losses from the thermosyphon and better predict heat transfer within the evaporator and condenser, heat transfer coefficients were calculated throughout the single and two-phase sections of the loop. Within the evaporator, a correlation developed by Kandlikar was used to predict the saturated flow boiling heat transfer coefficient ($h_{2\phi b}$). This boiling heat transfer coefficient is a function of the convective (*Co*) and boiling (*Bo*) numbers, the single-phase liquid heat transfer coefficient (h_{liq}), a fluid parameters (F_{fl}), the liquid only Froude number (Fr_{LO}), and five constants (C_1-C_5):

$$h_{2\phi b} = C_1 Co^{C_2} (25 Fr_{LO})^{C_5} h_{liq} + C_3 Bo^{C_4} h_{liq} F_{fl} \tag{21}$$

The calculation of these values is beyond the scope of this paper, but complete details are presented by Kandlikar [9]. In the non-boiling, two-phase region, Chen's modified form of the Dittus-Boelter equation is used to calculate the two-phase heat transfer coefficient ($h_{2\phi}$) [10]:

$$h_{2\phi} = 0.023 (Re_m)^{0.8} \left(Pr_{liq}\right)^{0.4} \frac{k_{liq}}{d_h} \tag{22}$$

Where, Rem is the homogeneous mixture Reynolds number. For loop thermosyphon sections in the condenser, the Shah correlation was chosen to approximate the condensing heat transfer coefficient. As presented by Papini et al. [11], the local, two-phase condensing heat transfer coefficient ($h_{2\phi c}$) can be computed by another Dittus-Boelter-based correlation:

$$h_{2\phi c} = h_{liq} \left[(1-x)^{0.8} + \frac{3.8 x^{0.76} (1-x)^{0.04}}{Pr_{liq}^{0.38}} \right] \tag{23}$$

Shah's correlation, presented in Equation (23), is applicable to vertical, inclined, and horizontal condensers. After solving for the heat transfer coefficient around the loop thermosyphon, heat loss from each section is estimated using a sum of thermal resistance method through the tube wall and an insulation layer surrounding the tube.

Excel Model Verification

Verification of the Excel model was conducted through a comparison with previous modeling results presented by Hartenstine et al. [12]. The Model's autogenerated illustration of this LTS with dimensions is presented on the left-hand side of Figure 35, Hartenstein et al. used the Lockhart-Martinelli correlation to calculate the mass flow rate, vapor quality, and vapor fraction for this LTS across a range of thermal powers between 0.25 and 10 kW_{th}. Similar cases were run for this LTS using the Excel model with the flow rate, vapor quality, and vapor fraction results plotted alongside those presented by Hartenstein et al. in Figure 35

As seen, Hartenstine et al.'s modeling results agree very closely with those generated by the Excel model across the entire input power range. This agreement helps to verify that the Excel VBA model is consistent with previously published results.

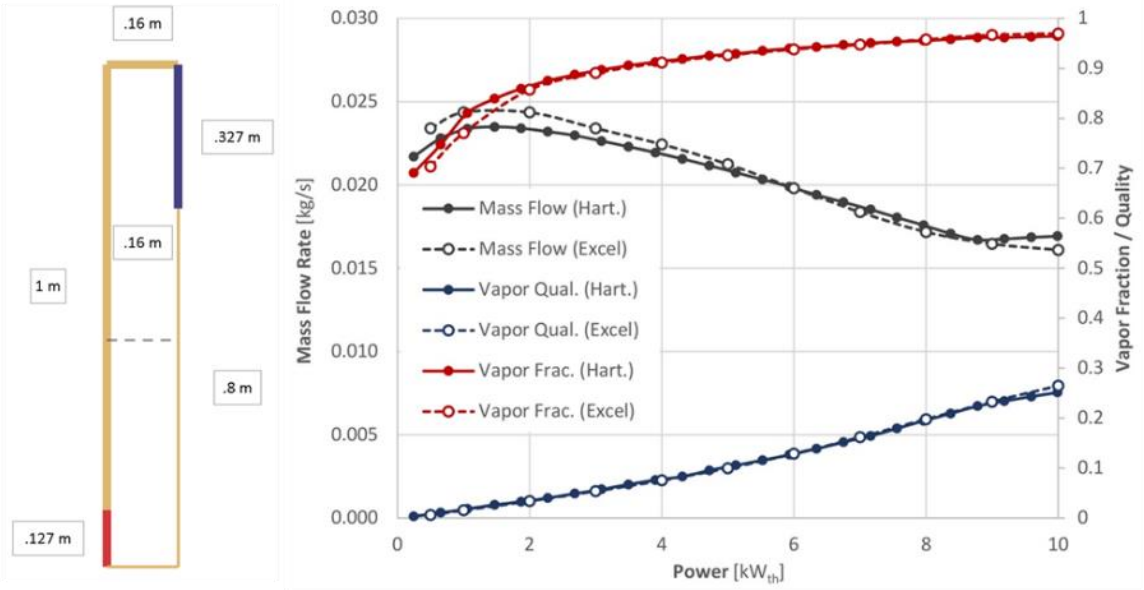

Figure 35: LTS as Presented by Hartenstine et al. & Modeling Result Comparison

Task 1.6: *Loop Thermosyphon Performance Evaluation with Inclined Evaporator.*

Using the Excel-based loop thermosyphon model, a sub-scale (500W) loop thermosyphon prototype system was designed at three evaporator inclination angles (0, 5, and 30°). This sub-scale system will be used for model validation and serve as the initial test bed for the loop thermosyphon system. The loop thermosyphon was designed around the following criteria:

Working fluid: water
material: copper
Evaporator power: 100-500W
Condenser length: 9.375 in
Condensing temperature: 100-160°C
Maximum working fluid velocity: 1 m/s
Evaporator length: 20 in
Tube

Using the model, it was found that a copper tube with an inside diameter (ID) of 0.62" resulted in a maximum two-phase flow velocity of approximately 1 m/s across the range of operating conditions. This tubing ID corresponds to an outer diameter (OD) of 0.75" and can be easily bent to a 3 in radius elbow.

The physical lab-scale system was designed in Solidworks using commonly available tubing and fittings (Figure 36). The loop thermosyphon was designed as a single system, which could be operated at 0, 5 and 30°C evaporator inclinations through changing out two tube sections. To reduce system complexity, the tube diameter used for the two-phase region was maintained around the entire loop. Compression-type tube fittings were used throughout the system provide ports for temperature and pressure measurements

as well as to join adjacent tube sections. Care was taken to use only brass or bronze fittings to reduce the potential for galvanic corrosion and non-condensable gas generation. A 6-inch, pressure-rated sight tube was added in the vertical, two-phase region of the system to allow for flow visualization. Both the evaporator and condenser were constructed machined aluminum blocks, which clamped around the working fluid tube. Cartridge heaters placed between the aluminum blocks heat the evaporator, while coolant lines run through the condenser aluminum blocks cool the system. Resistance temperature detectors (RTDs) were added for temperature measurement of both the working fluid and coolant across the condenser. Working fluid pressure is measured at the condenser exit via an absolute pressure transducer. Finally, the working fluid flow rate is monitored by an electromagnetic flowmeter located in the condensate line. The system was fully insulated to prevent thermal losses to the environment and a 125-psi relief valve was added to prevent over pressurization of the loop.

The lab-scale LTS prototype was tested at evaporator inclinators of 0 and 30° relative to the horizontal. The 0° inclination is preferential as it allows for longer solar collectors without the need for inclination of the concentrator (parabolic dish, etc.). A summary of the mass flow rate data for the 0 and 30° LTS tests is presented in Figure 37. Fluid charges of 650, 750, and 850mL were tested at saturation temperatures of 110, 120, and 130°C. Power input to the evaporator was varied between 500 and 1,000W.

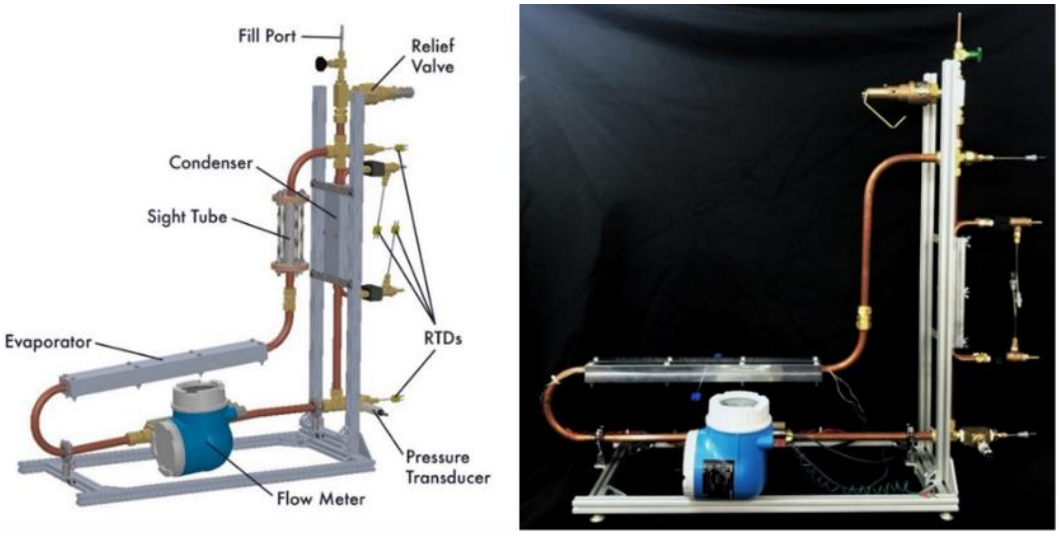

Figure 36: (left) Solidworks Model of 5° Lab-Scale LTS Prototype (right) Completed 0° Sub-Scale Prototype

The LTS was found capable of transferring thermal energy from the evaporator to condenser under all charge, temperature, and power conditions. Higher mass flow rates were found to occur at lower two-phase void fractions (aka. greater two-phase liquid flow from evaporator to condenser). Charge has the greatest impact on flow rate as increasing charge directly increases the liquid head providing the motive force to the working fluid.

For the 0° tests, a clear correlation between power and mass flow rate was not observed. However, for the 30° tests, increasing power consistently led to increases in flow rate.

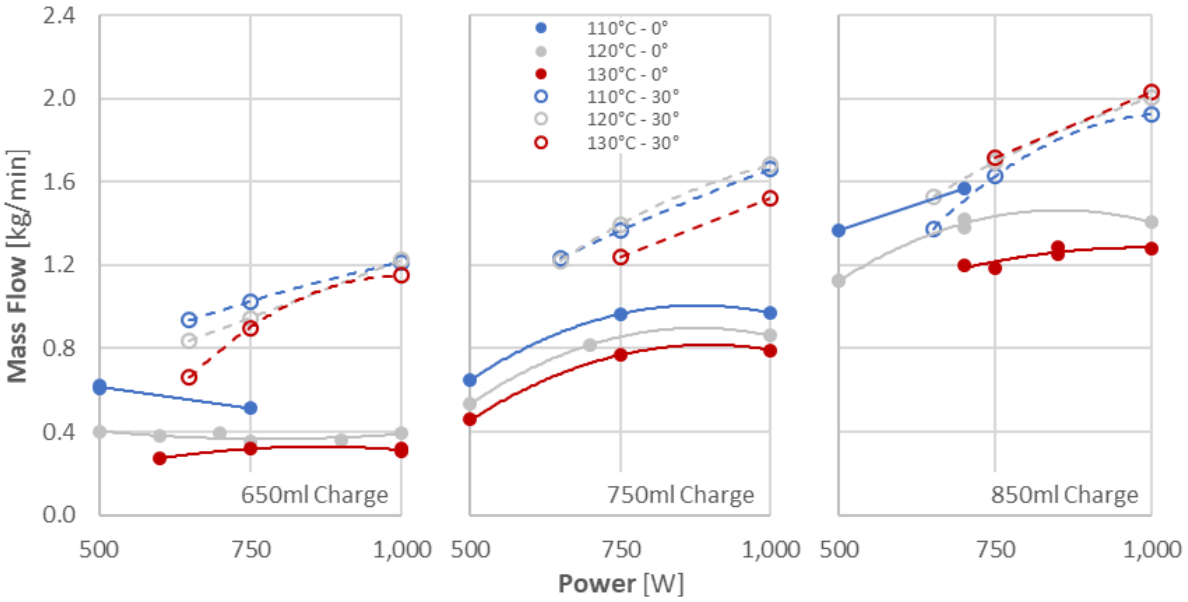

Figure 37: LTS Mass Flow Data for 0 and 30° Evaporator Inclinations

Figure 38 compares the lab-scale LTS modeling results from the Task 1.1 against experimental results. Both the model and experimental results show similar increasing trends in mass flow rate as charge increases (Figure 38, left). The right-hand side of Figure 38 illustrates that while there are considerable difference between the model and experiment at lower charges, as charge increases, the results converge and differ by only 10-15% at the highest charges.

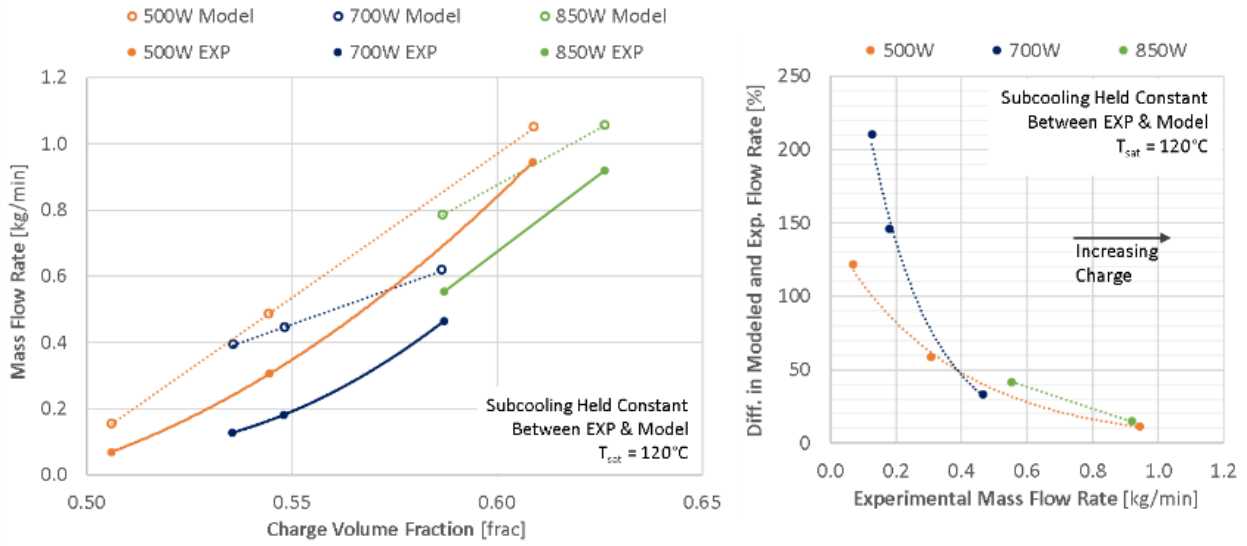

Figure 38: (left) Exp. and Modeled Flow Rate vs. Charge, and (right) Diff. Between Model and Exp. Flow

Task 2.3: *Design, Construct, and Test a Sub-Scale Prototype of the Complete Loop Thermosyphon Solar Collector. (Part 1: Sub-Scale LTS)*

A 3kW, sub-scale loop thermosyphon was designed to fill the gap between the 1kW prototype tested during BP1 and the full-scale 4.3kW system constructed during BP3. This sub-scale LTS design was based around a 1m long, 25mm ID evaporator with a flat plate condenser/boiler. The physical design of the prototype system is presented in Figure 39, with key design parameters listed in Table 4.

A 25 mm ID copper riser was used, with a liquid return line of 19 mm ID. A 50 mm ID accumulator was added directly beneath the condenser to serve as a fluid reservoir and to dampen flow oscillations within the loop. Five resistance temperature detectors (RTDs) are located at key points around the loop for fluid temperature measurements, with two RTDs in the coolant loop for conducting calorimetry on the condenser. An absolute pressure transducer at the condenser inlet provides the two-phase saturation pressure in the riser. Two differential pressure transducers measure pressure differences between the evaporator and condenser inlets, and the condenser inlet and the bottom of the downcomer. An electromagnetic flow meter in the liquid return line provides fluid flow rate measurements.

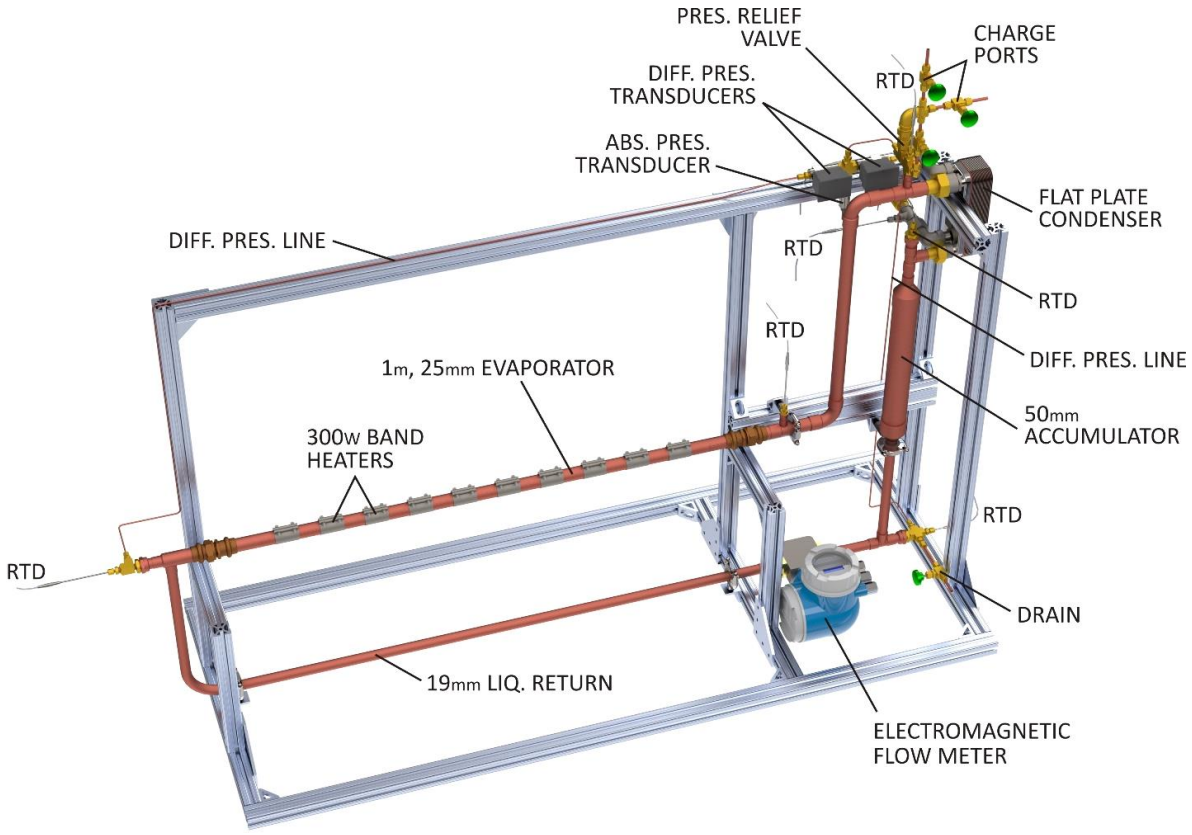

Figure 39: Sub-Scale LTS Physical Design

Table 4: Sub-Scale System Design Parameters

Max Power	[kW]	3
Heat Source		10 Band Heaters
Receiver Length	[m]	1.0
Receiver ID	[mm]	25
Condenser Type		Flat Plate HTX
Condenser Height	[m]	0.5
Coolant		Chilled Water
Accumulator Diameter	[mm]	50
Condensate Return ID	[mm]	19
Temperature Measurement		5 Fluid, 2 Coolant RTDs
Pressure Measurement		1 abs., 2 diff. Pres. Trans.
Flow Rate Measurement		Electromagnetic Flow Meter

Before fabrication began, the sub-scale LTS, was modeled using the one-dimensional pressure-drop and heat transfer LTS model. The design model was run across a range of evaporator powers and fluid charges. The model is capable of iterating on flow rate to achieve a specified fluid charge. This is useful for predicting the performance of the system at specified operating charges. To accomplish an accurate charge analysis, the model must accurately predict the total volume of the system inclusive of all dead-end junctions required by the RTD and pressure transducer connections. The model was modified to allow for these dead-end junctions to be easily created such that the modeled system volume accurately approximates that of the laboratory system. A visual representation of the as-modeled LTS was generated by the model and is presented in Figure 40.

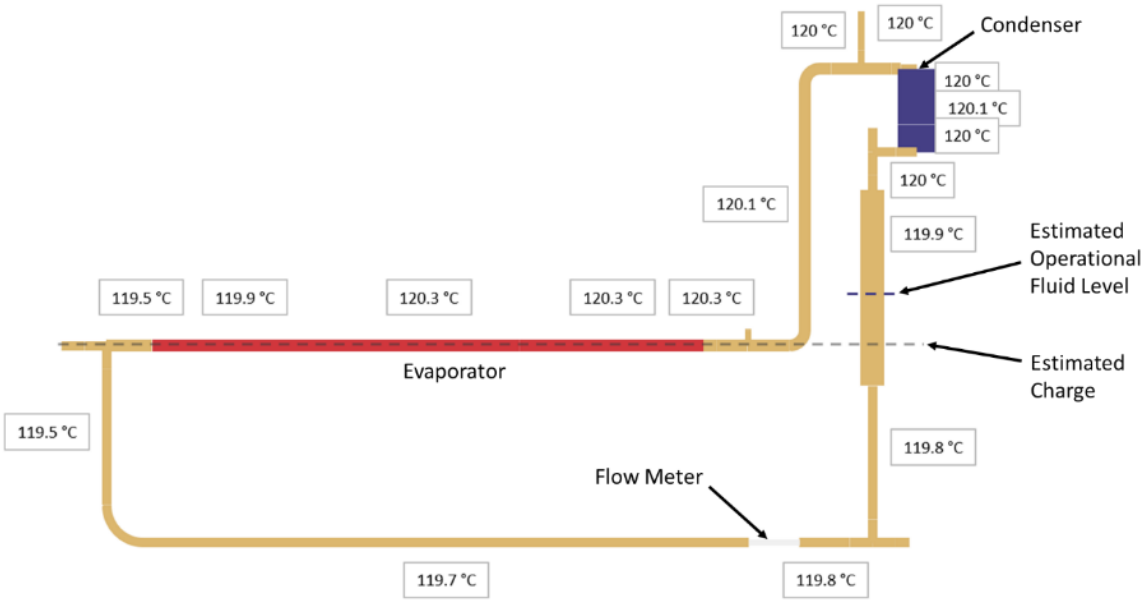

Figure 40: Visual Representation of Sub-Scale LTS as Implemented in Model

The model was used to examine a range of fluid charges and powers of 1-2.5kW for the sub-scale LTS. This modeling was to predict the fluid charge for initial testing. Modeled flow rates and void fractions across a range of charges are presented in Figure 41. A constant fluid saturation temperature of 120°C was used throughout modeling. For each power, charge was increased until the model predicted the liquid fluid return level would reach to the outlet of the condenser. Increasing charge beyond this point will push liquid into the condenser, leading to subcooling of the condensate.

The modeling results were used to select a fluid charge for the initial system testing at 2.5kW and 120°C. As seen in Figure 41, a maximum charge of 2,000ml was suggested. However, when the sub-scale LTS was charged with this quantity of fluid, significant subcooling was found, indicating that the LTS was overcharged. The fluid charge was decreased to the point where further charge decreases did not result in additional reductions in subcooling. Using this method, a maximum fluid charge of 1,700ml was found for the sub-scale LTS.

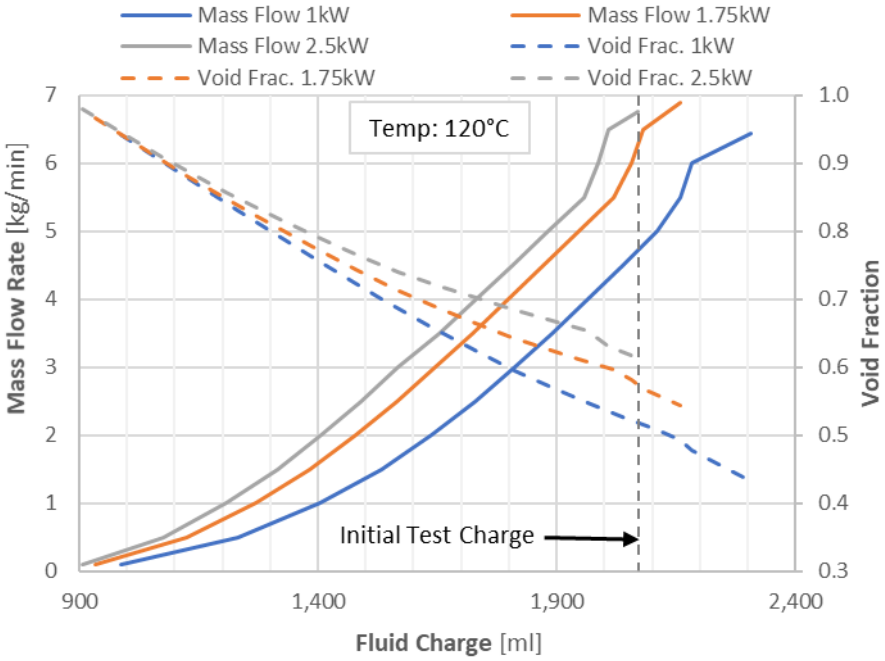

Figure 41: Modeled Mass Flow Rate, Void Fraction for the Sub-Scale LTS

Sub-Scale Loop Thermosyphon Fabrication & Testing

The sub-scale LTS was fabricated by the ACT team. Figure 42 presents the completed sub-scale LTS. The loop is constructed from 25mm ID, 19mm ID copper tubing, which is brazed together and leak-tested to ensure against non-condensable gas infiltration. Heat is supplied by ten, 300W band heaters, which are controlled via a variable-voltage relay driven by a programmable logic controller (PLC). The condenser coolant flow rate is controlled by PLC-controlled proportional flow control values. The PLC is also responsible for data acquisition from the 7 RTDs, 3 pressure transducers, electromagnetic flowmeter, coolant flow rate meter, and heater power transducer.

To test the sub-scale LTS, three fluid charges in the range of 1,700ml (1,650ml, 1,700ml, and 1,750ml) were tested at evaporator powers between 1,000W and 2,500W in 250 W increments. The coolant flow rate to the flat plate condenser was varied such that a constant two-phase saturation temperature was maintained at the inlet to the condenser. Saturation temperatures of 110, 120 and 130°C were tested.

In an LTS, the working fluid mass flow rate is a direct indication of the system's frictional and gravitational pressure drops. This is due to the passive operation of an LTS where the liquid head beneath the condenser drives the two-phase fluid against gravity from the evaporator to condenser. The experimental flow rate results for the three charges are presented vs. evaporator power in Figure 43 (a). As expected, a higher charge leads to a higher flow rate as the driving liquid head beneath the condenser is greater. Flow rate increases with increasing power as higher power leads to an increase in the two-phase void fraction. As the two-phase void fraction decreases, the average density of the two-phase flow decreases. This results in a reduction in the two-phase gravitational head opposing the forward fluid flow. An increase in void fraction also increases the two-phase frictional pressure drop, but for the operating power range considered, the two-phase head decreases more rapidly than the increased frictional pressure drop. This leads to an increase in the flow rate with increasing power. Flattening of the flow rate curves at high powers indicate that the two-phase frictional pressure drop is beginning to offset the gains in flow rate from the reduction in two-phase density.

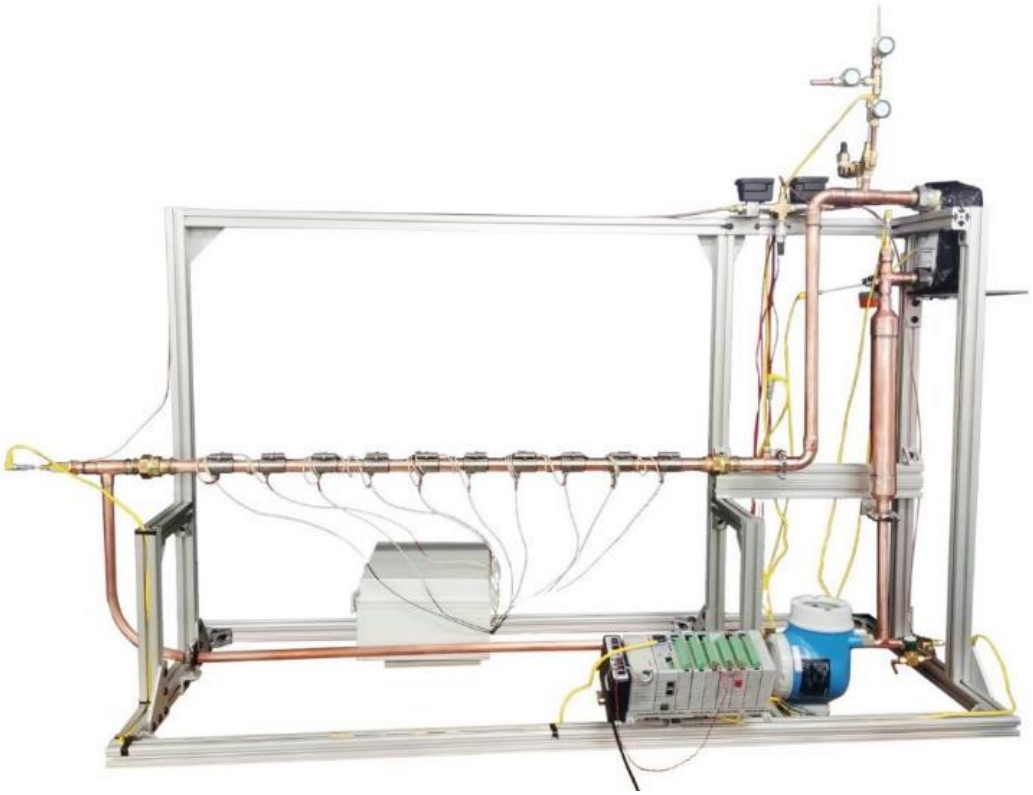

Figure 42: Completed Sub-Scale LTS

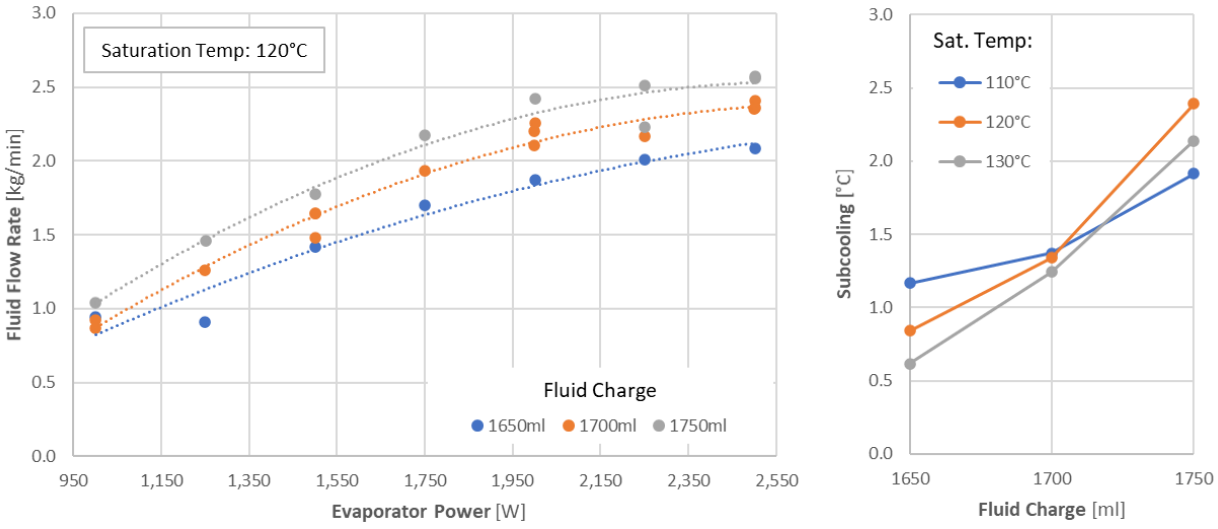

(a) (b)

Figure 43: Experimental Data from Sub-Scale LTS Testing (a) Fluid Flow Rate vs Evaporator Power for a 120°C Saturation Temperature and Three Fluid Charges (b) Subcooling Across Condenser vs. Saturation Temperature and Charge

An important finding of the sub-scale testing was the optimal fluid charge. This was found by varying the charge and examining the subcooling of the condensate leaving the condenser. A higher subcooling indicates that the charge is too high, while subcooling that does not change with decreasing charge indicates liquid is not backing up into the condenser. Average condensate subcooling for the three charges and temperatures is presented in Figure 43 (b), where each point is the average subcooling across all of the tested evaporator powers. The knee in the subcooling curves at 1,700ml indicates that this is the maximum system charge where significant condensate is not backing up into the condenser. Because of this, 1,700ml is proposed as the optimal system charge resulting the maximum fluid flow rate for this LTS. Most LTS systems do not attempt to maximize flow rate. However, for the current system the targeted void fraction between 50 and 70% can only be achieved if flow rate is maximized.

Task 2.5: *Loop Thermosyphon System Model Revision*

In this task, the loop thermosyphon model developed in Task 1.1 was reviewed and revised according to the test results of both the lab-scale and sub-scale LTS systems. This work has led to two conference papers over the past 2 years, and has helped to increase ACT's overall understanding of the fundamentals of two-phase loop thermosyphon flow.

Overview of the LTS Model

As mentioned in the Task 1.1 write-up, the LTS model is constructed around a pressure and energy balance around the loop. The model discretises the loop into sections, which are sequentially operated on. For each section, critical dimensions (diameters, length, inclination, elbow radius, etc.) are user input and are used to define the LTS geometry.

Required model inputs include the working fluid, the saturation temperature, operating temperature, and fluid quality at the entrance or exit of the starting section.

During Task 2.5 the model was improved by adding additional frictional pressure drop correlations. Table 5 presents six well-documented two-phase frictional pressure drop correlations that have been implemented in the model. Each of these correlations uses fluid flow conditions to solve for a liquid or liquid only two-phase multiplier, which is used to find the two-phase pressure drop using either of the following equations:

$$\left(\frac{dP_f}{dz}\right)^{2\phi} = \phi_l^{2\phi}\left(\frac{dP_f}{dz}\right)_{liq} = \phi_g^{2\phi}\left(\frac{dP_f}{dz}\right)_{gas} \quad (24)$$

$$\left(\frac{dP_f}{dz}\right)^{2\phi} = \phi_{lo}^{2\phi}\left(\frac{dP_f}{dz}\right)_{liq} \quad (25)$$

All of the correlations presented in Table 5 are implemented and user-selectable within the LTS model user interface. In addition to an accurate estimation of two-phase pressure drop, accurate correlations predicting the two-phase void fraction are critical to estimating the system fluid charge and heat transfer characteristics. Fifteen well-documented void fraction correlations compiled by Ghajar et al. have been implemented in the model [18**Error! Reference source not found.**]. During BP2 the model interface was updated to allow the user to select the desired pressure-drop and void fraction correlations used.

Comparison of Experimental and Modeling Results

Experimental (EXP) and modeling (MOD), steady-state flow rate results for the sub-scale LTS are presented in Figure 44(a) for 1,650 and 1,750ml fluid charges and saturation temperatures of 110 and 120°C. The modeling results were produced using the Lockhart-Martinelli pressure drop correlation. For all charges and temperatures, increasing evaporator power was found to correlate to an increase in working fluid flow. This is expected as the thermal energy input to the system directly drives the flow through the density reduction of the two-phase working fluid. The trend of increasing flow rate with increasing power was observed in both the experimental and model results. Also, the flattening of the experimental flow rate trend at powers greater than ~2,000W is observed in most of the modeling result curves. The difference between model and experiment is visualized in Figure 44: (b), where modeled mass flow rate is plotted against experimental mass flow rate. For the temperatures and charges considered, the model, on average, overpredicts mass flow rate by between 20 and 30%. While this difference is significant, it is within the typical error associated with the L-M correlation due to the highly complex nature of two-phase flow regimes.

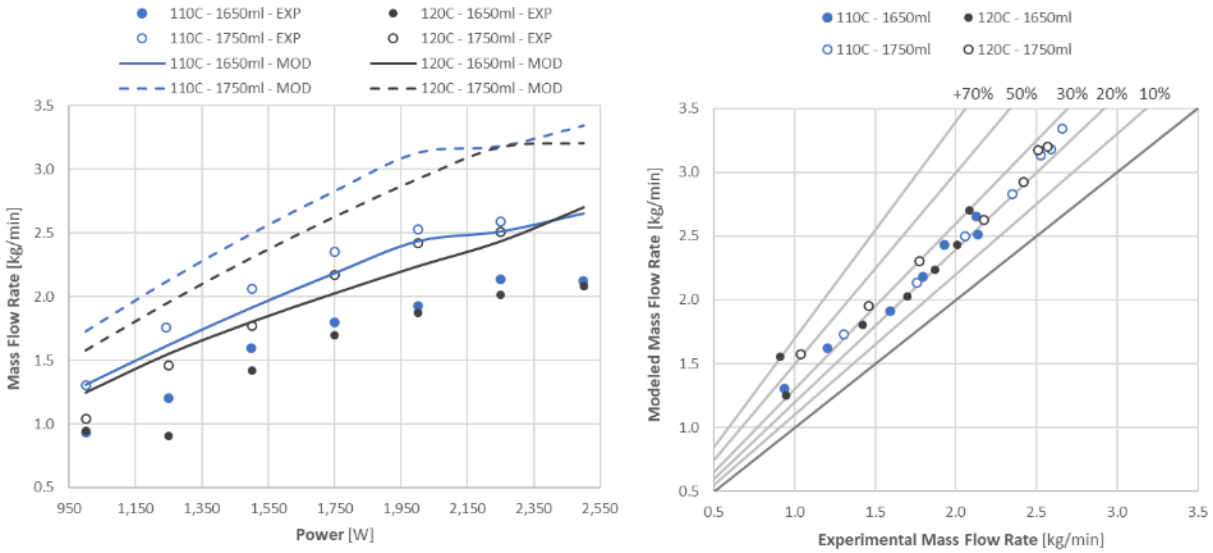

(a) (b)

Figure 44: (a) Modeling and experimental LTS mass flow rate results vs. evaporator power at 110 and 120°C and 1,650 and 1,750ml of charge and (b) the difference in modeled and experimental mass flow rate for the lab-scale LTS.

Table 5: Summary of the two-phase pressure drop correlations implemented in the sectional LTS model

Source	Correlation Equations and Variables		
[5]	$\Phi_l^2 = 1 + \frac{C}{X} + \frac{1}{X^2}$; $X = \sqrt{\frac{\left(\frac{dP_f}{dz}\right)_l}{\left(\frac{dP_f}{dz}\right)_g}}$; C = 5: lam-lam flow, C = 10: lam-turb, C = 12: turb-lam, C = 20: turb-turb		
[13]	$\Phi_l^2 = \left(\left(\frac{1}{1-x}\right)\left(1-\Gamma_{Bf}\left(1-\frac{\rho_g}{\rho_l}\right)\right)^{0.43}\left(1+x\left(\frac{\rho_g}{\rho_l}-1\right)\right)\right)^{1.75}$; $\Gamma_{Bf} = \left(\frac{0.71+2.35\left(\frac{\rho_g}{\rho_l}\right)}{1+\left(\frac{1-x}{x}\right)\left(\frac{\rho_g}{\rho_l}\right)}\right)$		
[14]	$\Phi_{lo}^2 = A_{Fr} + \frac{1.262x^{0.6978}}{We_{go}^{0.1458}}\left(\frac{\rho_l}{\rho_g}\right)^{0.3278}\left(\frac{\mu_g}{\mu_l}\right)^{-1.181}\left(1-\frac{\mu_g}{\mu_l}\right)^{3.477}$; $A_{Fr} = (1-x)^2 + x^2\left(\frac{\rho_l}{\rho_g}\right)\left(\frac{f_{go}}{f_{lo}}\right)$		
[15]	$\Phi_{lo}^2 = 1 + (Y^2-1)\left(B_{CH}x^{(1-0.5n)}\left(1-x^{(1-0.5n)}\right)\right) + x^{(2-n)}$; n = 0.25; $Y^2 = \frac{\left(\frac{dP}{dL}\right)_{go}}{\left(\frac{dP}{dL}\right)_{lo}}$		
	$0 \le Y \le 9.5$	$9.5 < Y \le 28$	$28 < Y$
	$G \le 500$: $B_{CH} = 4.8$ $500 < G < 1900$: $B_{CH} = 2400/G$ $1900 \le G$: $B_{CH} = 55/\sqrt{G}$	$G \le 600$: $B_{CH} = 520/\sqrt{Y^2 G}$ $600 < G$: $B_{CH} = 21/Y$	$B_{CH} = 15000/\left(Y^2\sqrt{G}\right)$

[16,17]	$For\ \theta = 0° \ or + 90°: \Phi_{lo}^2 = A_{Fr} + \frac{3.24x^{0.78}(1-x)^{0.22}\left(\rho_l/\rho_g\right)^{0.91}\left(\mu_g/\mu_l\right)^{0.19}\left(1-\left(\mu_g/\mu_l\right)\right)^{0.7}}{Fr_{lo}^{0.045}We_{lo}^{0.035}}$ $For\ \theta = -90°: \Phi_{lo}^2 = A_{Fr} + \frac{5.7x^{0.7}(1-x)^{0.14}\left(\rho_l/\rho_g\right)^{0.85}\left(\mu_g/\mu_l\right)^{0.36}\left(1-\left(\mu_g/\mu_l\right)\right)^{0.2}}{Fr_{lo}^{0.09}We_{lo}^{0.007}}$ $f_{lo} = 0.25\left(0.86859\ ln\left(\frac{Re_l}{1.964\ ln(Re_l) - 3.8215}\right)\right)^{-2}; f_{go} = 0.25\left(0.86859\ ln\left(\frac{Re_g}{1.964\ ln(Re_g) - 3.8215}\right)\right)^{-2}$ $Fr_{lo} = \frac{G^2}{g d_h \rho_l^2}; We_{lo} = \frac{G^2 d_h}{\sigma \rho_l}; A_{Fr} = (1-x)^2 + x^2\left(\frac{\rho_l}{\rho_g}\right)\left(\frac{f_{go}}{f_{lo}}\right)$
[18,19]	$\Phi_{lo}^2 = 1 + dP_{Fr}\left[\frac{\left(\frac{\rho_L}{\rho_g}\right)}{\left(\frac{\mu_L}{\mu_g}\right)^{0.25}} - 1\right]; dP_{Fr} = f_{Fr}\left(x + 4\left(x^{1.8} - x^{10} f_{Fr}^{0.5}\right)\right); Fr_{lo} = \frac{G^2}{g d_h \rho_l^2}$ $Fr_{lo} \geq 1: f_{Fr} = 1.0; Fr_{lo} < 1: f_{Fr} = Fr_{lo}^{0.3} + 0.0055\left(ln\left[\frac{1}{Fr_{lo}}\right]\right)^2$

Predicting the Performance of an Industrial-Scale Full-Scale System

The passive, gravity-driven nature of the LTS solar collector will introduce a practical upper limit to the length of parabolic trough that can be used. This is because the system frictional pressure drops must be overcome by the liquid head beneath the condenser. As trough length increases and frictional pressure drops along with it, the condenser height must increase in proportion to this length. The greater the condenser height, the greater the material and fabrication costs for the vertical portion of the system.

To examine the relationship between trough length and condenser height, a broad range of trough lengths (30 – 160m) were modeled, corresponding to incident solar flux values between 150 and 800kW. For each configuration, the riser height was adjusted from a minimum value where the charge is at a level corresponding to the midline of the evaporator to a maximum value where the two-phase quality approaches 0. These represent the physical riser height limitations of the LTS system. In total, 180 cases were modeled at trough length increments of 10m. An 80mm OD, 76mm ID receiver tube diameter was assumed with a trough aperture of 5m and nominal irradiance of 1kW/m^2 at the aperture. The 76mm ID tube diameter was maintained from the outlet of the evaporator to the condenser, with a 50mm ID liquid return line. A SWEP B400T 190 plate flat plate heat exchanger was assumed for all cases, with the pressure-drop through the condenser estimated using SWEP's design utility. The range of acceptable riser heights for a given trough length is summarized in Figure 45. A linear relationship between riser height and trough length was found.

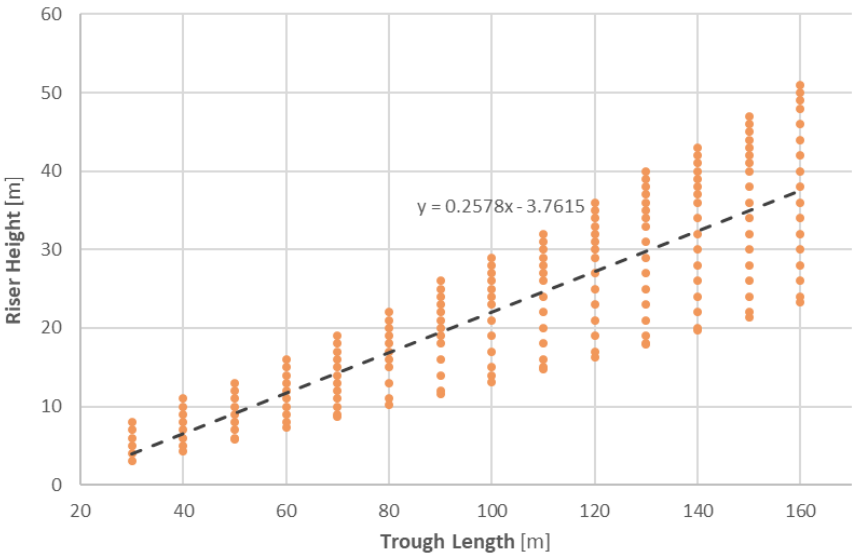

Figure 45: Riser Height vs. Trough Length for the Range of Systems Modeled

The model results were simplified by only accounting for those where the two-phase void fraction lies in the required range between 50 and 70%. The levelized cost of heat for these cases was calculated to find the impact of increasing trough length on lifetime system costs:

$$\mathbf{LCOH} = \frac{\mathbf{I}}{\sum_{\mathbf{t=1}}^{\mathbf{n_l}} \frac{\mathbf{Q \cdot 8760 \cdot CF}}{\mathbf{(1 + r_d)^t}}} + \mathbf{O\&M \cdot n_l} \tag{26}$$

Where *I* is the installed costs, O&M is the operating and maintenance costs, n_l is the discount rate of money, *Q* is the rated power, *CF* is the annual capacity factor, r_d is the annual discount rate, and *t* is time in years. Installed costs are the sum of tube material, insulation, parabolic trough, condenser, and fluid costs. For the tube and insulation, total installed costs are 2.25 times raw material costs to account for manufacturing and installation. For the trough, a cost of \$148/m^2 was assumed with a fixed condenser cost of \$5,236 based on a vender-supplied value.

Calculated LCOH for the different through lengths is plotted against riser height in Figure 46. At the shorter trough lengths, LCOH is found to decrease rapidly, but above a riser height of ~20m further increase in system size shows negligible decreases in LCOH. Given the simplicity of the model in evaluating the impact of system size on system construction costs and the fact that very high structures would be challenging to construct, it is proposed that a practical system be limited to a riser height of 20m. This corresponds to a trough length around 80-90m.

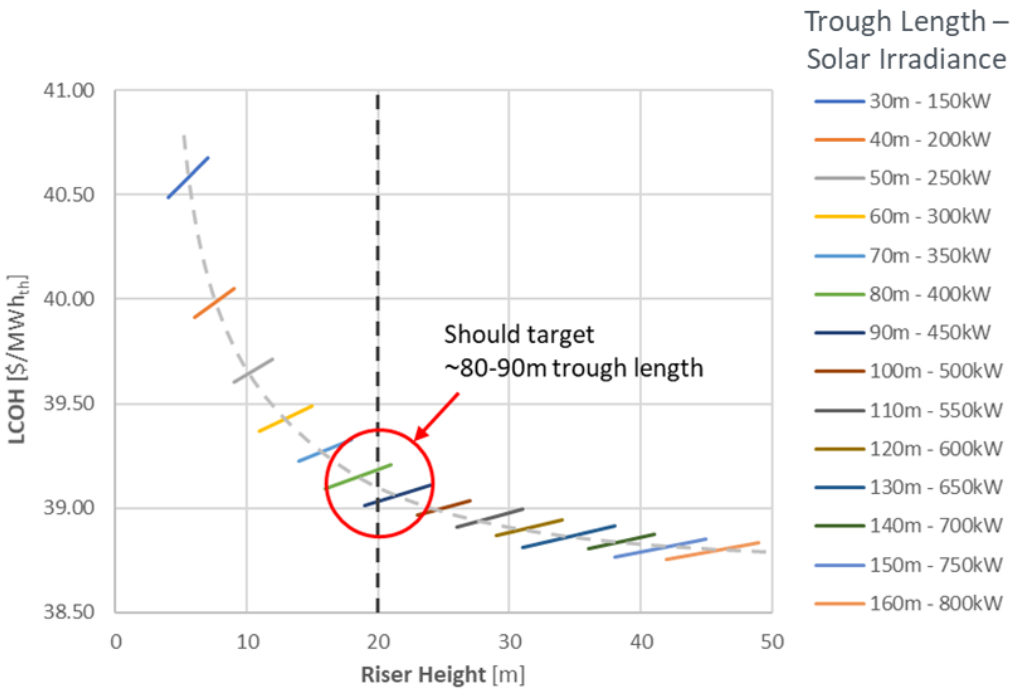

Figure 46: LCOH for the Full-Scale LTS Across the Modeled Range of Trough Lengths

Project Results and Discussion – System Integration

Tasks 3.4 comprises the final system integration task of this project, where the individually developed components, volumetrically absorbing dye, glass receiver, and two-phase loop thermosyphon are combined in a final full-scale system. A summary of the second half of Task 2.3 is also included in this section as the sub-scale solar simulator work was a bridge between the pure LTS research and full-scale on-sun system.

Task 2.3: *Design, Construct, and Test a Sub-Scale Prototype of the Complete Loop Thermosyphon Solar Collector.*

Task 3.3: *Mid-Scale Prototype Testing in Solar Simulator*

The sub-scale LTS was originally designed to allow for integration with a glass receiver and dye working fluid with a solar simulator providing energy to the system. The solar simulator was designed around three 2,500 W_e metal halide lamps. Irradiance from these lamps is collimated using three parabolic dishes, which project the light onto a parabolic trough positioned such that its focal line is coincident with the centerline of the LTS evaporator. The design of the lamps and parabolic trough, and their integration with the sub-scale LTS is presented in Figure 47.

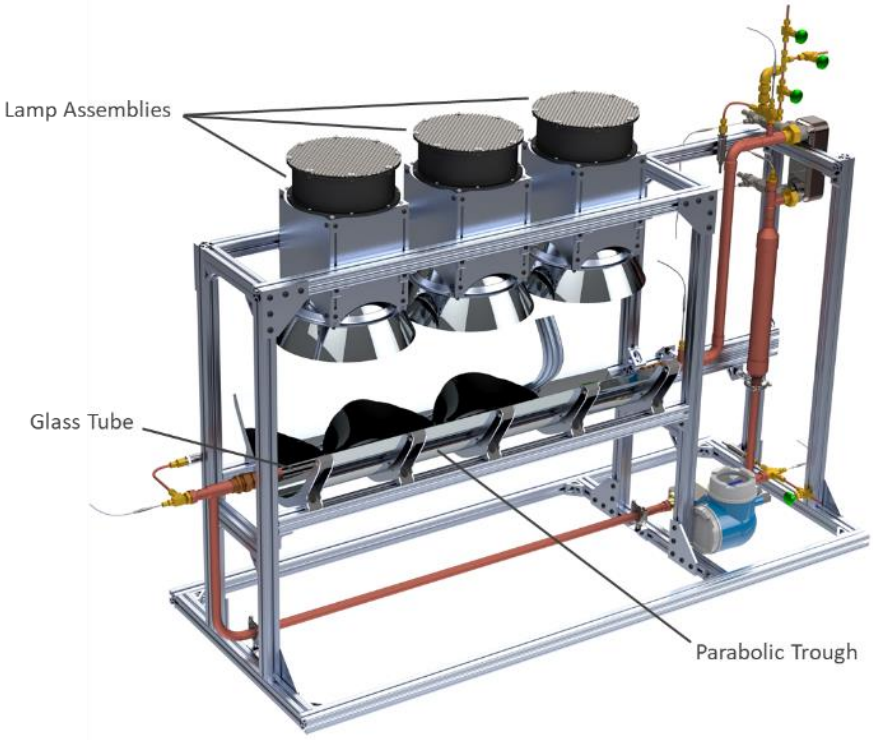

Figure 47: Sub-Scale System Design with 7,500 W Solar Simulator, Parabolic Trough Concentrator, and Glass Evaporator

The lamps source was selected based on their ability to provide the required irradiance, cost, and their match with the solar spectrum. The following three arc-lamps are typically used in solar simulators due to their good spectral match: xenon, argon, and metal halide [20]. For all three technologies, the light is produced through ionization of a gas in the presence of an electrical arc. Xenon arc lamps are the most widely used, followed by metal halide lamps. Argon lamps are not widely used today [20]. Initially, a xenon arc lamp was considered for use in the simulator due to its good spectral match and small arc length [21]. However, as pointed out by Siegel et al. [22], xenon arc lamps are far from inexpensive at costs of up to \$60,000/kW_{th} (delivered). Because of this, Siegel et al. recommended metal halide arc lamps as a suitable and less expensive alternative. Despite being considerably cheaper than xenon lamps, metal halide lamps still have an acceptable match with the solar spectrum, especially for concentrated solar thermal applications, which are less sensitive to spectral variations. The solar spectrum of a typical metal halide lamp is plotted against the solar spectrum in Figure 48 (a).

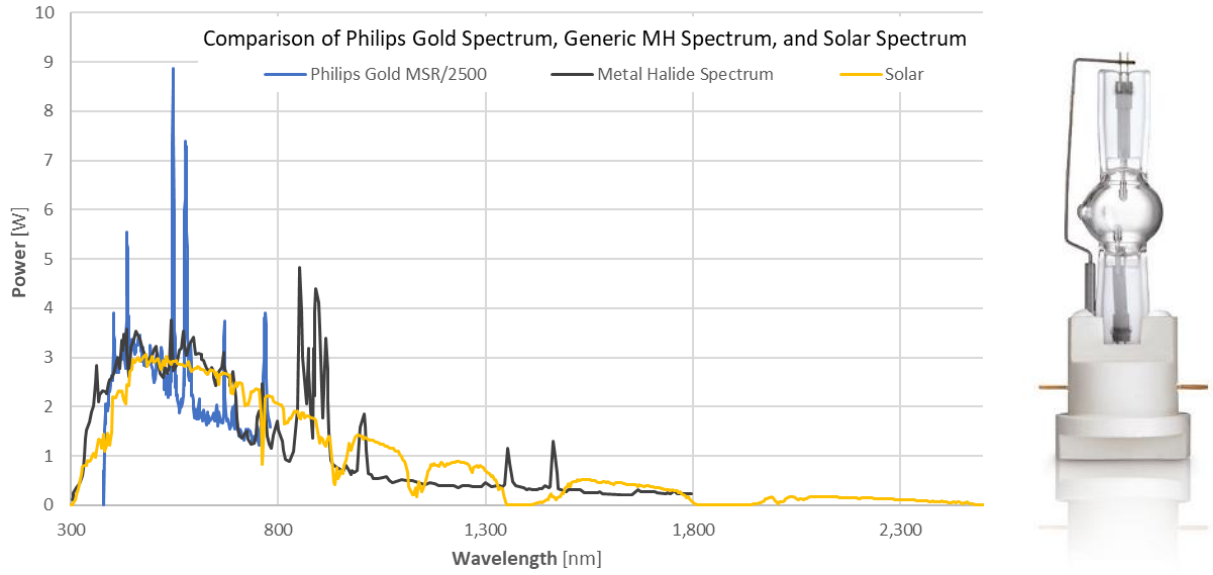

(a) (b)

Figure 48: (a) Comparison of Methal Halide, Philips Gold MSR, and Solar Spectrums (b) Philips MSR Gold 2500/2 Metal Halide Lamp Selected for the Solar Simulator

Siegel et al. proposed the use of the Philips MSR Gold metal halide lamp [22]. This lamp is available at powers up to 2,500 W_e and is designed for use in a single lamp holder, which simplifies its integration into a parabolic reflector. With a short arc length of 9.5 mm [23], the MSR lamp closely approximates a point source, which increases the optical efficiency of the reflector and/or any other focusing optics. To convert the quasi-point source of the Philips lamp into a columnar beam, electroplated parabolic dishes by Optiforms (Model P38) have been selected. The dishes are coated with Optiforms's protected silver coating, which was selected due to its excellent reflectance at wavelengths greater than ~400 nm. The MSR lamp mounts through the rear aperture of each dish with a lamp support bracket used to position to the center of the arc at the focal point of the dish. An illustration of the solar simulator lamp assembly design is presented in Figure 49. The dish and lamp support are attached to a simple aluminum frame, which in turn attaches to the sub-scale LTS frame. The end of the frame opposite the dish connects to a 10" diameter fan, which is used to remove excess heat from the backside of the lamp and dish. Thin aluminum shields on each side of the lamp assembly to prevent potentially hazardous

Figure 49: Metal Halide Solar Simulator Lamp Assembly Design

light leakage. As illustrated in Figure 47, the three lamp assemblies were placed above the horizontal LTS evaporator with the dishes aimed downwards towards the tube. A 15" aperture aluminum parabolic trough placed beneath the horizontal evaporator concentrates the columnar light from the lamp assemblies onto the glass evaporator located along the trough's focal line. To examine the performance of this three-lamp solar simulator and the reflector geometries, the system was modeled using the TracePro ray-tracing software package.

After importing the Solidworks model of the lamp assemblies, trough, and evaporator tube into TracePro, representative surface and material properties were applied to each surface and/or solid within the model. For the parabolic dishes, the spectral-weighted reflectance was specified using the values for protected silver supplied by Optiforms. For the trough, the spectral reflectance of aluminum was used. Both the glass dome of the lamp and the evaporator tube were specified as Pyrex borosilicate glass, which is a pre-defined material property within TracePro. For the dye, 100% absorption was assumed. To simulate the arc light source, the irradiance produced by each lamp was evenly spread across the surface of a 9.5 mm long cylinder placed between the electrodes of the bulb. An electrical to irradiance efficiency of 75% was assumed, meaning 1,875 W is released from each arc cylinder. The spectral intensity of the light source was matched to that supplied by Philips for the MSR Gold lamp [23]. In total, around 500,000 rays were traced from the three lamp sources. An illustration of 1% of traced rays between the source and evaporator tube is presented in Figure 50.

The most important design criteria for the solar simulator/parabolic trough system is the distribution and magnitude of thermal energy delivered to the evaporator. In other words, what are the optical losses of the system? To analyze this, the irradiance flux incident on the top and bottom surface of the dye was found using the ray-trace analysis presented above. The results of this analysis are visually presented in Figure 51.

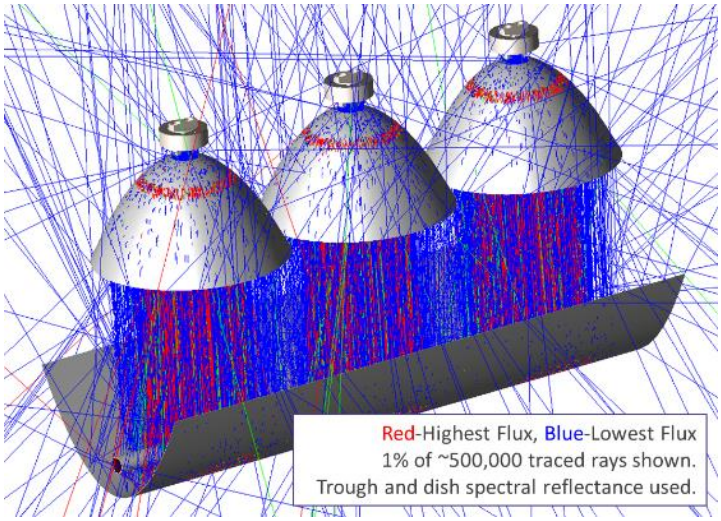

Figure 50: Ray Tracing of Philips Gold MSR Lamps Across Parabolic Dishes, Trough, and onto Glass Tube

As expected, most of the energy strikes the surface of the dye at points roughly below the three lamp assemblies. The upper surface of the dye receives in total 658 W, which is partially due to rays directly striking the tube from above and partially due to rays reflected from the edges of the trough onto the sides of the tube. The bottom surface of the dye receives nearly 4 times the power as the top surface at 2,494 W. This higher flux is expected as most of the rays incident on the trough surface will be reflected onto the lower half of the evaporator surface. In total, 3,152 W is predicted to reach the surface of the dye, or 42% of the electrical power input

to the lamps.

There are significant non-uniformities in flux seen along the length of the evaporator, with six defined “hot spots” located adjacent to the centerline of each lamp assembly. This is not expected to be an issue for the evaporator due to the highly turbulent nature of the boiling working fluid, which enhances mixing and temperature uniformity within the flow.

The three metal halide lamps are driven by electronic ballasts capable of dimming the bulbs to ~50% of their maximum intensity. This allows for solar receiver testing at powers as low as 1,500 W, which is important given the variability in the solar resource across time.

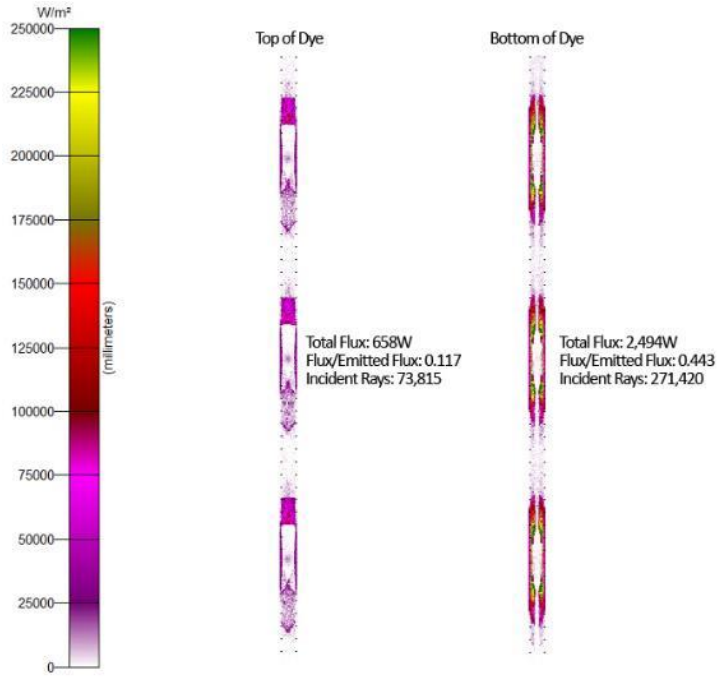

Figure 51: Ray Trace Flux Absorbed onto Top and Bottom Surface of the Dye Filling the Glass Evaporator Tube

Calibration of the Solar Simulator

After completing the construction of the solar simulator, a steel pipe with a high absorptivity surface coating was used to calibrate the simulator. Figure 52 presents the coated stainless-steel pipe before testing and the coating spectral absorptance.

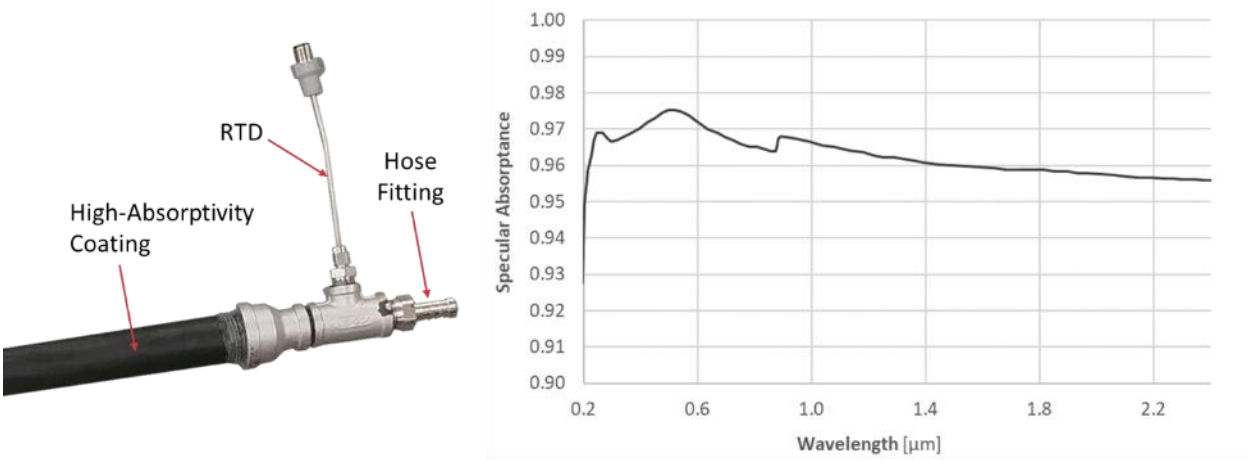

Figure 52: (left) Coated Stainless Steel Receiver and (right) High Absorptivity Coating Spectral Absorptance Used for Ray-Tracing

After the solar simulator was assembled, the stainless-steel receiver was connected to a chilled water loop. An electromagnetic flowmeter monitored the water flow rate into the receiver, while RTDs at the inlet and outlet of the pipe recorded the water temperature rise across the receiver. First, the system was operated with all three lamps at powers between 50 and 100% of their rated value. Next, lamps were selectively turned off to note the impact on the heat absorbed into the water. Figure 53 shows the linear solar simulator during calibration runs.

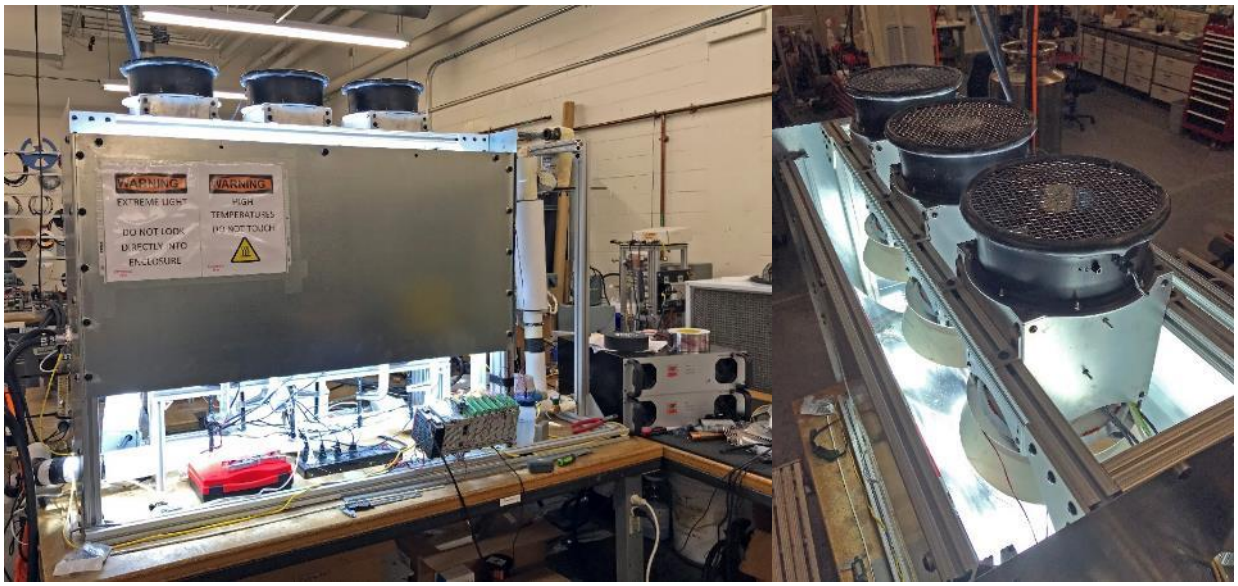

Figure 53: (left) View of the Linear Solar Simulator During a Calibration Run and (right) Looking Down into the Simulator During Calibration

Calibration runs were conducted at average water temperatures between 16 and 67°C to determine the impact of convective losses from the steel tube The lamp current and voltage were recorded for each test case. It was found that each lamp would operate at a nominal power of 3,065W (123% of rated nominal power). At maximum lamp power, an average electric-to-absorbed thermal energy efficiency of 50.8% was found after correcting for convective and radiative losses from the un-insulated receiver tube. This dropped to 47.4% at 75% power and 38.8% at 50% power. It is believed that this decrease in efficiency with decreasing lamp power is due to a decrease in lamp efficiency at reduced power levels. These experimental calibration data points are summarized in Table 6.

Table 6: Summary of the Experimental Solar Simulator Calibration Results

Lamp Power	$Power_e$ [W]	$Power_{rec}$ [W]	Elec. to Therm. Eff.
100%	9,194	4,668	0.508
75%	6,391	3,029	0.474
50%	3,443	1,337	0.388

The solar simulator calibration system was modeled in Solidworks and imported into TracePro for a detailed ray-tracing analysis. This analysis was completed in a similar fashion to that for the glass receiver-tubed system (Figure 50) however the glass tube was replaced by the coated stainless-steel pipe.

The heat flux absorbed by the calibration receiver tube for 100% power and 86% lamp efficiency is shown in Figure 54. Approximately 1/3 of the total thermal energy is absorbed onto the top of the tube with the remainder absorbed on the bottom surface after reflecting from the parabolic trough. As expected, there are three distinct "hot spots" along the length of the tube as the parabolic dishes result in three circular parallel beams incident on the trough. While this isn't ideal, the highly turbulent flow within an evaporative receiver will help to minimize temperature gradients within the working fluid.

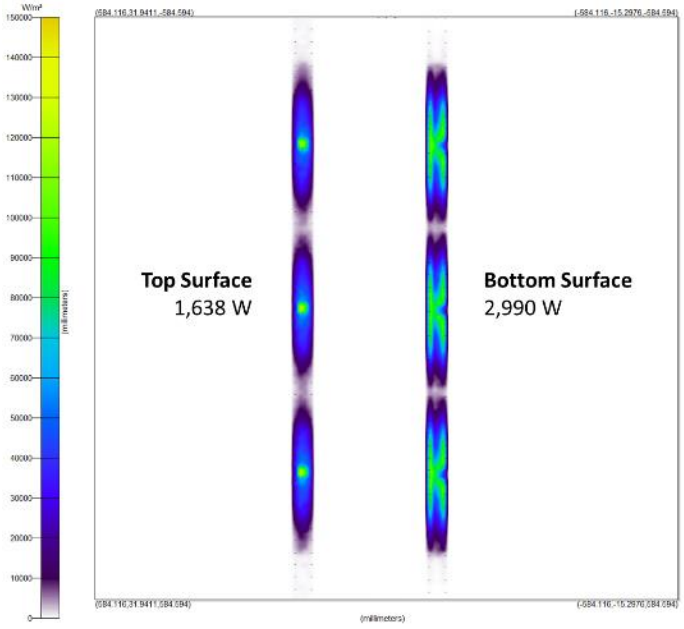

Figure 54: Ray-Tracing Results for Irradiance Absorbed onto the Top and Bottom Hemispheres of the Steel Receiver Tube at 100% Power and 86% Lamp Efficiency

Solar Simulator Testing with Glass Receiver and Dye

After validating the performance of the linear solar simulator with the stainless-steel tube, the stainless tube was replaced with a 1¼" OD x 42" medium-wall borosilicate glass tube. Brass O-ring flanges identical to those used in the thermal cycling test terminate the ends of the glass tube. A larger-diameter (2¼" OD) medium-wall tube was designed to fit over the outside of the brass flanges to provide a vacuum annulus around the receiver tube. However, during assembly, the team experienced several outer tube breakages and proceeded without fitting the outer glass tube. The project team charged the BP2 sub-scale LTS with linear solar simulator with 1,700ml of the Acid Black 52 dye developed for volumetric adsorption of solar energy. Figure 55 shows the sub-scale LTS with solar simulator filled with dye before testing.

Testing of the sub-scale LTS with solar simulator began by starting all three lamps at their lowest power setting of 50%. The stainless-steel calibration data showed a total lamp power of 2.7kW$_e$ at 50% dimming results in irradiance of approximately 1.9kW, or a lamp electrical to radiation efficiency of 70.5%. The dye successfully boiled and circulated around the LTS at this power level. Figure 56 shows dye boiling in the glass receiver directly below the third lamp at 50% power. When lamp power increased to 60%, the glass receiver suffered breakages on two occasions. The first failure was due to misalignment of the two brass O-ring fittings, which introduced a twisting moment on the

ends of the tube. This tube cracked at the glass-metal joint. The second failure is likely due to thermal stresses resulting from the localized "hot spots" directly beneath each lamp. This tube cracked directly beneath the middle lamp.

Figure 55: Sub-Scale LTS with the Solar Simulator Filled with Acid Black 52 Dye

Figure 56: Boiling of the Dye Working Fluid During Application of Simulated Solar Energy

Modeling during Task 1.5 (Figures 23 and 24) predicted only marginal improvements in overall system performance resulting from the use of a glass receiver and volumetric absorption working fluid. Although volumetric absorption can increase overall solar energy absorption by a few percentage points, state-of-the-art receivers have absorptivity efficiencies upwards of 94%, resulting in marginal system-level performance gains. Using a loop thermosyphon for thermal transport and fluid circulation more significantly impacted the levelized cost of heat by eliminating the working fluid pump. The two-phase working fluid more efficiently transports thermal energy at a lower temperature, reducing thermal losses to the environment and requiring a small heat exchanger.

Because of the glass tube breakages, short project timeline, and marginal performance gains due to volumetric absorption, the team replaced the glass receiver with a copper receiver with a high-absorptivity coating. Deionized water replaced the Acid Black 52-based working fluid. Figure 57 presents the sub-scale LTS with a copper receiver tube fitting into the existing O-ring brass flanges.

The sub-scale system was operated at three charges (1,650, 1,750, and 1,850ml) and three saturation temperatures (110, 120, and 130°C), at lamp powers of 50, 75, and 100% of full brightness.

In an LTS, the working fluid mass flow rate directly indicates the system's frictional and gravitational pressure drops. LTS pressure drop is critical to its successful operation as the liquid head beneath the condenser must overcome both the two-phase working fluid's mass as it rises to the condenser and the sum of frictional pressure drops around the loop. Figure 58 presents the working fluid mass flow rate vs. lamp power for the three charges tested in the sub-scale LTS with linear solar simulator at a saturation temperature of 120°C.

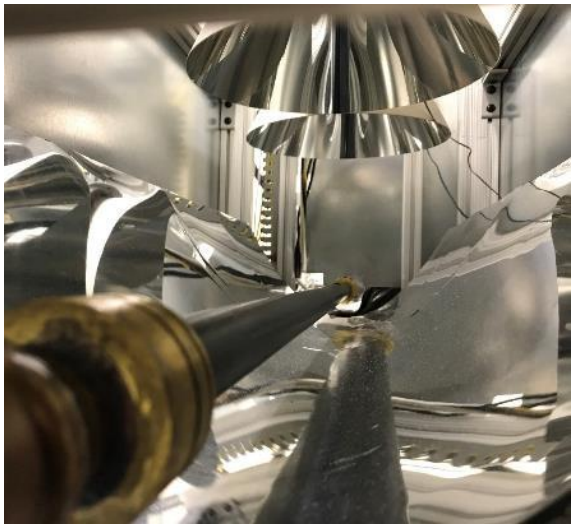

Figure 57: Sub-Scale LTS with Solar Simulator and Copper Receiver with High-Absorptivity Surface Coating.

Figure 58 shows that a higher charge leads to a higher flow rate as the driving liquid head beneath the condenser is greater. The flow rate increases with increasing power as higher powers increase the two-phase void fraction. As the two-phase void fraction decreases, the average density of the two-phase flow decreases, decreasing the two-phase gravitational head opposing the forward fluid flow. An increase in void fraction also increases the two-phase frictional pressure drop, but for the operating power range considered, the two-phase head decreases more rapidly than the increased frictional pressure drop. This leads to an increase in the flow rate with increasing power. These results are comparable to those found for the electrically heated sub-scale LTS.

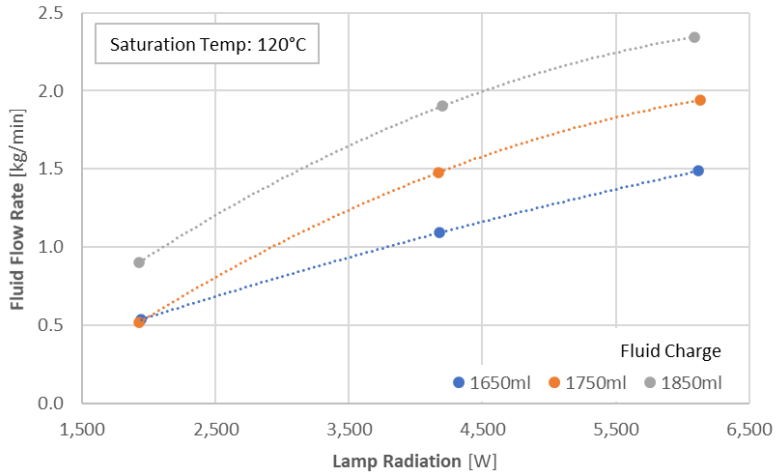

Figure 58: Water Flow Rate vs. Charge and Lamp Power for the Three Charges Tested in the Sub-Scale LTS with Linear Solar Simulator

Task 3.4: *Full-Scale Prototype Design, Fabrication, and Testing*

A full-scale sun heated parabolic trough LTS was designed around a parabolic trough produced by Environmental Solar Systems (ESS) of Methuen, MA. The EES trough consists of four mirrored aluminum trough sections, with a combined aperture area of

6.6m^2. The full-scale LTS system is designed for a maximum absorbed power of 5.3kW at a direct normal irradiance (DNI) of 1,000 W/m^2. Figure 59 illustrates the final design of the ESS parabolic trough LTS system.

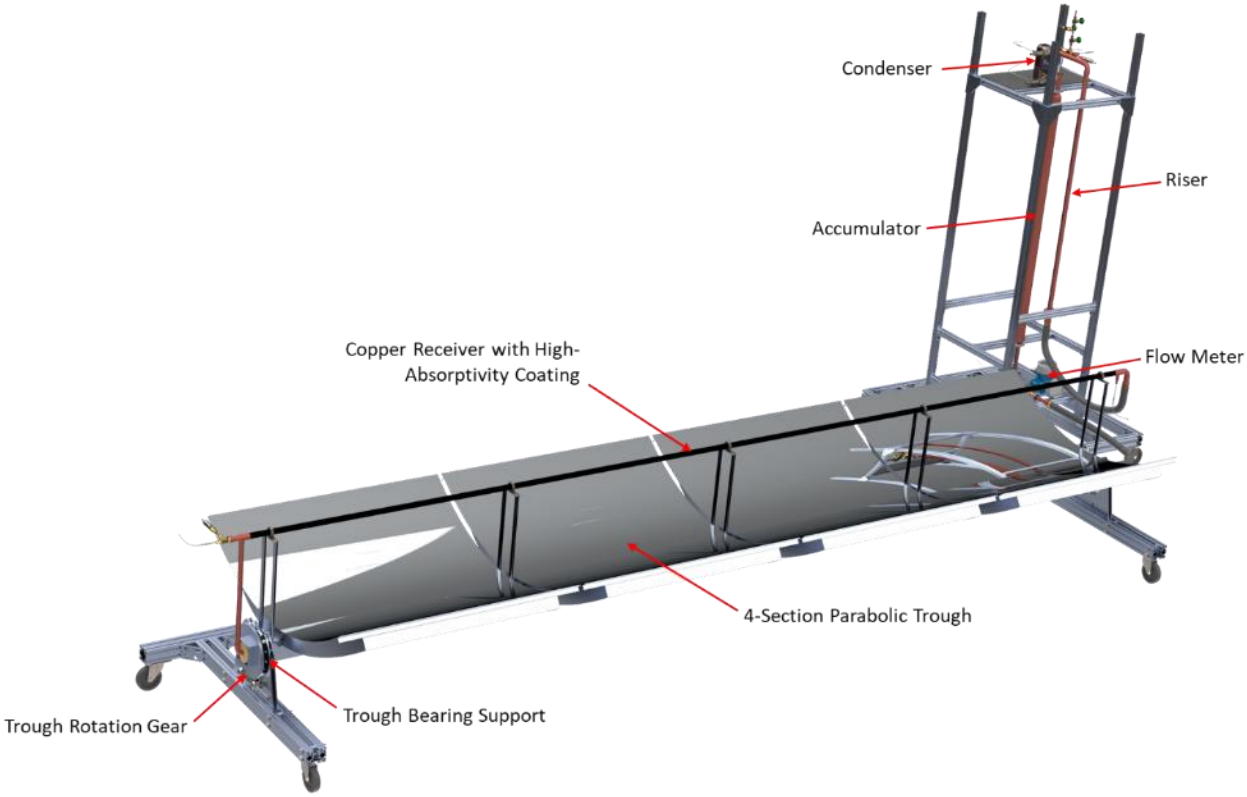

Figure 59: ESS Parabolic Trough-Based Full-Scale LTS Design

The four, 1.25m x 1.3m parabolic troughs focus incident sunlight onto the 1¼" OD copper receiver located along the focal line of the trough. Vapor generated in the receiver rises to the flat plate condenser, where it is condensed. The copper receiver is coated with a high-absorptivity coating to maximize irradiance absorption by the working fluid.

Ray Tracing

The ESS parabolic trough and receiver 3D model were imported into TracePro for ray-tracing. This initial modeling was completed for the full-scale system with a glass receiver. However, after the tube breakage difficulties experienced by the team, the full-scale system was fabricated using a copper receiver with high-absorptivity coating.

Material properties for the trough, mounts, glass tubes, and tube ends were applied to the ray-tracing model along with an appropriate spectral reflectivity for mirrored aluminum trough surface. Similarly, a wavelength-dependent refractive index for borosilicate glass was specified for the glass tubes to account for reflective and refractive losses across the tubes. A planar grid source 3 meters above the trough was used to approximate the sun at an infinite distance from the trough and a dithered rectangular ray distribution was assumed across the plane surface with an irradiance flux of 1,000 W/m^2. Discrete wavelength-dependent irradiance magnitudes approximating the ground-level solar

spectrum were applied to the surface source plane. Figure 60 presents a comparison of the ground-level solar spectrum and the discrete irradiance magnitudes used in TracePro.

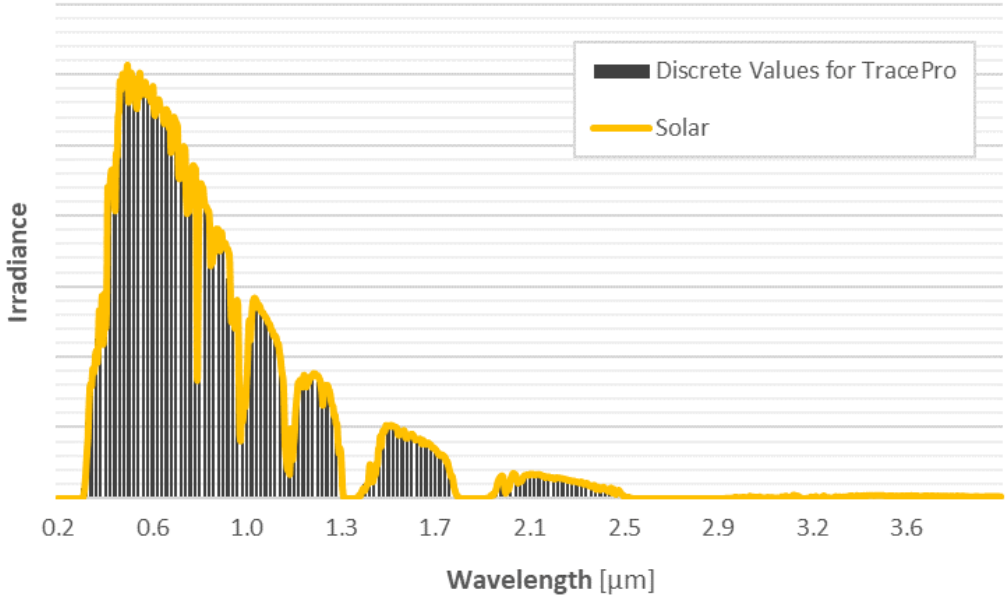

Figure 60: Comparison of the Solar Spectrum at Ground Level and the Discrete Wavelength-Dependent Irradiance Magnitudes Applied to the Planar Grid Source in TracePro.

For a single axis tracking parabolic trough, incident rays rarely lie along a line normal to the trough aperture plane. The angle between the aperture plane normal vector and incident rays is defined as the incidence angle (*i*). The incidence angle varies throughout a day based on the time of year, trough location, and orientation of the trough (N-S vs E-W). The ray source plane was angled relative to the trough aperture normal vector to simulate incidence angles between 0 and 76°. Figure 61 illustrates the trough with the incidence angle labeled.

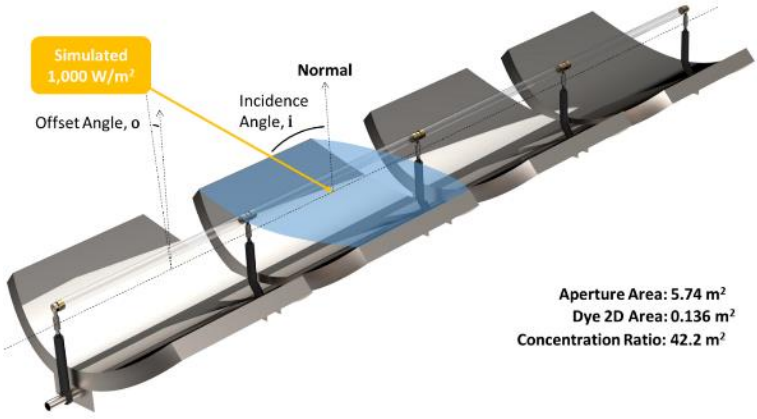

Figure 61: Incidence and Offset Angles as Examined During Ray-Tracing of the EES Parabolic Trough with Glass Tube Solar Receivers.

More than 21 million rays were traced from the planar source grid towards the trough aperture. The plane was tilted to simulate incidence angles between 0 and 76° with the key result parameter being energy absorbed by the dye. Table 7 summarizes these ray-

tracing results and Figure 62 visualizes 0.01% of total traced rays for incidence angles of 0, 45, and 76°.

Table 7: Summary of Ray-Tracing Results Across a Range of Incidence Angles

Incidence Angle (*i*) [°]	Power Reflected by Trough [W]	Power Absorbed by Trough [W]	Power Incident on Inner Tube Surface [W]	Dye Absorbed Power [W]
0	5,086	483	4,769	4,594
14	4,981	473	4,448	4,284
26.6	4,706	447	3,849	3,703
26.6	4,197	399	3,330	3,193
45	3,702	352	2,826	2,691
56.3	3,095	294	1,991	1,849
66	2,360	224	1,199	1,047
76	1,404	133	1,418	309

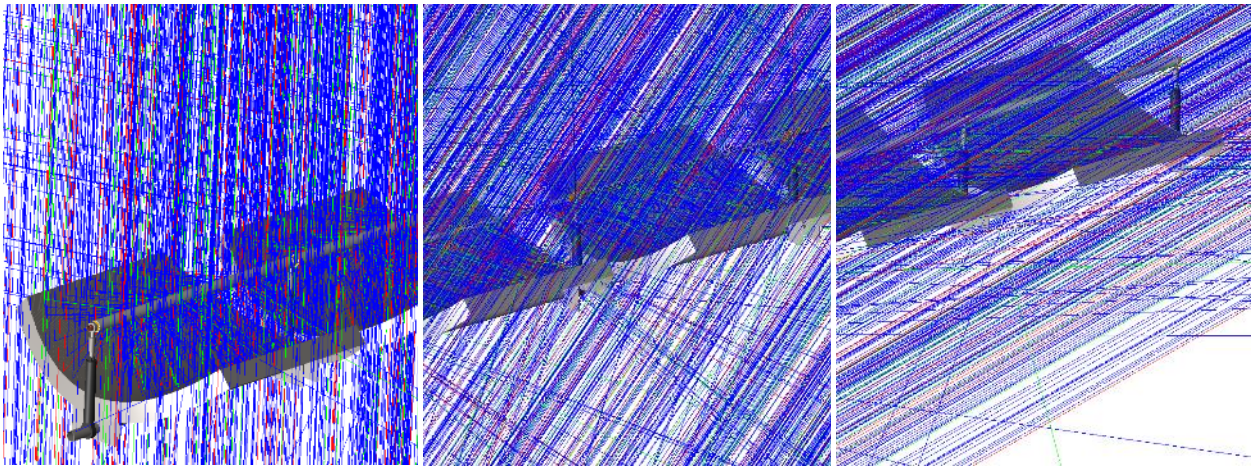

i = 0° *i* = 45° *i* = 76°

Figure 62: 0.01% of 21,120,000 Traced Rays for Full-Scale LTS System at Three Incidence Angles

Since the EES trough is relatively short, as the incidence angle increases, an increasing percentage of incident irradiance reflects towards a focal line beyond the end of the receiver tube. At the other end of the trough, a portion of the last tube does not receive irradiance because of the reflection angle from the trough surface. Figures 63 and 64 illustrate this effect for incidence angles of 0 and 45°, respectively. For an incidence angle of 0° (Figure 63), incident irradiance is absorbed uniformly across the tube sections. Figure 64 illustrates what happens at an incidence angle of 45°. First, gaps in absorbed irradiance open in each tube section due to the gaps between the trough sections. More importantly, a large portion of "Tube 4" receives no irradiance due to the angle of reflection

from the trough surface. This loss of absorbed irradiance becomes pronounced at high incidence angles.

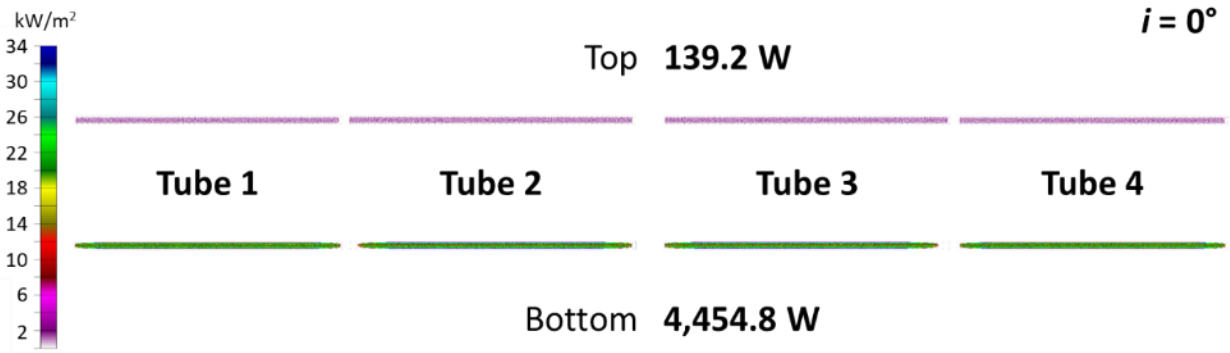

Figure 63: Absorbed Irradiance for an Incidence Angle of 0°

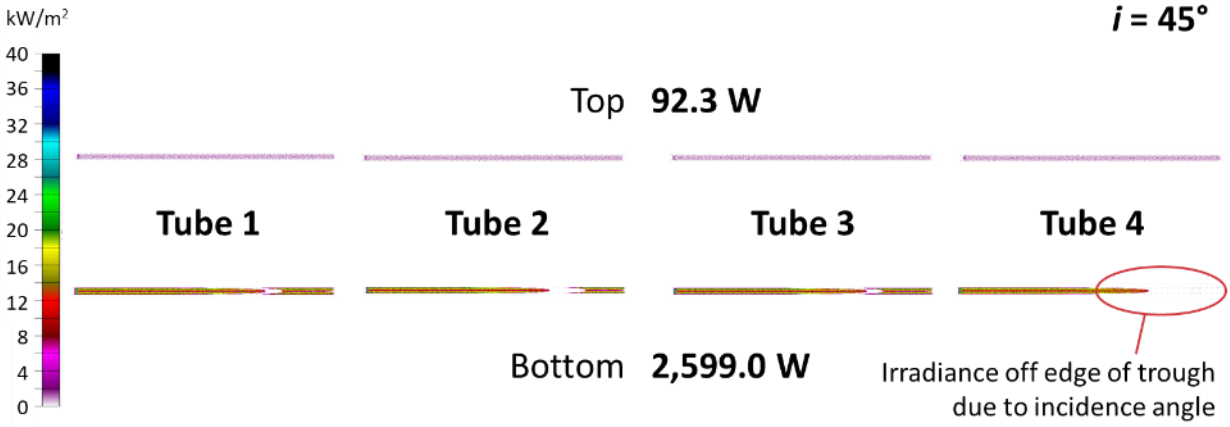

Figure 64: Absorbed Irradiance for an Incidence Angle of 45°

Figure 65 presents dye absorbed power across all modeled incidence angles. By the maximum modeled incidence angle of 76°, dye absorbed power approaches zero. It is critical to optimize the trough's tracking axis to minimize the incidence angle throughout the day. As expected, Figure 65 shows that the power contribution from the four trough sections does not remain uniform as *i* increases. In particular, the power contribution from Tube 4

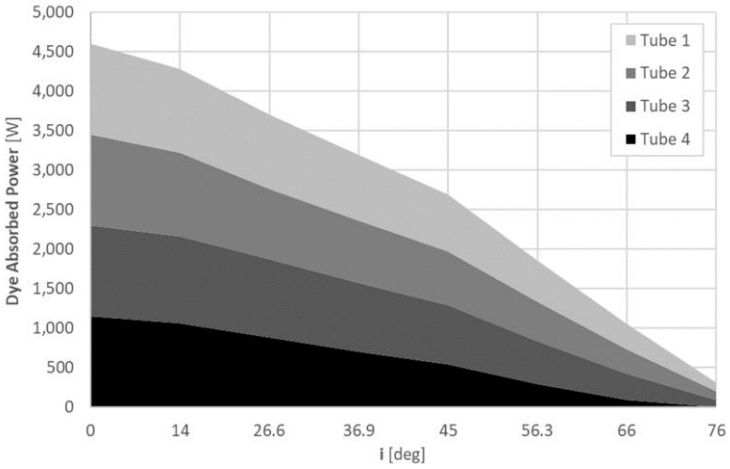

Figure 65: Ray-Tracing Results for Dye Absorbed Power vs. Incidence Angle (*i*)

approaches zero at incidence angles greater than ~66°.

Loop Thermosyphon Modeling

Modeling of absorbed power vs. incidence angle is only the first step to modeling the performance of the full-scale LTS. The loop thermosyphon model developed during Task 1.1 was used to model the performance of the entire system across the range of absorbed power predicted by ray-tracing. A visualization of the full-scale LTS model is presented in Figure 66.

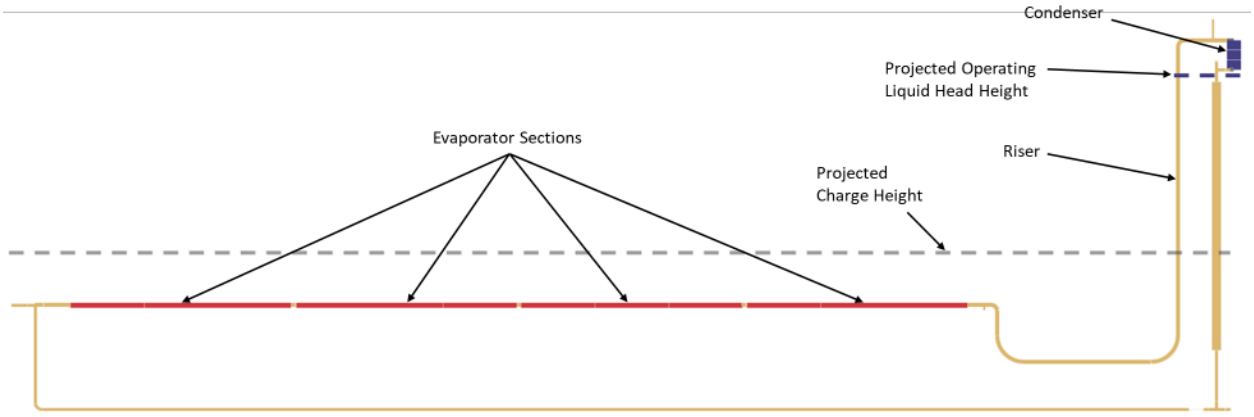

Figure 66: LTS Model Illustration Showing the Full-Scale System Layout

The primary purpose of the full-scale LTS model is to predict the necessary condenser height for the target trough length. Condenser height was defined by the riser length. The full-scale LTS model was run across a range of evaporator powers corresponding to incidence angles between 0 and 66° with riser lengths of 66”, 76”, and 86” modeled. For each power/riser length modeled, a range of fluid charge conditions were modeled. The maximum fluid charge condition was defined as the charge that results in the downcomer liquid level reaching the outlet of the condenser during operation. Minimum charge is defined as the quantity of fluid needed to fill the lower part of the system such that the evaporator is half-filled. This minimum charge was fixed based on the system geometry at approximately 4.5 liters.

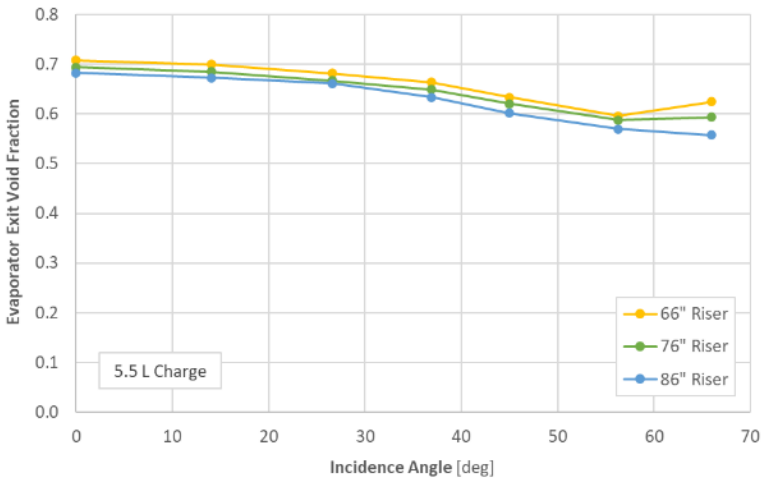

Figure 67: Evaporator Exit Void Fraction vs. Incidence Angle and Riser Length

The model predicted that the system can operate at riser lengths of 66”, 76”, and 86” although the longer riser can accommodate a larger fluid charge and tends to have a slightly lower two-phase void fraction. A dye void fraction less than 70% is targeted at the

evaporator exit to ensure all of the sunlight concentrated onto the receiver can be absorbed by the absorptive working fluid. Modeled evaporator exit void fraction is plotted against incidence angle and riser length in Figure 67.

Figure 67 shows that all three riser lengths have a similar two-phase void fraction prediction. However, the 66" riser is slightly above the upper-limit void fraction target of 0.7 at an incidence angle of 0°. Figure 67 suggests that a taller condenser is better. However, a taller condenser results in additional system costs (materials and manufacturing) and the additional loop length increases frictional pressure drop, which can decrease overall thermal efficiency. To examine the system's thermal efficiency, the power removed in the condenser (available for the end-use desalination process) is plotted against the incidence angle in Figure 68.

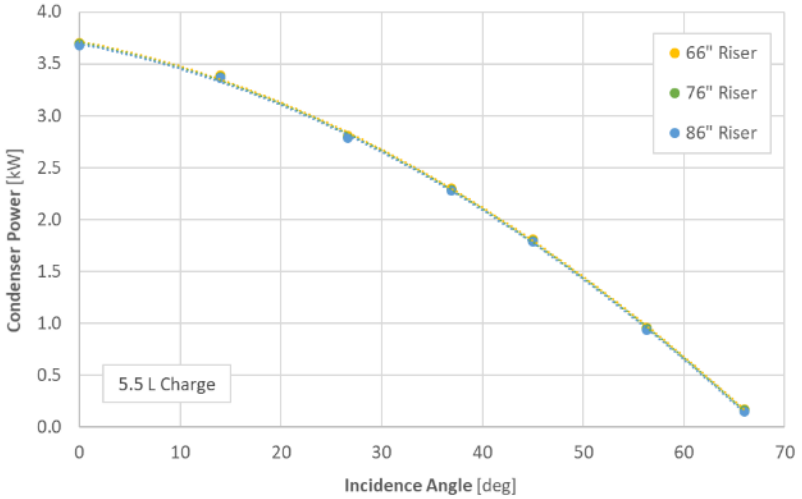

Figure 68: LTS Modeling Results for Condenser Power vs. Incidence Angle and Riser Height at a 5.5 Liter Fluid Charge

Figure 68 shows that riser length has little impact on the thermal transport of the system with negligible differences in condenser power between the three riser lengths. What is significant is the drop-off in condenser power at high incidence angles with the system ceasing to operate at incidence angles greater than ~68°. A riser height of 76" was selected as it provides a slightly higher two-phase void fraction, without significantly impacting the system's thermal performance.

With riser height selected, the team ran the model across the range of solar powers predicted by the ray-tracing analysis. In other words, receiver power varied from 1.2kW at an incidence angle of 66° to 5.3kW at an incidence angle of 0°. A key process parameter produced by this modeling is the minimum and maximum fluid charge for successful operation at each power. Figure 69 presents these modeling results. A charge range between ~5 and 7.5l is predicted for all powers. At incidence angles between ~40 and 60°, the maximum charge increases slightly, but since the loop must operate across a range of solar irradiance values, a slightly lower charge of 7l was selected for the full-scale system.

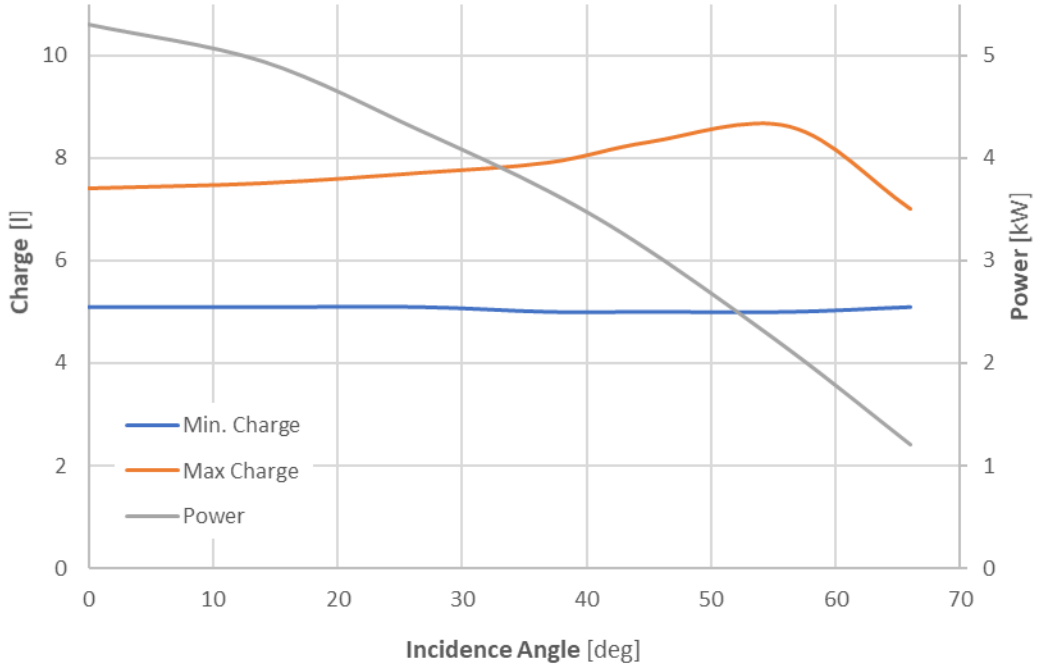

Figure 69: Full-Scale LTS Modeling Results Predicting Min. and Max. Charge for Incidence Angles Between 0 and 66°

Solar Modeling

Solar irradiance information for Lancaster, PA [40.05397, -76.28297] (ACT's testing location) was used to predict the on-sun performance of the full-scale LTS. The following well-known equations were used to calculate the solar elevation angle (θ_{el}) and azimuth angle (θ_{az}):

$$\theta_{dec}\ (declination\ angle) = 23.45° \sin\left[\frac{360}{365}(280 + n_{day})\right] \quad (27)$$

$$\theta_{el} = \sin^{-1}[\sin(\theta_{dec})\sin(lat) + \cos(\theta_{dec})\cos(lat)\cos(\theta_h)] \quad (28)$$

$$\theta_{az} = \cos^{-1}\left[\frac{\cos(\theta_{dec})\sin(lat)\cos(\theta_h) - \sin(\theta_{dec})\cos(lat)}{\cos(\theta_{alt})}\right] \quad (29)$$

Where n_{day} is the day of the year, *lat* is the latitude angle, and θ_h is the hour angle. The elevation angle varies greatly throughout the year due to the earth's axis tilt. Figure 70 plots elevation angle vs. the hour of the day for an average day of each month. As expected, in the summer months of June and July, the sun rises to its highest annual elevation angle at approximately noon (hour 12). The winter months of December and January have the lowest peak elevation angles of the year.

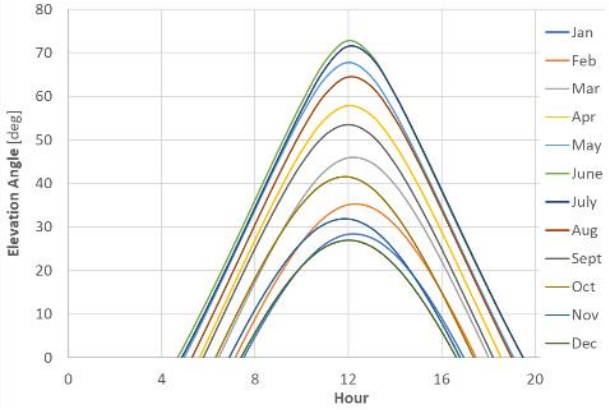

Figure 70: Solar Elevation Angle vs. Day Hour for a Typical Month-Averaged Day in Lancaster, PA

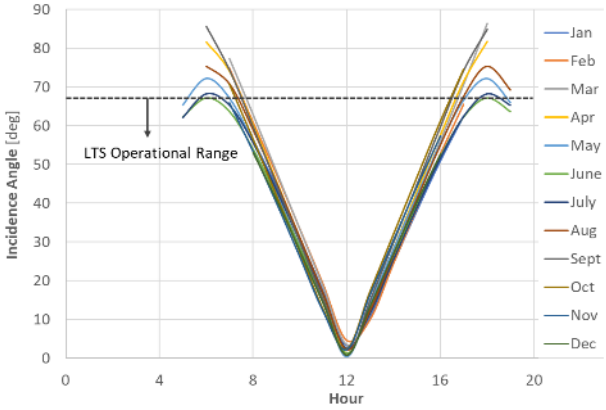

Figure 71: Incidence Angle (*i*) onto an East-West Oriented Parabolic Trough vs. Hour for a Typical Month-Averaged Day in Lancaster, PA

Two trough orientations were considered for the full-scale system; East to West (E-W) or North to South (N-S). An N-S-oriented trough tends to best track incident solar rays early and late in the day with mid-day rays striking the trough at an angle. This is a minor concern at latitudes approaching 0° or very long trough lengths. However, this can be a significant concern at higher latitudes (particularly in winter) and short trough lengths, as shown in the ray-tracing results for large incidence angles. ACT's full-scale system's short length of ~17ft and Lancaster, PA's relatively high latitude or ~40°N, suggest that an E-W trough orientation is preferred. This configuration is advantageous for maximizing peak power as there is less atmospheric attenuation of incident solar radiation at noon, and noontime also corresponds to the minimum incidence angle. Figure 71 presents the incidence angle for an E-W-oriented parabolic trough vs. hour for a typical month-average day in Lancaster, PA.

The final step was to combine the incidence angle data for an E-W-oriented trough in Lancaster (Figure 71) with the LTS modeling results predicting condenser power vs. incidence angle (Figure 68). Hourly DNI data for Lancaster was obtained from the National Renewable Energy Lab's (NREL) Standard Advisor Model (SAM) [24]. The results of combining incidence angle data, location-specific DNI, and LTS modeling results are presented in Figure 72 for an E-W-oriented trough in Lancaster.

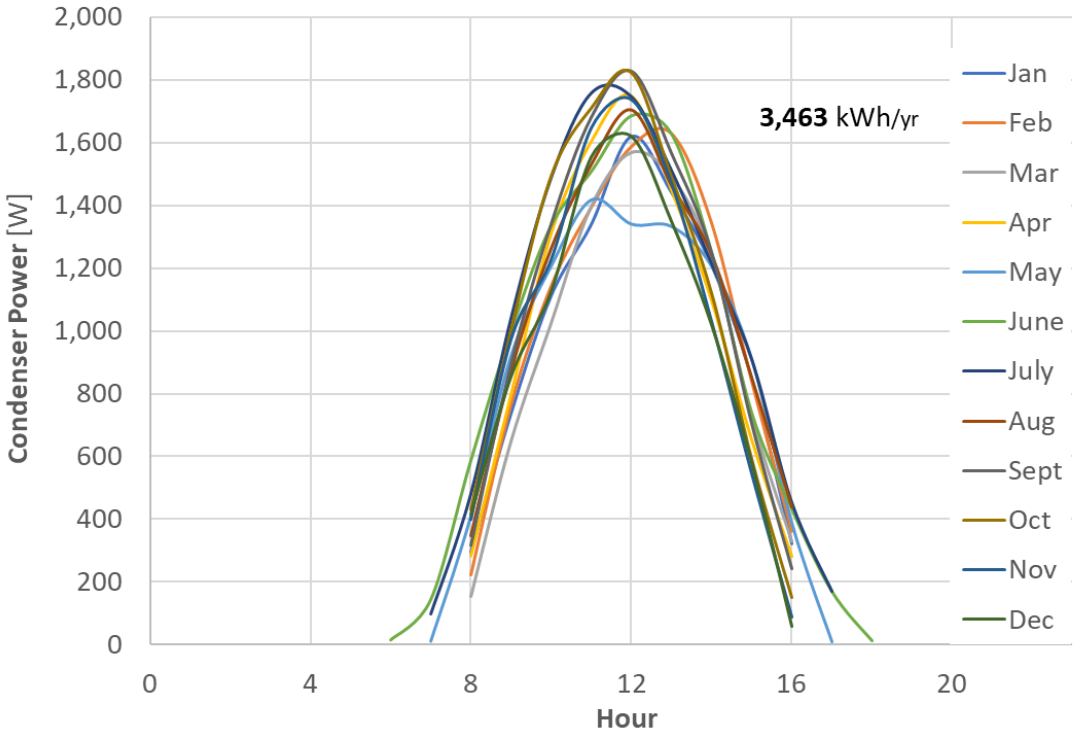

Figure 72: Predicted Condenser Power vs. Hour of an Average Month Day in Lancaster, PA for an E-W-Oriented Parabolic Trough.

As seen in Figure 72, peak condenser power on a typical day approaches 1,800 W throughout the year with total annual energy to the condenser reaching 3,463 kWh/yr. It should be noted that monthly averaging of hourly data reduces the maximum peak power considerably, with a peak condenser power of 3.7kW projected for the year. This power roughly corresponds to the system design point of 1,000 W/m^2.

Full-Scale System Fabrication

ACT fabricated a full-scale solar-heated loop thermosyphon according to the design and modeling detailed above. Figure 73 presents the full-scale parabolic trough solar collector LTS as fabricated.

Five (5) resistance temperature detectors (RTDs) record temperatures around the LTS; at the evaporator inlet, evaporator outlet, condenser inlet, condenser outlet, and at the bottom of the vertical downcomer. Three (3) absolute pressure transducers record fluid pressure at the evaporator inlet, condenser inlet, and at the bottom of the downcomer. An electromagnetic flowmeter records the working fluid flow rate. On the coolant side of the condenser, a second electromagnetic flowmeter records flow, and RTDs record coolant temperatures into and out of the flat plate condenser. These coolant flow rates and temperatures are used to calculate the thermal energy removed from the condenser. A variable speed pump in the coolant radiator is modulated by the LTS's control/DAQ PLC unit. The PLC varies coolant flow to achieve and maintain the targeted LTS saturation temperature.

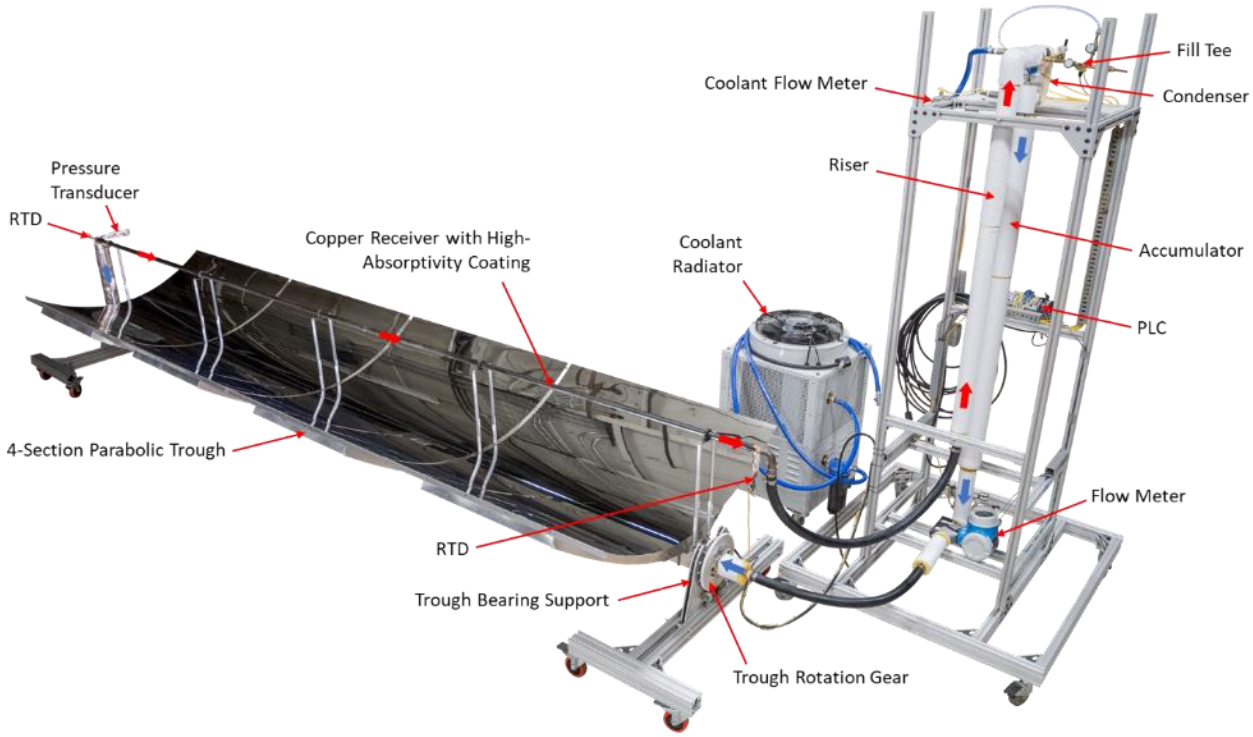

Figure 73: Full-Scale Parabolic Trough Solar Collector Loop Thermosyphon as Fabricated

The trough sections were attached to a 17ft long 4x4" aluminum box tube supported by bearing supports allowing the entire trough to rotate about the axis of the box centerline. A worm gear and 120 tooth gear attached to the box tube rotate and lock the trough position as desired. The liquid return line passes through the box tube to the inlet of the evaporator/receiver and is fully insulated with fiberglass insulation. Both the liquid return and vapor lines attach to the condenser tower by flexible, reinforced hoses. A coolant radiator removes heat from the flat plate condenser, rejecting it to the ambient air. Figure 74 presents the connections between the parabolic trough and condenser tower and Figure 75 highlights the trough angle adjustment worm gear drive and bearing supports. The full-scale parabolic trough solar was fabricated on wheels to allow the trough and condenser tower to be stowed indoors when not in use.

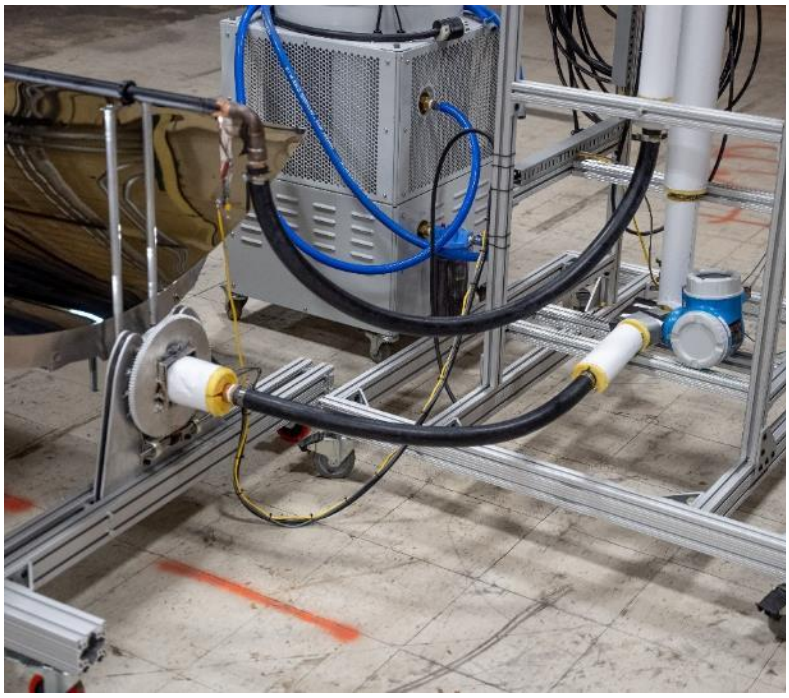

Figure 74: Detail of Connections Between Parabolic Trough and Condenser Tower

Figure 75: Detail of Trough Angle Adjustment Mechanism

On-Sun Testing of the Full-Scale LTS

The ACT team tested the full-scale LTS a handful of days during the 2nd quarter of 2022. Because of the often overcast weather in Lancaster, Pennsylvania, the team only rolled the system outside on the clearest days. The trough was setup in a small grass plot outside of the ACT facility and oriented in an E-W configuration, with the trough tipped towards South to account for altitude angle of the sun. As shown in the proceeding sections, an E-W orientation provides the most consistently high power at noon. It also allows the trough tilt to remain fixed throughout the day, which was helpful as the full-scale system featured manual trough tilt control. Figure 76 presents the full-scale system during testing.

Figure 76: Full-Scale Parabolic Trough Solar Collector LTS During Testing

Initially, the LTS system experience startup issues due to the flexible hose section after the evaporator. This hose had been oriented downward towards the pivot point of the trough to allow the system to pivot more freely. However, this design choice resulted in a liquid “trap” within the two-phase riser line. While modeling suggested this should work, the model does not take system startup into account. During startup, the “trap” is filled with liquid, which stops the flow of two-phase liquid from the receiver to condenser.

To solve this problem, the fitting at the exit of the receiver tube was rotated to prevent the hose from drooping downward at the exit of the evaporator. One this change was made, the system operated as expected during subsequent test days. Figures 77 and 78 present additional images of the full-scale parabolic solar collector LTS during testing at ACT.

Figure 77: Full-Scale Parabolic Trough Solar Collector LTS During Testing

Figure 78: Close Up of Solar Receiver During On-Sun Testing

Figure 79 presents a portion of the temperature and flow rate test data from the June 17th, 2022 full-scale system test. Temperatures are reported at the evaporator inlet, evaporator exit, condenser inlet, and at the bottom of the downcomer upstream of the electromagnetic flow meter. Both the water flow rate in the loop and the coolant flow rate to the condenser are also shown. During the test, the coolant pump controller was set to maintain a condenser inlet temperature of 120°C. As solar energy was added to the system, both the evaporator and condenser temperatures rise to the point where the pump controller turns on the coolant pump. Even when operating at the lowest possible coolant flow rate, the cooling water is very effective at removing heat from the system, and loop temperatures quickly fall. As the condenser inlet temperature falls below 120°C, the pump shuts off and the system is allowed to rise in temperature again. This process is responsible for the cyclic temperature and flow rate behavior seen in Figure 79.

The thermal efficiency of the system can be examined by comparing the outlet temperature of the evaporator to the inlet temperature of the condenser. A large temperature drop will require much higher evaporator temperatures to ensure adequate temperature in the condenser to effectively desalinate brackish water. Figure 79 indicates

that the temperature drop from evaporator to condenser is typically no greater than about 10°C.

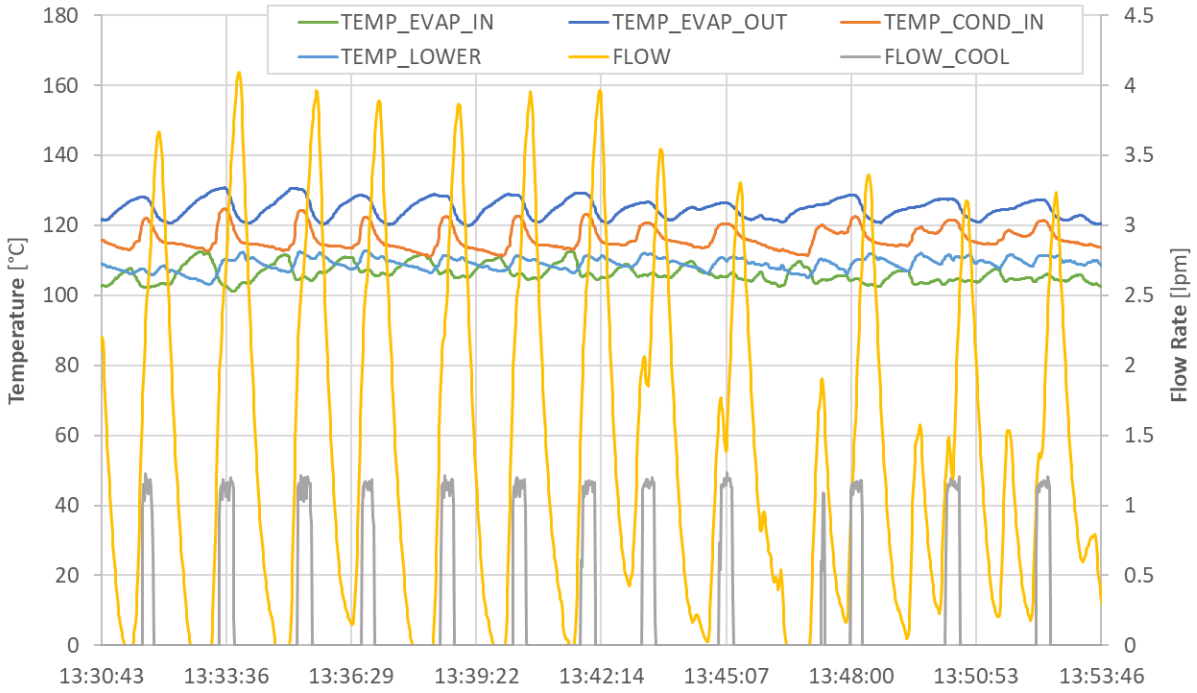

Figure 79: A Portion of the Full-Scale Parabolic Trough LTS Test Data from a June 17, 2022 Test

The temperature difference between evaporator and condenser is plotted vs. the cooling water flow rate in Figure 80. When the cooling water flow is stopped (the condenser temperature is not at the set point), the system can experience differences in temperature of up to 78°C between the evaporator exit and condenser inlet. However, when cooling water is flowing and heat is being removed from the system, the temperature difference falls to within 10°C. This is an important finding as it shows the system operates efficiently when heat is being transferred through the loop. Future systems will need to better balance the heating and cooling loads to allow heat to be continuously removed from the condenser without quenching the entire system. In other words, this full-scale system should

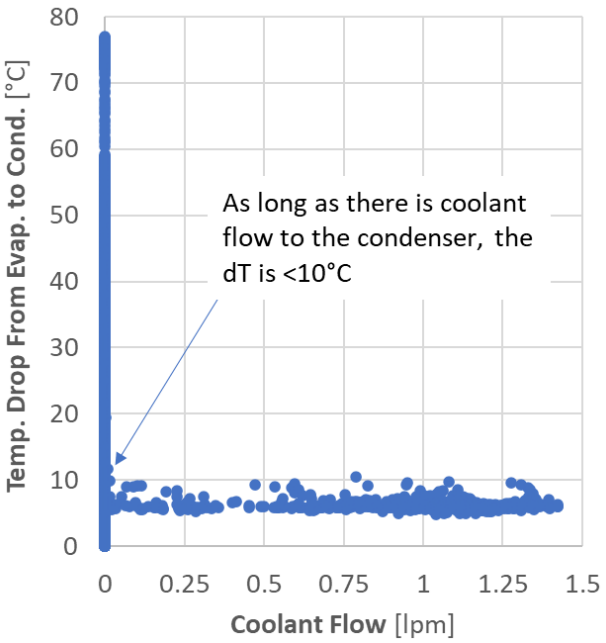

Figure 80: ΔT from Evaporator to Condenser vs. Cooling Water Flow Rate.

either utilize a cooling water pump with a lower minimum flow rate or a condenser with less surface area.

If the highly cyclical data illustrated in Figure 79 is time-averaged, the time-averaged condenser power can be found. This time averaging is important as the calculated (from calorimetry) condenser power is high when coolant is flowing but falls to 0 during periods where the cooling water pump is idle. When time-averaged across the day, an average condenser power of 500W is found, with an average peak condenser power of 3.8kW during periods when the cooling water pump is operational. This difference in average peak power (during pump operation) and overall average power is due to the cycling of the pump as outlined above.

The team would have liked to continue testing further and experimented with a reduced pump flow rate, but the period of performance was ending and the number of clear days in Lancaster, PA was limited. Despite these limitations, this test showed that a concentrated solar-driven loop thermosyphon can work and will effectively transfer heat from the hot evaporator/receiver to the cold condenser. Future work would focus on refining this system to operate more consistently.

Stakeholder Engagement & Marketing

In addition to the four technical directions of this program, the team completed stakeholder engagment and marketing as part of Tasks 1.7, 2.6, and 3.5. A summary of this work is compiled in the following sections.

Task 1.7: *Perform a preliminary market research to understand the solar thermal desalination market, the key players, and potential partners for technology integration and commercialization.*

The loop thermosyphon solar collection system provides passive, effective solar-to-thermal energy conversion. With proper design, the system can provide a high solar-to-thermal efficiency with a low cost that satisfies the requirement of the fast-growing desalination market, specifically for thermal desalination. This technology can be applied to provide moderate temperature saturated steam to state-of-the-art thermal desalination technologies such as MSF and MED, as well as emerging technologies such as the Vacuum Freezing Desalination under development in ACT.

As the commercialization strategy of this technology, ACT plans to manufacture the loop thermosyphon systems in house and sell to the industrial key players and end users to allow them to apply this technology in their existing and new desalination plants. The goal of the commercialization efforts is to advertise the technology and educate the potential customers and stakeholders of the solar desalination community to satisfy the need for low cost, sustainable thermal energy.

With the potential of market availability, the applicability of solar desalination depends on the availability of solar energy, saline water (seawater, brackish water, etc.) availability, freshwater availability, and technology readiness. The geographical requirements are well satisfied in the USA for solar desalination application, especially in the southwest

and the west coast. In the application of the loop thermosyphon technology to the field of solar desalination, a few types of stakeholders may have different aspects of influence to this technology, including business associations, thermal desalination technology developers and system integrators, and local regulators.

The business associations of water and desalination technologies are scientific and educational organizations to improve the quality of water resource and water works. Directly related associations in the US include American Water Works Association (AWWA), the International Desalination Association (IDA), and Environmental & Water Resources Institute (EWRI) by American Society of Civil Engineers (ASCE), etc. There are also other related associations such as American Society of Mechanical Engineers (ASME), American Society of Thermal and Fluid Engineers (ASTFE), Electric Power Research Institute (EPRI), etc. ACT is actively participating in communities of this industry, including but not limited to the conferences hosted by these organizations.

The technology developers and system integrators are the major group of customers who may be interested in utilizing the loop thermosyphon technology for thermal energy production for their desalination systems. Examples of these stakeholders include international companies such as Veolia Environment and Suez, and domestic companies such as Aquatech and Evoqua Water Technologies. To engage with potential customers, ACT will continue to advertise this technology and the research which has been completed on this program, both through ACT's website and by attending conferences and trade shows. Table 8 list stakeholders identified by ACT, who may be interested in further development of the technology developed during the program.

In March 2019, ACT joint the CSP Summit in Oakland, CA and presented the loop thermosyphon solar collection technology. The presentation was well received, and a few potential collaborations was discussed with researchers and stakeholders during the summit. In the next quarter, we will continue engaging with the potential collaborators by presentation, invention disclosure, publication, etc., as well as direct contact with established connections in current and previous research collaborations.

Table 8. List of Stakeholders that ACT can Potentially Collaborate with to Further Develop the Loop Thermosyphon Solar Collection Technology.

Business Associations	American Water Works Association (AWWA)
	the International Desalination Association (IDA)
	Environmental & Water Resources Institute (EWRI)
	Electric Power Research Institute (EPRI)
	American Society of Mechanical Engineers (ASME)
	American Society of Thermal and Fluid Engineers (ASTFE)
Solar Thermal System Integrators	Skyfuel Inc.
	Rioglass Solar
	Apricus
	SunEarth
	AET Solar
Thermal Desalination System Integrators	CH2M
	Veolia
	Doosan
	IDE America
	Suez Degremont
	Aquatech
	Xylem Inc.
	Evoqua Water Technology
	Island Water Association
End Users	SENER USA
	Local governments, e.g. Orange County, Marin County, etc.
	Power plants

Task 2.6: *Stakeholder Engagement and Market Identification /*

Task 3.5: *Market Strategy Development*

The LTS modeling work was presented at the SolarPACES 2020 conference [25] and the 5-6th Thermal and Fluids Engineering Conference (TFEC) held in late May of 2021 [26]. Both a peer-reviewed conference paper and presentation video [27] (remote conference) were prepared for both conferences. A poster presentation for the SolarPACES 2022 conference in Albuquerque, NM has been accepted. This poster focuses on the linear solar simulator constructed during the program. In addition to these conferences, the ACT project team has begun to work with ACT's sales and marketing team to increase market outreach and awareness for the technology development effort.

ACT will continue to perform market research and work with our internal sales and marketing team to identify and reach out to potential stakeholders, particularly potential integration partners for continued development and deployment of the LTS solar collector system. This includes suppliers or developers of the solar parabolic troughs and developers of thermal desalination or other users of process heat that may be supplied by ACT's LTS solar collector.

ACT will evaluate and pursue communication and interaction with stakeholders in the field of solar thermal desalination, including business associations, solar thermal system integrators, thermal desalination system integrators, and end-users including local regulators. ACT will continue to pursue these relationships in pursuit of commercialization of the developed technology. This will include obtaining non-disclosure agreements (NDAs) and investigating avenues for licensing and manufacturing of the loop thermosyphon solar collector.

In addition to the solar thermal desalination application, ACT is pursuing research funding opportunities for using the loop thermosyphon enhanced solar collector to provide renewable process heat for a variety of industrial applications. The developed loop thermosyphon performance model has already proved useful in other LTS design projects, and will be used in future research and design programs. Several conference and journal manuscripts are in preparation; ACT routinely uses published conference and journal articles to advertise its capabilities and research results.

Inventions, Patents, Publications, and other Results

The following publications were made during the course of this project:

J. Charles, N. Van Velson, J. Wang, & S. Hoenig, Modeling of a Loop Thermosyphon Supplying Solar Energy to a Desalination Boiler, AIP Conference Proceedings, 2022, 2245, 140003.

Charles, J., & Van Velson, N. (2021). Loop Thermosyphon Design for Solar Thermal Desalination. In ASTFE Digital Library. Begel House Inc.

References

[1] Luo, Z., Wang, C., Wei, W., Xiao, G., & Ni, M. Performance improvement of a nanofluid solar collector based on direct absorption collection (DAC) concepts. *International Journal of Heat and Mass Transfer*, 2014, 75, 262-271.

[2] Ye, N., Wang, Z., Wang, S., Fang, H., Wang, D. Aqueous aggregation and stability of graphene nanoplatelets, graphene oxide, and reduced graphene oxide in simulated natural environmental conditions: complex roles of surface and solution chemistry. *Environmental Science and Pollution Research*, 2018, 25(11), 10956-10965.

[3] D. Li, M. B. Müller, S. Gilje, R. B. Kaner, G. G. Wallace. Processable Aqueous Dispersions of Graphene Nanosheets. *Nature nanotechnology*, *3*(2), (2008), 101.

[4] W. Hwang. Enhancement of Nanofluid Stability and Critical Heat Flux in Pool Boiling with Nanocellulose. *Carbohydrate Polymers, 213*, (2019) 393-402.

[5] R. W. Lockhart and R. C. Martinelli, "Proposed Correlation of Data for Isothermal Two-Phase Two-Component Flow in Pipes," *Chemical Engineering Progress, 45*(1), 1949, pp. 39-48.

[6] D. Chisholm, "A Theoretical Basis for the Lockhart-Martinelli Correlation for Two-Phase Flow." *International Journal of Heat and Mass Transfer 10*, 1967, pp. 1767-1778.

[7] M.S. Yadav, "Interfacial Area Transport Across Vertical Elbows in Air-Water Two-Phase Flow." *PhD thesis, Pennsylvania State University*, 2013.

[8] A. Filip and R. D. Bălţăreţu, "Comparison of Two-Phase Pressure Drop Models for Condensing Flows in Horizontal Tubes." *Mathematical Modeling in Civil Engineering, 10*(4), 2014, pp. 19-27.

[9] S. G. Kandlikar, "A General Correlation for Saturated Two-Phase Flow Boiling Heat Transfer Inside Horizontal and Vertical Tubes," *Journal of Heat Transfer, 112*, 1990, pp. 219-228.

[10] J.C. Chen, "A Correlation for Boiling Heat Transfer to Saturated Fluids in Convective Flow," *Brookhaven National Laboratory*, Upton, NY, 1962.

[11] D. Papini, A. Cammi, “Modelling of Heat Transfer Phenomena for Vertical and Horizontal Configurations of In-Pool Condensers and Comparison with Experimental Findings.” *Science and Technology of Nuclear Installation,* 2010.

[12] J. R. Hartenstine, R. W. Bonner, J. R. Montgomery, T. Semenic. Loop Thermosyphon Design for Cooling of Large Area, High Heat Flux Sources. *IPACK2007-33993, Proceedings of ASME InterPACK 2007*, Vancouver, BC, Canada.

[13] Bankoff, S. G. “A Variable Density Single Fluid Model for Two Phase Flow with Particular Reference to Steam-Water Flow.” *J. Heat Transfer,* 11, pp. 165–172, (1960).

[14] Cavallini, A., Censi, G., Del Col, D., Doretti, L., Longo, G.A., Rossetto, L. “Condensation of Halogenated Refrigerants Inside Smooth Tubes.” *HVAC&R Res. 8*, pp. 429–451 (2002).

[15] Chisholm, D. “Pressure Gradients Due to the Friction During the Flow of Evaporating Two Phase Mixtures in Smooth Tubes and Channels.” *Int. J. Heat Mass Transf. 16*, pp. 347–358 (1973).

[16] Friedel, L. “Improved Friction Pressure Drop Correlation for Horizontal and Vertical Two Phase Pipe Flow.” *Eur. Two Phase Flow Group Meet.* Pap. 18, pp. 485–492 (1979).

[17] Friedel, L. “Two-Phase Frictional Pressure Drop Correlation for Vertical Downflow.” *Ger. Chem. Eng. 8*(1), pp. 32–40 (1985).

[18] Ghajar, A., Bhagwat, S. “Chapter 4: Flow Patterns, Void Fraction and Pressure Drop in Gas-Liquid Two Phase Flow at Different Pipe Orientations.” *Frontiers and Progress in Multiphase Flow 1*, Cheng, L. (ed.). Springer International Publishing, Switzerland, (2014).

[19] Wolverine Tube, Inc. “Chapter 13: Two-Phase Pressure Drops.” Accessed 12/8/2020 from <http://www.thermalfluidscentral.org/e-books/pdf/edb3/13.pdf>, (2006).

[20] Levêque, G., Bader, R., Lipiński, W., Haussener, S. High-flux Optical Systems for Solar Thermochemistry. *Solar Energy,* 2017, http://dx.doi.org/10.1016/j.solener.2017.07.046

[21] Tawfik, M., Tonnellier, X., Sansom, C. Light Source Selection for a Solar Simulator for Thermal Applications: A Review. *Renewable and Sustainable Energy Reviews, 90*, 2018, p.802-813. https://doi.org/10.1016/j.rser.2018.03.059

[22] Siegel, N., Roba, J. Design, Modeling, and Characterization of a 10kW$_e$ Metal Halide High Flux Solar Simulator. *Journal of Solar Energy Engineering, 140*, 2018, https://doi.org/10.1115/1.4039658

[23] Philips. MSR Gold 2500/2 FastFit 1CT/4. *Signify Holding.* Accessed 1/14/2020: < https://www.lighting.philips.com/main/prof/conventional-lamps-and-tubes/special-lamps/entertainment/touring-stage/msr-goldtm-fastfit/928106405115_EU/product>

[24] System Advisor Model Version 2018.11.11 (SAM 2018.11.11). National Renewable Energy Laboratory. Golden, CO. Accessed December 15, 2021. <https://sam.nrel.gov>

[25] Charles, J., Van Velson, N., Wang, J., Hoenig, S. Modeling of a Loop Thermosyphon Supplying Solar Energy to a Desalination Boiler. *AIP Conference Proceedings,* 2445, (2022), p.140003. < https://aip.scitation.org/doi/abs/10.1063/5.0086288>

[26] Charles, J., Van Velson, N. Loop Thermosyphon Design for Solar Thermal Desalination. *5-6th Thermal and Fluids Engineering Conference (TFEC),* May 2021, p.239-248.

[27] Charles, J. Loop Thermosyphon and Solar Energy. *Online Video (YouTube).* < *https://www.youtube.com/watch?v=nGKTPkc1dBo*>